Fluctuation-induced dissipation for ocean surface waves

Guoqiang Liu[1,*] and Maryam Al Alshehhi[1]

[1] *Civil, Infrastructural and Environmental Engineering, Khalifa University of Science and Technology, Abu Dhabi, United Arab Emirates*

Phase averaging is a one-time operation. Irreversible transport is not. Here we identify a coupling hidden in the Navier-Stokes equations for surface waves propagating through turbulence whose one-time phase average vanishes but whose two-time autocorrelation yields a finite Green-Kubo friction coefficient. Classical phase averaging removes this stochastic vortex force, the bilinear coupling between wave orbital motion and turbulent vorticity fluctuations, because its instantaneous mean is zero. Using a statistical-mechanical treatment, we show that its finite-time autocorrelation yields a non-negative attenuation rate and, under inertial-range conditions, a closed-form law for remote swell decay determined by the turbulent dissipation rate, wave frequency, and gravity, without fitting parameters to wave-attenuation observations. Remote ocean swell provides a natural test bed because competing processes are weak. The theory predicts two observational signatures absent from deterministic descriptions: a positive bias in standard satellite attenuation estimates caused by multiplicative-noise logarithmic drift, and a finite probability that individual tracks show apparent energy gain. Both are supported by 241 trans-oceanic satellite observations. The missing mechanism was not absent from the governing equations, but removed by phase averaging. The analysis identifies a persistent non-breaking pathway by which surface-wave energy enters the upper ocean.

In Brownian motion a zero-mean random force, negligible in any single collision, produces a measurable friction coefficient once its autocorrelation is integrated through the Green-Kubo relation[1–3]. Here we show that a similar statistical-mechanical route resolves a sixty-year-old problem in wave physics.

Ocean swell decays measurably across entire ocean basins[4, 5], yet wave breaking, the dominant irreversible sink[6, 7], is effectively absent. This non-breaking pathway matters beyond swell forecasting. Wind transfers roughly 60 TW to the ocean surface through waves[8, 9], and where that energy ultimately goes shapes upper-ocean mixing, air-sea momentum exchange and climate-relevant heat redistribution[10, 11].

Classical candidates do not close the gap. Molecular viscosity underpredicts the required attenuation by four orders of magnitude. Eddy-viscosity closures overpredict it by two to three[7, 12]. The laminar air-side boundary layer[13] remains an order of magnitude too weak[14]. The missing mechanism reflects a structural blind spot in how wave-current coupling has been coarse-grained.

Classical wave-current theory is built on phase averaging[15, 16]. Phase averaging captures the cycle-mean coupling but removes every fluctuating contribution whose phase average vanishes. This is analogous to retaining only the mean force on a Brownian particle and discarding the thermal noise. The resulting dynamics contains no mechanism for fluctuation-induced friction, so operational wave models supply swell attenuation as an empirical source term rather than deriving it[12, 17–19]. The resolution requires moving from one-time averages to the two-time correlations that determine irreversible energy transport. More generally, this raises the question whether zero-mean couplings removed by phase averaging can still leave measurable transport through their two-time correlations.

Here we identify that missing term in the Navier-Stokes equations. When wave orbital motion sweeps through turbulent vorticity fluctuations, it generates a stochastic vortex force whose phase average vanishes but whose two-time autocorrelation can remain finite. The point is not to introduce another empirical term, but to restore a fluctuation already present in the exact equations and show that its autocorrelation yields a non-negative Green-Kubo attenuation rate.

Remote ocean swell isolates this coupling for direct test. After leaving the generating storm, breaking, wind input and nonlinear wave-wave transfer are all strongly reduced, so weak non-breaking losses accumulate coherently over planetary scales and become measurable by satellite altimetry[5, 20]. The observations contain a more discriminating clue than the mean decay rate alone. Across independent datasets, one in eight to one in four tracks yield apparent negative attenuation[5, 14, 20], that is, inferred swell growth along the track. A deterministic decay law cannot produce such a tail. A stochastic transport process predicts it as a natural consequence of finite-sample fluctuations, just as Brownian displacement includes excursions against the mean drift.

Starting from the Navier-Stokes equations, we introduce a three-layer decomposition of the rotational vorticity that isolates a stochastic vortex force discarded by classical phase averaging. Its two-time autocorrelation produces a non-negative Green-Kubo transport coefficient whose one-time mean vanishes, so one-time phase averaging is not a sufficient criterion for transport irrelevance. Under Kolmogorov inertial-range closure the resulting kernel yields a parameter-free swell attenuation law. The same framework predicts an Itô bias and a finite probability of apparent energy gain in single-track estimates. We test both against 241 trans-oceanic satellite events, including a 26% sub-population of apparent energy-gain tracks that the theory predicts quantitatively from the same force autocorrelation that

governs the mean.

The force that phase averaging removes

Within the present non-breaking, potential-wave framework, phase-averaging discards the non-viscous term whose autocorrelation can produce irreversible swell dissipation. The total velocity field admits the Helmholtz decomposition[21] $\boldsymbol{U} = \boldsymbol{u}_\phi + \boldsymbol{u}$, where $\boldsymbol{u}_\phi = \nabla\phi$ is the irrotational wave orbital velocity and $\boldsymbol{u}$ contains all rotational motions. Substituting into the Navier-Stokes momentum equation and collecting terms, the wave-current coupling reduces to a single non-viscous channel, the orbital vortex force $\boldsymbol{f}_\mathrm{v} = \boldsymbol{u}_\phi \times \boldsymbol{\omega}$, where $\boldsymbol{\omega} = \nabla \times \boldsymbol{u}$ (Supplementary S1 A-B).

The vorticity $\boldsymbol{\omega}$ contains contributions on very different timescales. We introduce a three-layer decomposition of the rotational vorticity into the ensemble-mean $\bar{\boldsymbol{\Omega}}$, the wave-slaved oscillation $\boldsymbol{\omega}_\mathrm{wave}$, and the autonomous turbulent fluctuation $\boldsymbol{\omega}'$ (Supplementary S1 D-E). The first two layers enter the classical Craik-Leibovich framework[15, 16]; the third is required to isolate the stochastic vortex force identified below. The vortex force inherits the split:

$$\boldsymbol{f}_\mathrm{v} = \underbrace{\boldsymbol{u}_\phi \times \bar{\boldsymbol{\Omega}} + \boldsymbol{u}_\phi \times \boldsymbol{\omega}_\mathrm{wave}}_{\text{Phase-averaged sector}} + \underbrace{\boldsymbol{u}_\phi \times \boldsymbol{\omega}'}_{\text{stochastic vortex force}} . \tag{1}$$

Phase averaging yields, at leading order, $\langle \boldsymbol{u}_\phi \times \bar{\boldsymbol{\Omega}} \rangle_\varphi = \boldsymbol{0}$ and $\langle \boldsymbol{u}_\phi \times \boldsymbol{\omega}' \rangle_\varphi = \boldsymbol{0}$. The wave-slaved term rectifies, via the phase-averaging identity[22], into the Craik-Leibovich vortex force $\boldsymbol{u}_\mathrm{s} \times \boldsymbol{\Omega}_\mathrm{s}$ (where $\boldsymbol{\Omega}_\mathrm{s} = \bar{\boldsymbol{\Omega}} + \boldsymbol{\omega}'$ is the full phase-averaged but not ensemble-averaged vorticity), driving Langmuir circulations[15, 16, 23]. But irreversibility is controlled not by a one-time phase average but by the two-time autocorrelation entering the Green-Kubo formula. At that level the discarded term $\boldsymbol{u}_\phi \times \boldsymbol{\omega}'$ survives, whereas the rectified CL force remains a zero-frequency quantity and cannot damp the resolved swell mode.

We call $\boldsymbol{f}_\mathrm{svf} = \boldsymbol{u}_\phi \times \boldsymbol{\omega}'$ the *stochastic vortex force* (SVF). Fig. 1a-c illustrates a single wave-eddy encounter. The CL contribution carries no spectral weight at the wave frequency and cannot enter the mode-level friction coefficient. The SVF instead produces irreversible transfer, depositing a small random energy increment into the rotational flow whose sign and magnitude are unpredictable for any single encounter. Fig. 1d schematically shows the SVF autocorrelation. Although it need not be positive at all lags, its time integral, the Green-Kubo coefficient, is non-negative (see below). Over the $N \sim 10^5$ near-independent encounters along a trans-oceanic path, the cumulative energy change is a biased random walk (Fig. 1e, Supplementary Video 1).

Irreversibility from fluctuations

At the wave-subspace level, the relevant object is not the field $\boldsymbol{f}_\mathrm{svf}(\boldsymbol{x}, t)$ itself but its mode projection $F_k(t) = \int \boldsymbol{\psi}_k^* \cdot \boldsymbol{f}\, \mathrm{d}^3x$ (Methods, equation (8)). Under Assumptions A2-A5, the only bath-driven contribution is the projected SVF, whose autocorrelation enters the Green-Kubo formula.

Applying Mori-Zwanzig[3, 24, 25] to the resolved amplitude $a_k(t)$ yields a generalised Langevin equation with this projected SVF as the fluctuating force. The second fluctuation-dissipation relation (FDR-II)[3, 24, 26] connects the memory kernel to the force autocorrelation (Methods, equation (9), Supplementary S2 B). For remote swell the wave and local turbulence originate from independent sources separated by thousands of kilometres, so their cross-correlation vanishes to leading order (Assumption A3, Supplementary S2 B-C). When $\tau_\mathrm{c} \ll \Gamma^{-1}$ the memory integral reduces to the Green-Kubo formula[1, 2] for the damping rate,

$$\Gamma(k) = \int_0^\infty \mathrm{Re}\big\langle F_k(0)\, F_k^*(t) \big\rangle \, \mathrm{d}t \,\Big/\, 2E_k \;\geq\; 0. \tag{2}$$

The force autocorrelation factorises as $\langle F_k(0)\, F_k^*(t)\rangle = 2E_k\, \mathcal{G}_k(t)$, so Γ is independent of wave amplitude, a material property of the mixed-layer turbulence rather than of the swell passing through it. This places remote swell in a noise-dominated Mori-Zwanzig regime[27], in which the noise kernel becomes analytically tractable because the underlying force has an explicit microscopic form. The inequality in equation (2) is guaranteed by Bochner's theorem[28], so the ensemble-mean energy decays monotonically.

Irreversibility arises because the turbulent bath is not frozen. A real eddy possesses internal degrees of freedom through the turbulent cascade; energy absorbed from the wave is redistributed among those modes before the wave phase returns. The weak evolution during each encounter breaks time-reversal symmetry, producing a net loss of order $\delta^2 E_k$ while the fluctuation remains of order δE_k (Supplementary S2 I). The single control parameter $\delta \equiv u'/c_\mathrm{g} \sim 10^{-3}$-$10^{-2}$ governs both the bias and the noise (Methods, Supplementary S6).

A closed-form law from turbulence physics

The sign of Γ is theorem-level (equation (2)). The frequency law is not. To obtain a closed-form $\mu_E(\omega)$, two additional ingredients are needed. The first is scale locality of the coupling kernel. The second is a turbulence spectral closure at the selected scales.

Expressing the force autocorrelation in wavenumber space converts the Green-Kubo integral into a weighted sum over the turbulent energy spectrum (Supplementary S3 A-C):

$$\Gamma(k) \;\propto\; \int_0^\infty E_\mathrm{u}(q)\, q\, \mathcal{W}\Big(\frac{q}{k}\Big)\, \mathrm{d}q, \tag{3}$$

where q is the eddy wavenumber and $\mathcal{W}(q/k)$ a dimensionless kernel encoding how a swell mode at k cou-

ples to an eddy at q. Wave-eddy geometry constrains $\mathcal{W} \propto (q/k)^2$ for $q/k \ll 1$ (Galilean invariance and action conservation) and suppresses it at least as $(q/k)^{-1}$ for $q/k \gg 1$ (finite orbital penetration) (Supplementary S3 D, S5 B). Scale locality is not assumed but computed. Large eddies produce nearly uniform vorticity across the orbital excursion, reducing the interaction to reversible refraction[29]; small eddies are confined shallower than the orbital layer[30]; Kolmogorov weighting concentrates energy at intermediate scales. Eddies with $0.5k \lesssim q \lesssim 2k$ account for 60-70% of the total attenuation (Fig. 2).

At these scales, deep-water swell propagates far faster than mixed-layer turbulent velocities ($c_g/u' \sim 10^2$), so the force decorrelates by advective sweeping ($\tau_{\rm eff} \sim (qc_g)^{-1}$) rather than eddy turnover (Extended Data Fig. 2, Fig. 1d). This extreme separation places the system in the Markovian limit of Mori-Zwanzig, where the wave acts as a fast probe of a slowly evolving turbulent bath. Substituting the Kolmogorov spectrum $E_{\rm u}(q) = C_K \varepsilon_{\rm eff}^{2/3} q^{-5/3}$ and the sweep decorrelation yields, after angular reduction and conversion to a spatial decay rate,

$$\mu_E(\omega) \;=\; C_{\rm tot}\, \varepsilon_{\rm eff}^{2/3}\, g^{-7/3}\, \omega^{8/3}, \qquad (4)$$

where $\varepsilon_{\rm eff}$ is an effective dissipation rate weighted by the orbital energy profile (Methods) and $C_{\rm tot} = 2\pi/3 \approx 2.09$ collects five independently constrained factors, none fitted to wave data ($C_{\rm tot} \in [1.10, 3.34]$, Supplementary S5). The exponent is robust once the kernel is local in scale. The Kolmogorov spectrum contributes $q^{-5/3}$, the vorticity vertex q^{+2}, and sweep decorrelation q^{-1}. Uncertainty in the physics affects only the prefactor.

The non-negativity $\Gamma \geq 0$ holds for any stationary bath, but the factorised prefactor and $\omega^{8/3}$ scaling require the turbulence spectral closure and remote-swell decoupling conditions (Supplementary S9). The Kolmogorov closure is needed only at $q \sim k \approx 0.01$-$0.03\,{\rm rad\,m^{-1}}$, where the local Ozmidov scale exceeds the orbital penetration depth and the flow is locally isotropic[31, 32] (Supplementary S5 G). Near-surface breaking eddies are spectrally filtered and do not bias the estimate (Extended Data Fig. 3). Homogeneous-turbulence simulations confirm the Kolmogorov closure is accurate to 4% within the kernel window (Supplementary S5, Extended Data Fig. 4).

What satellites actually measure

The scaling law (4) governs the ensemble-mean energy decay rate μ_E at each point along a swell trajectory. Satellite altimeters measure something different. The finite-length log-energy slope $\hat{\mu}_i \equiv -L_i^{-1} \ln[E(L_i)/E(0)]$ along a track of length L_i (Supplementary S6 A). Along a multi-thousand-kilometre track the amplitude encounters $N \sim 10^4$-10^5 near-independent turbulent eddies with correlation time τ_c far shorter than the propagation time L_i/c_g. This scale separation makes the many-encounter diffusive limit the relevant observational coarse-graining, and the amplitude obeys an effective stochastic differential equation. Because the SVF enters the energy equation multiplicatively ($\mathrm{d}E_{\rm w} \propto E_{\rm w}\,\mathrm{d}W$, Methods, equations (20)-(21)), passing from energy to log-energy generates an Itô drift. The log-slope estimator $\hat{\mu}$ tracks the geometric mean of the energy ratio, not the arithmetic mean. In the near-independent-encounter limit and at leading order in δ, this fixes three structural relations (Methods, Supplementary S6 A-B): $\langle\hat{\mu}\rangle = 2\mu_E$, $\mathrm{Var}(\hat{\mu}) = 2\mu_E/L$, $c_0 = \mathrm{Var}(\hat{\mu})\,L/\langle\hat{\mu}\rangle = 1$. Half of the observable log-slope comes from the physical damping Γ and half from the noise-induced geometric drift. The same force autocorrelation that fixes the mean also fixes the baseline single-track variance.

When the turbulent environment varies along a propagation path, the predicted observable mean for track i becomes the path-averaged rate

$$\mu_{{\rm model},i} \;=\; \frac{1}{L_i}\int_0^{L_i} \Big[2\,\mu_E\big(\omega_i;\, \varepsilon_{\rm eff}(s)\big) + \mu_v^{\rm Dore}(\omega_i)\Big]\,\mathrm{d}s. \qquad (5)$$

Under the central-limit approximation ($N \sim 10^5$ near-independent encounters per track), the finite-length estimator is

$$\hat{\mu}_i \;\sim\; \mathcal{N}\!\left(\mu_{{\rm model},i},\; c_0\,\frac{\mu_{{\rm svf},i}}{L_i} \;+\; \sigma^2_{\rm meas}\right), \qquad (6)$$

where $\mu_{\rm svf} = 2\mu_E$ is the SVF observable contribution (including the Itô factor), $\mu_{\rm model} = \mu_{\rm svf} + \mu_v^{\rm Dore}$, and only the SVF component enters the intrinsic variance because the Dore channel is deterministic. Weak along-ray correlations renormalise the second moment but not the first, replacing c_0 by $\mathcal{R}$ (Methods, Supplementary S6 D). The signal-to-noise ratio $\mathcal{S} = \mu_{\rm model}/\sigma_{\rm tot} \sim \mathcal{O}(1)$ for typical trans-oceanic paths (Extended Data Fig. 5), so the framework predicts a substantial fraction of negative single-track estimates: $P(\hat{\mu}_i < 0) = \Phi(-\mathcal{S}_i)$. Writing $\beta = C_{\rm tot}/(2\pi/3)$, the first-moment prediction is $\beta = 1$. This prediction is parameter-free because every factor in the scaling law is fixed by independent physical constraints. The pathwise variance has a leading-order structural baseline $c_0 = 1$. Along-ray correlations and environmental-input limitations renormalise c_0 in practice, making the second-moment prediction a closure test rather than a strict zero-parameter claim.

Ensemble-mean predictions

Given wind forcing and mixed-layer structure from reanalysis, the scaling law (4) predicts the ensemble-mean energy attenuation rate μ_E at every ocean point, before examining a single wave observation. The prediction depends on turbulence sustained predominantly by the local wind along the propagation path, not on the swell itself. Fig. 3a maps this prediction for 14 s swell. Because $\mathcal{S} \sim \mathcal{O}(1)$ (equation (6)), no single satellite track measures μ_E directly. The median e-folding length exceeds 10,000 km (Fig. 3d). Long-period swell

routinely crosses an entire ocean basin before decaying by a factor e. The theory thus connects a ∼100 m wave-eddy interaction scale to a ∼10,000 km propagation scale, predicting an attenuation rate of order $10^{-7}\,\mathrm{m}^{-1}$ from first principles.

We compare these predictions with 241 trans-oceanic swell events tracked by satellite altimetry[5, 33] (Methods). For each track, $\varepsilon_{\mathrm{eff}}$ is evaluated along the great-circle ray using concurrent wind and mixed-layer data[34–36]. The prefactor C_{tot} was fixed from turbulence physics before any altimeter case was examined. The global maps (Fig. 4a,b) show the same spatial organisation, with elevated attenuation near storm centres and low-attenuation corridors through subtropical gyres. The observed and predicted distributions both peak near $10^{-7}\,\mathrm{m}^{-1}$, and a paired Wilcoxon signed-rank test on the log ratios detects no systematic offset ($p = 0.816$). The stronger discriminating tests are the dependence of the negative-estimate fraction on path length and frequency (below) and the amplitude independence of Γ.

The predicted magnitude falls within the empirical corridor of existing swell-dissipation coefficients[19, 20, 37], but the functional forms differ. The empirical source term predicts $\mu \propto H_s^2$, whereas the Green-Kubo coefficient Γ is independent of wave energy (equation (2)). Satellite data strongly favour amplitude independence ($r = 0.00$, $p = 0.98$ across 241 tracks, Extended Data Fig. 1, Supplementary S8). This suggests that the empirical coefficient captures the correct turbulence-set magnitude through a different partitioning of the dependence on wave amplitude and environmental forcing.

Why some tracks show apparent energy gain

The theory predicts that roughly one in four trans-oceanic swell tracks should show apparent *energy gain*. The ensemble mean always decays, but a single satellite pass samples only $N \sim 10^4$-10^5 near-independent wave-eddy encounters, too few for the stochastic drift to dominate fluctuations. At $c_0 = 1$, $P(\hat{\mu} < 0) = \Phi(-\mathcal{S})$ yields 13-27% depending on wave period and path length (Supplementary S6 G). The observed fraction across 241 tracks is 26%.

The sharpest test is whether the theory predicts the correct fraction of negative estimates for each track individually. The intrinsic variance $c_0\,\mu_{\mathrm{svf},i}/L_i$ is not a free parameter. The fluctuation-dissipation relation locks it to the same Green-Kubo kernel that fixes the mean drift (equation (6)), so $P(\hat{\mu}_i < 0) = \Phi(-\mathcal{S}_{\mathrm{tot},i})$ depends only on quantities already determined by the first prediction line.

Fig. 5b bins the observed negative fraction by path length against the per-bin predictions; as $\mathcal{S}$ grows, the negative fraction falls. Fig. 5c repeats the test by wave frequency. Because $\mu \propto \omega^{8/3}$, higher frequencies have larger $\mathcal{S}$ and smaller negative fractions, an unambiguous signature of the $\omega^{8/3}$ law tested through the distribution rather than the mean.

Fig. 5d shows the profile log-likelihood for $\beta = C_{\mathrm{tot}}/(2\pi/3)$, profiled over c_0. The zero-parameter prediction $\beta = 1$ falls within both the statistical 95% CI and the theoretical C_{tot} range [1.10, 3.34] (Supplementary S5). Including the laminar viscous contribution (∼12-17% of the total, Fig. 5f) shifts β_{MLE} closer to unity. Jointly profiling over c_0 and σ_{meas} keeps $\beta = 1$ within the C_{tot} range (Extended Data Fig. 6b). A fixed-design Monte Carlo at $(\beta, c_0) = (1, 1)$ recovers both parameters without bias and achieves nominal coverage (Extended Data Fig. 7).

The intrinsic-variance coefficient c_0 and the non-intrinsic σ^2_{meas} are partially degenerate, trading off along a likelihood ridge (Extended Data Fig. 6a). At the adopted observational lower bound $\sigma_{\mathrm{meas}} = 0.63 \times 10^{-7}$ m^{-1}, $c_{0,\mathrm{MLE}} \approx 0.78$. The reported $c_{0,\mathrm{MLE}}$ absorbs residual prediction error in $\varepsilon_{\mathrm{eff}}$, so the true intrinsic c_0 may be lower. Langmuir circulations[23] provide one physical mechanism for $c_0 < 1$, imposing alternating-sign vorticity along the propagation path and generating negative serial correlations between successive encounters[38]. Isotropic turbulence cannot produce such anticorrelation, consistent with the DNS finding $c_0 \approx 1.1$-1.8 at $\delta = 0.01$-0.1.

The attenuation budget (Fig. 5f) comprises the dominant SVF contribution $2\mu_E$ and the laminar air-viscous rate[13] μ_v, whose fraction declines from ∼21% at $T \approx$ 12-13 s to ∼13% at $T \approx$ 16-18 s, reflecting the steeper $\omega^{7/2}$ viscous scaling relative to the $\omega^{8/3}$ SVF law.

A single theory governed by $\delta = u'/c_{\mathrm{g}}$ passes five independent tests across the 241-track dataset: ensemble-mean magnitude, global spatial pattern, negative fraction versus path length, negative fraction versus frequency, and predictive coverage. The negative attenuation estimates that previous studies discarded are not mere retrieval artefacts but a discriminating prediction of the stochastic theory. They are analogous to the backward displacements in Brownian motion that supported molecular-collision physics long before individual molecules could be observed.

DISCUSSION

The analysis rests on three linked advances. First, a three-layer decomposition of the rotational vorticity, into mean, wave-slaved, and autonomous turbulent components, isolates a stochastic vortex force $\boldsymbol{f}_{\mathrm{svf}} = \boldsymbol{u}_\phi \times \boldsymbol{\omega}'$. This term is present in the exact vortex force but vanishes under phase averaging. Second, the two-time autocorrelation of this discarded coupling produces a non-negative Green-Kubo friction coefficient, so the classical one-time criterion for transport relevance is incomplete. Third, under Kolmogorov inertial-range closure the resulting kernel yields a parameter-free swell attenuation law. The same autocorrelation that fixes the mean also fixes an Itô bias in the standard satellite estimator and a calculable fraction of tracks with apparent energy gain. Restoring the discarded term converts an empirical source term into a calculable one. It also turns what was previously treated as retrieval

noise, namely the apparent energy gain in individual tracks, into a discriminating observational signature of the theory.

What makes this realisation unusual is that three conditions converge. The fluctuating force can be explicitly identified in the governing equations. The extreme speed mismatch between wave and turbulence reduces the interaction to a tractable Green-Kubo form. And remote swell provides a natural setting in which competing processes are suppressed enough for the mechanism to be isolated observationally. A companion moving-probe experiment[38] reveals a finite, channel-specific Green-Kubo kernel for the mode-projected SVF in Navier-Stokes turbulence before any closure is imposed. Phase-averaging and time-shuffling controls confirm that the signal is carried by the discarded SVF coupling rather than by generic turbulence memory. The present work converts that channel into a parameter-free macroscopic law, while the companion provides complementary microscopic evidence that such a kernel exists in Navier-Stokes turbulence.

This reframing identifies a distinct non-breaking pathway by which surface-wave energy enters upper-ocean turbulence below the breaking layer. The coupling is weighted by the orbital structure, depositing energy at depths of order $O(1/k) \sim$ 30-80 m. A physically based representation of this pathway is currently absent from most ocean-mixing formulations[10, 11]. The scaling law offers a first-principles constraint for non-breaking wave-induced vertical mixing parameterisations[11, 39] and a grounded alternative to empirical swell-dissipation source terms in operational wave models[12, 19].

The Itô correction changes how the observational record should be interpreted. The relation $\langle\hat{\mu}\rangle = 2\mu_E$ does not imply that half the attenuation is spurious. It means that trackwise log-slope estimates combine physical damping with a noise-induced logarithmic drift. Revisiting the global swell-decay budget with this correction may alter current estimates of the non-breaking contribution to upper-ocean energy input.

In wind seas, the same coupling should exist but is masked by breaking and wind input. Quantifying its contribution there through wave-resolving simulation or targeted field experiments is a natural next step. Remote swell is also a geophysical analogue of passive microrheology[40, 41], a weak probe whose stochastic response reveals transport properties of the bath.

The deeper lesson is methodological. Phase averaging is a one-time coarse-graining, whereas irreversible transport is controlled by two-time correlations. The elimination of a zero-mean bilinear coupling by phase averaging is not unique to ocean-surface wave turbulence. Whenever such a coupling is discarded at the one-time level, its two-time autocorrelation may still produce a finite Green-Kubo transport coefficient. Remote swell is an unusually clean geophysical example because competing processes are weak enough for this channel to be isolated and tested. The same logic applies, in principle, wherever effective wave dynamics is derived by phase averaging over a slow stochastic bath. Candidate frameworks include the generalised Lagrangian-mean and Craik-Leibovich formalisms[42], and the phase-averaged parameterisations of internal and atmospheric gravity waves interacting with vortical or turbulent backgrounds.

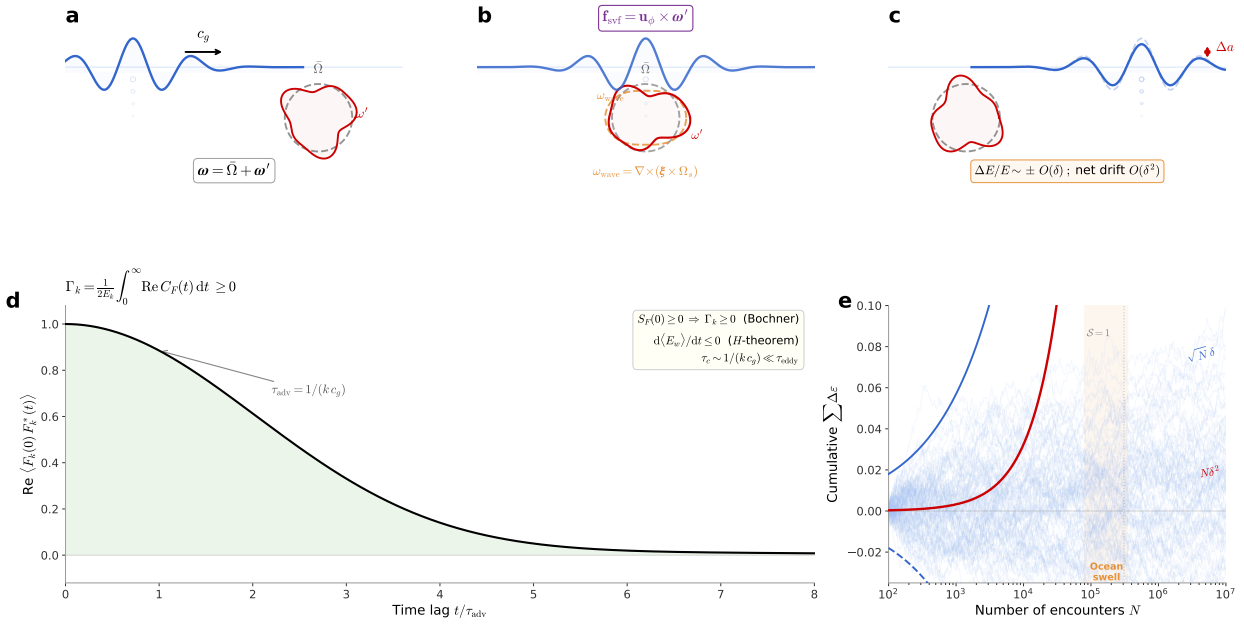

FIG. 1. **The stochastic vortex force and the Green-Kubo route to irreversible swell dissipation.** **a**, A swell packet propagates at group speed c_g toward a turbulent eddy. Before the encounter the vorticity has two components, the ensemble-mean $\bar{\boldsymbol{\Omega}}$ (grey dashed) and the autonomous turbulent fluctuation $\boldsymbol{\omega}'$ (red). The wave-slaved component $\boldsymbol{\omega}_{\rm wave}$ does not yet exist because it is created by the wave orbital motion. **b**, During the encounter. The wave-vorticity coupling generates a three-layer decomposition. $\bar{\boldsymbol{\Omega}}$ (grey dashed), $\boldsymbol{\omega}_{\rm wave} = \nabla \times (\boldsymbol{\xi} \times \boldsymbol{\Omega}_s)$ (orange dashed, wave-slaved, no autonomous degrees of freedom), and $\boldsymbol{\omega}'$ (red, autonomous). The mean-vorticity layer has zero phase average. The wave-slaved layer rectifies into the Craik-Leibovich vortex force, a zero-frequency quantity that does not project onto the wave mode at ω and therefore cannot enter its Green-Kubo friction coefficient. The third layer defines the stochastic vortex force $\boldsymbol{f}_{\rm svf} = \boldsymbol{u}_\phi \times \boldsymbol{\omega}'$ (purple arrows). Its phase average vanishes, yet its nonzero autocorrelation is the only retained source of irreversible swell decay within the non-breaking, bulk-turbulence framework. **c**, After the encounter. The packet departs with a random energy increment $\Delta E/E \sim \pm O(\delta)$ whose sign depends on the instantaneous realisation of $\boldsymbol{\omega}'$. The dashed envelope marks the original amplitude. Irreversibility enters at $O(\delta^2)$ because the autonomous evolution of $\boldsymbol{\omega}'$ breaks the symmetry, and spatial separation at c_g permanently locks the energy transfer. **d**, Normalised SVF force autocorrelation $\mathrm{Re}\,\langle F_k(0)\, F_k^*(t)\rangle$, computed from the spectral overlap integral (Supplementary S3). After projection onto the resolved mode, the carrier-wave phase cancels in the conjugate product $F_k F_k^*$, so the residual decorrelation is controlled primarily by advective sweeping at c_g, with $\tau_{\rm adv} \sim 1/(k\, c_g) \ll \tau_{\rm eddy}$. The time integral is non-negative by Bochner's theorem. **e**, Cumulative log-energy change versus encounter number N for 100 Monte Carlo realisations (light blue). Mean drift (red) grows as $N\delta^2$ and fluctuations (blue envelope) grow as $\sqrt{N}\,\delta$. Signal-to-noise reaches unity at $N \sim 1/\delta^2$ (orange band), corresponding to a trans-oceanic path of ∼15,000 km, so a finite fraction of tracks end with apparent energy gain.

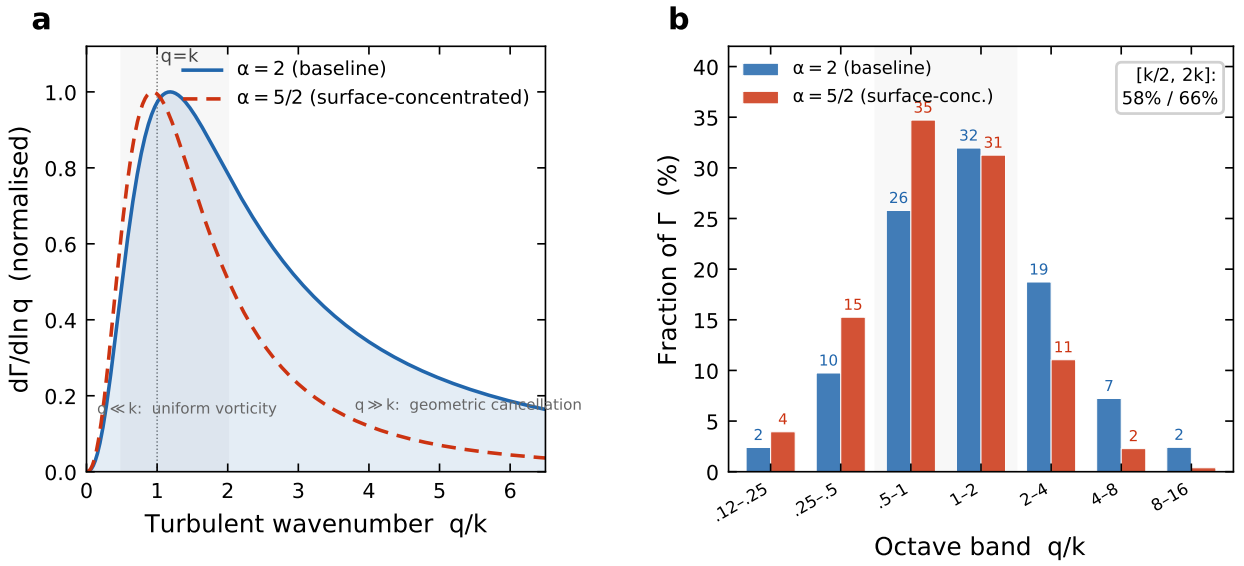

FIG. 2. **Scale-selective coupling.** **a**, Spectral contribution density $\mathrm{d}\Gamma/\mathrm{d}\ln q$ as a function of normalised turbulent wavenumber q/k, for two members of the parametric window family $\widehat{W}_\alpha(x) = x^2/(1+x^2)^\alpha$ (Supplementary S5 B). The baseline model $\alpha = 2$ (blue solid, surface-injected turbulence with depth confinement $\chi_q \propto e^{-qz}$) and the surface-concentrated model $\alpha = 5/2$ (orange dashed, enhanced near-surface enstrophy). Three independent mechanisms suppress coupling away from $q \simeq k$. Large eddies ($q \ll k$) produce nearly uniform vorticity across the orbital excursion. Small eddies ($q \gg k$) cancel by geometric averaging within one orbital penetration depth. The Kolmogorov energy weighting concentrates the inertial-range spectrum at intermediate scales. All three select $q \simeq k$, confirming that the SVF coupling is local in scale. The shaded band marks the interval $[k/2, 2k]$. **b**, Fractional contribution to the total damping rate Γ from successive octave bands of q/k. For the baseline window ($\alpha = 2$), eddies with $k/2 \leq q \leq 2k$ account for 58% of the total. For the surface-concentrated window ($\alpha = 5/2$), the same band captures 66%. This scale locality is what allows the Kolmogorov $-5/3$ spectrum, evaluated at the single scale $q \simeq k$, to fix the $\omega^{8/3}$ exponent without free-parameter fitting. Uncertainty in the enstrophy depth profile affects only the prefactor C_{tot} (Supplementary S5, Supplementary Table S1).

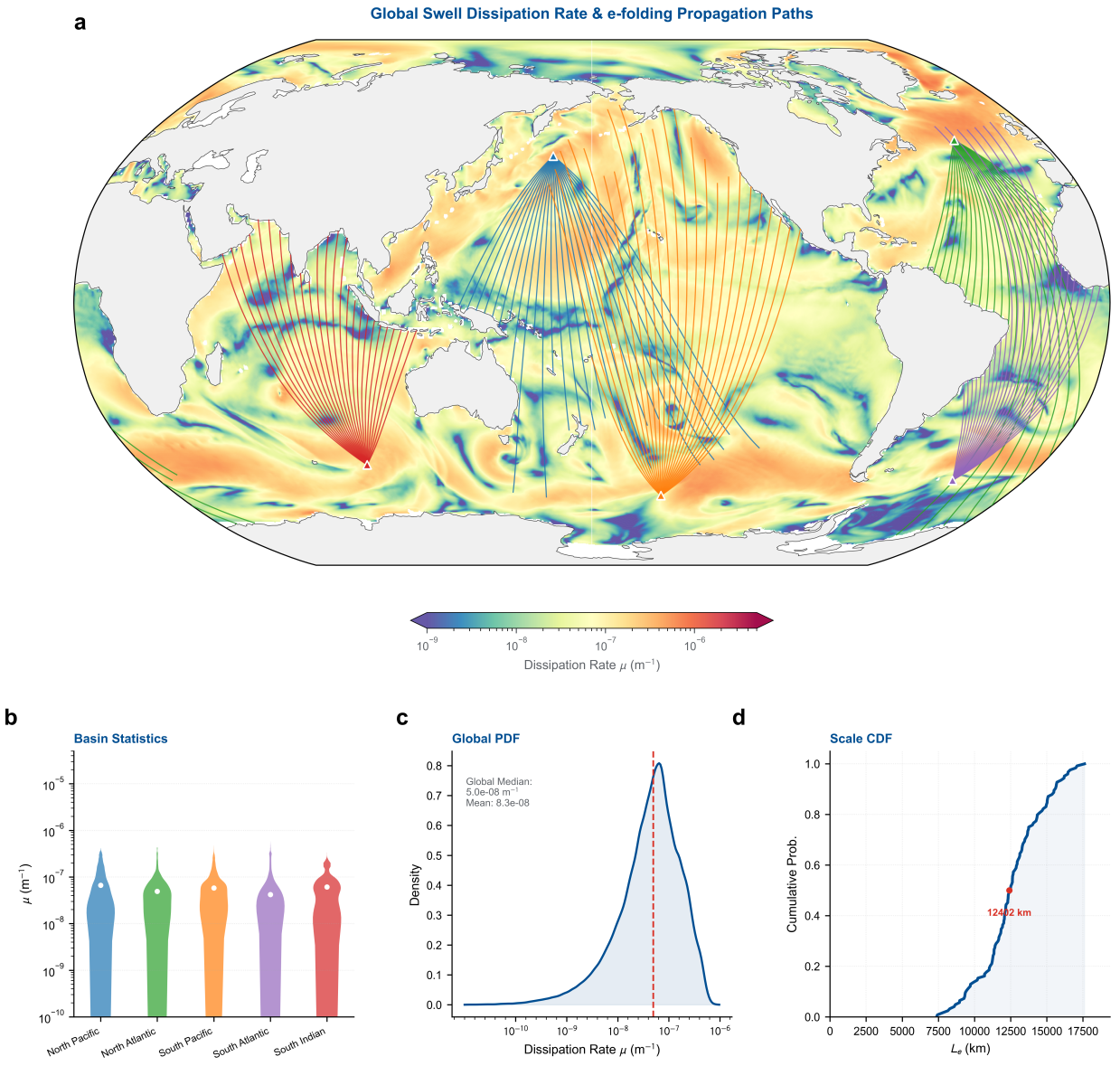

FIG. 3. **Ensemble-mean swell dissipation predicted from the scaling law.** All panels are computed from reanalysis environmental fields and the analytical law $\mu_E = C_{\rm tot}\,\varepsilon_{\rm eff}^{2/3}\,g^{-7/3}\,\omega^{8/3}$ with $C_{\rm tot} = 2\pi/3$. **a**, Physical attenuation rate μ_E for $T = 14$ s swell ($k \approx 0.02$ rad m^{-1}) on 1 January 2005 (00:00 UTC). $\varepsilon_{\rm eff}$ is evaluated from ERA5 10-m wind speeds via the wall-law parameterisation (Supplementary S5 E) with mixed-layer depth from ECCO V4r4. Great-circle rays (25 per source) radiate from five storm-generation zones (triangles) and are truncated where the cumulative path integral $\int_0^L \mu_E\,{\rm d}s$ reaches unity ($L_e = 1/\bar{\mu}_E$). **b**, Basin-resolved violin plots of along-ray μ_E sampled at 20 km intervals. White circles mark medians. Southern Ocean basins show systematically higher attenuation owing to stronger background winds. **c**, Global probability density of μ_E across all ocean grid points (kernel density estimate on $\log_{10}\mu_E$, approximately log-normal). Dashed red line marks the median, and the mean exceeds the median by a factor of ~ 1.5 due to the heavy upper tail in storm-track regions. **d**, Cumulative distribution of e-folding length L_e from each ray's path-averaged $\bar{\mu}_E$. Red dot marks the median (annotated). Swell at $T = 14$ s routinely crosses an entire ocean basin before losing a factor of e in energy, confirming that non-breaking turbulent dissipation acts as a slow but persistent drain over trans-oceanic distances.

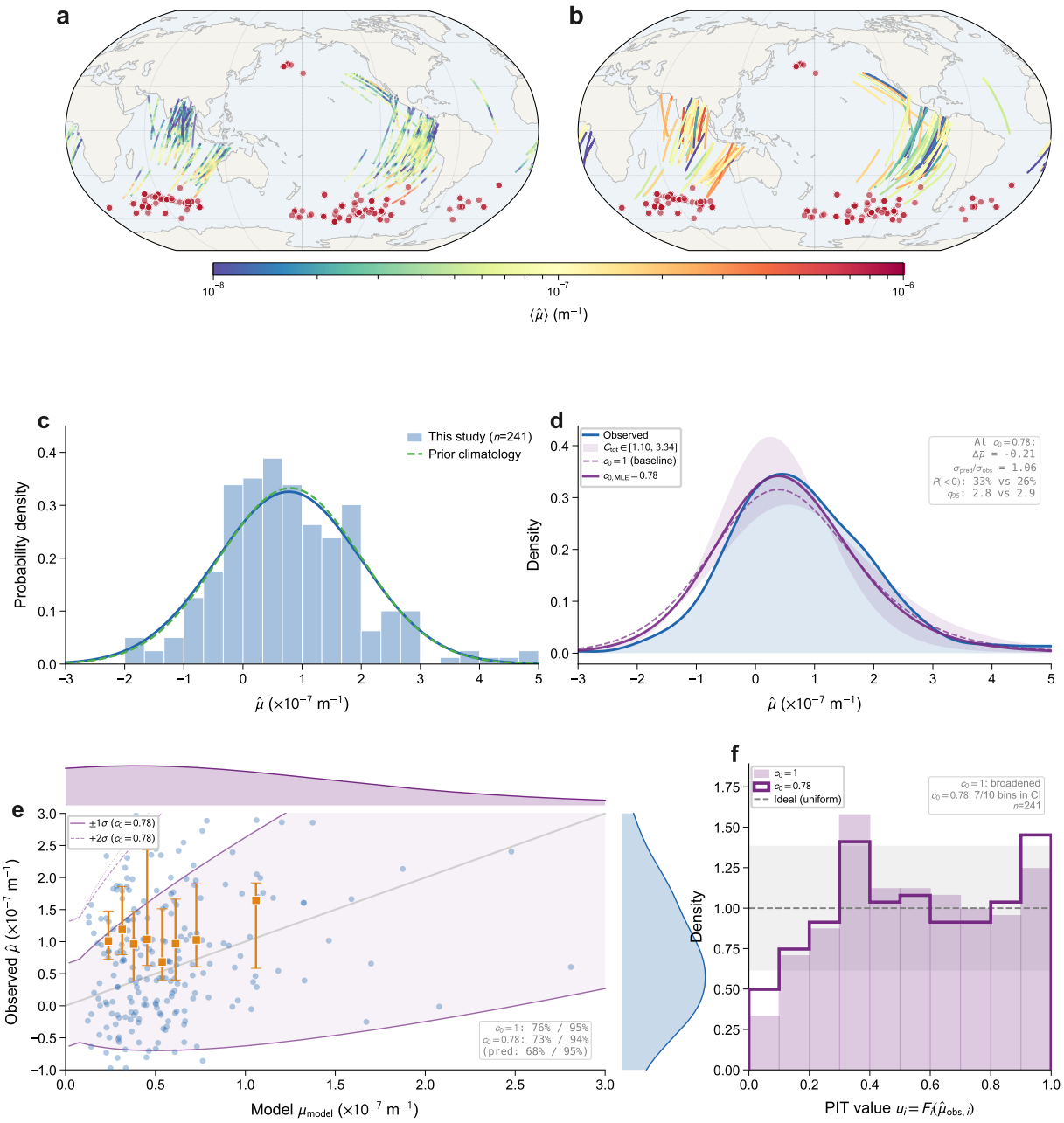

FIG. 4. **Satellite validation of the universal swell attenuation law.** The trackwise observable mean is $\mu_{\mathrm{model},i} = 2\mu_{E,i}^{\mathrm{SVF}} + \mu_{v,i}^{\mathrm{Dore}}$, combining the SVF turbulent prediction with the laminar air-viscous rate[13]. The predictive variance uses only the SVF component, $\mathrm{Var}_{\mathrm{int}}(\hat{\mu}_i) = c_0 \cdot 2\mu_{E,i}^{\mathrm{SVF}}/L_i$ (Dore is deterministic and does not contribute to intrinsic scatter). Panels d-f preview the distribution-level diagnostics developed fully in Fig. 5. **a**, Model-predicted SVF attenuation rate along each observation segment, coloured by $2\,C_{\mathrm{tot}}\varepsilon_{\mathrm{eff}}^{2/3} g^{-7/3}\omega^{8/3}$, evaluated from CCMP V2.0 wind vectors and ECCO V4r4 mixed-layer depths. Red dots mark storm sources. **b**, Satellite-derived attenuation rate $\hat{\mu}$ for the same 241 events, computed from altimeter significant wave height by log-energy regression. Thin dark segments show the pre-observation propagation path. **c**, Probability density of observed $\hat{\mu}$ (histogram) compared with the climatological distribution from Jiang et al.[5] (dashed). **d**, Distribution-level comparison. Blue solid: observed KDE. Purple dashed: predicted mixture at the near-independent-encounter baseline $c_0 = 1$. Purple solid: $c_{0,\mathrm{MLE}} = 0.78$. Shaded band spans the C_{tot} prefactor uncertainty [1.10, 3.34] (Supplementary S5), applied to the SVF component only. Inset reports summary statistics at $c_0 = 0.78$, including bias $\Delta\bar{\mu}$, variance ratio $\sigma_{\mathrm{pred}}/\sigma_{\mathrm{obs}}$, negative fraction (predicted versus observed), and 95th percentile $q_{0.95}$. **e**, Trackwise scatter of observed $\hat{\mu}$ against μ_{model}. Grey diagonal: $y = x$. Purple curves mark the $\pm1\sigma$ and $\pm2\sigma$ prediction envelopes at $c_{0,\mathrm{MLE}} = 0.78$ (representative envelope at median L and μ_v^{Dore}). Gold squares: binned medians with interquartile ranges. Inset reports $1\sigma/2\sigma$ coverage fractions for $c_0 = 1$ and $c_0 = 0.78$ (Gaussian expectation, 68%/95%). **f**, Probability Integral Transform (PIT) histogram. Under a well-calibrated predictive distribution, $u_i = F_i(\hat{\mu}_{\mathrm{obs},i})$ should be uniform (dashed line). Light shading: $c_0 = 1$. Purple outline: $c_0 = 0.78$.

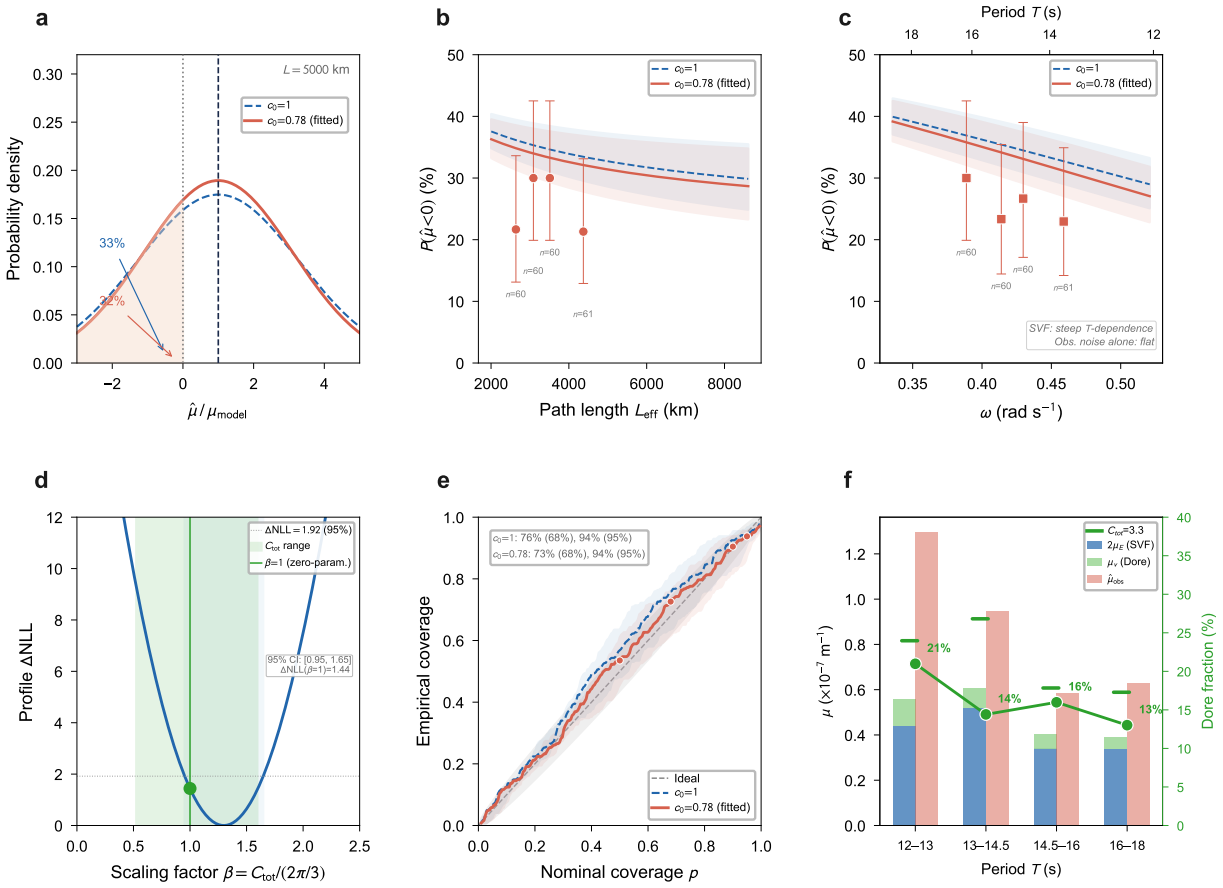

FIG. 5. **Distribution-level validation and attenuation budget across swell events.** The predictive distribution for each track is $\hat{\mu}_i \sim \mathcal{N}\big(\mu_{{\rm model},i},\ c_0\,\mu_{{\rm svf},i}/L_i + \sigma^2_{\rm meas}\big)$, where $\mu_{{\rm model},i} = \mu_{{\rm svf},i} + \mu^{\rm Dore}_{v,i}$ and $\mu_{\rm svf} = 2\mu_E$. The intrinsic variance uses only the SVF component (Dore is deterministic). Two closures are compared, the near-independent-encounter baseline $c_0 = 1$ (blue dashed) and $c_{0,{\rm MLE}} = 0.78$ (red solid). Shaded bands in panels b, c span the $C_{\rm tot}$ uncertainty [1.10, 3.34] (Supplementary S5). **a**, Predicted single-path distribution of $\hat{\mu}/\mu_{\rm model}$ at $L = 5{,}000$ km for both c_0 values. Shaded regions mark the negative-attenuation tail. **b**, Observed negative fraction versus effective path length $L_{\rm eff}$ (circles with Wilson 95% intervals), compared with predictions for both c_0 values. **c**, Same comparison versus peak swell frequency ω (top axis: period T). The steep frequency dependence is a discriminating signature of the $\omega^{8/3}$ law. Measurement noise alone would produce a flat curve. **d**, Profile negative log-likelihood for $\beta = C_{\rm tot}/(2\pi/3)$, marginalised over c_0. Blue shading: 95% CI [0.95, 1.64]. Green band: theoretical $C_{\rm tot}$ range (Supplementary S5). The zero-parameter prediction $\beta = 1$ lies within both. **e**, Reliability diagram: empirical coverage versus nominal coverage p. Grey band: binomial 95% envelope. $c_0 = 1$: 76%/94% at the 68%/95% levels. $c_0 = 0.78$: 73%/94%. **f**, Attenuation budget by period bin (left axis) and laminar fraction (right axis, green). Blue bars: SVF contribution $2\mu_E$. Green bars: laminar viscous[13]. Pink bars: observed median $\hat{\mu}$. Horizontal green ticks: SVF+Dore at the upper $C_{\rm tot}$ bound (3.34), covering the observed medians in all bins. Green circles (right axis): Dore fraction, declining from ∼21% at $T \approx 12$ s to ∼13% at $T \approx 18$ s.

METHODS

Assumptions and projection framework

The derivation requires six assumptions (full discussion in Supplementary S2 A): **A1** (Resolved wave band). A narrow swell band $\mathcal{B}$ admits a linear dispersion relation. Nonlinear wave-wave transfer is negligible on the attenuation time scale. **A2** (Time-scale separation). $\tau_c \sim (k\,c_g)^{-1} \sim \mathcal{O}(1\text{-}5\,\mathrm{s}) \ll \Gamma^{-1} \sim 10^5\text{-}10^6\,\mathrm{s}$. The margin is $\tau_c/\Gamma^{-1} \sim \delta^2 \sim 10^{-6}\text{-}10^{-4}$. **A3** (Bath statistics and phase decoupling). $\boldsymbol{\omega}'$ is locally stationary and homogeneous, statistically independent of the swell phase, with zero ensemble mean $\langle \boldsymbol{\omega}' \rangle = \mathbf{0}$. The swell band contributes $\lesssim \mathcal{O}(10\%)$ of the total near-surface Stokes drift[10, 43], and the observed amplitude-independence of attenuation rates[14, 20] confirms the decoupling empirically. **A4** (Linear truncation). Feedback of order $|a_{\boldsymbol{k}}|^2$ on the bath is negligible. **A5** (Stationary reference measure). $\rho_{\mathrm{ss}} \approx \rho_{\mathrm{wave}} \times \rho_{\mathrm{bath}}$. **A6** (Finite memory). The mode-projected SVF has an absolutely integrable autocorrelation.

The Mori-Zwanzig inner product is $\langle A, B \rangle_\rho = \int A\,B^*\,\rho_{\mathrm{ss}}\,\mathrm{d}\boldsymbol{X}$, and the projector $\mathcal{P}$ onto the swell subspace is $\mathcal{P}A = \sum_{\boldsymbol{k}\in\mathcal{B}} \langle A, a_{\boldsymbol{k}} \rangle_\rho\, a_{\boldsymbol{k}} / \langle a_{\boldsymbol{k}}, a_{\boldsymbol{k}} \rangle_\rho$ (Supplementary S2 B). The resulting generalised Langevin equation is

$$\dot{a}_{\boldsymbol{k}} = \mathrm{i}\,\omega_{\boldsymbol{k}}\,a_{\boldsymbol{k}} - \int_0^t K_{\boldsymbol{k}}(t-s)\,a_{\boldsymbol{k}}(s)\,\mathrm{d}s + F_{\boldsymbol{k}}(t), \tag{7}$$

where $K_{\boldsymbol{k}}(\tau)$ is a memory kernel and $F_{\boldsymbol{k}}(t)$ is the fluctuating force propagated within the orthogonal ($\mathcal{Q} = 1-\mathcal{P}$) subspace. Under A2-A5, $F_{\boldsymbol{k}}$ reduces to the mode projection of the physical SVF:

$$F_{\boldsymbol{k}}(t) = \int \mathrm{d}^3\boldsymbol{x}\;\boldsymbol{\psi}^*_{\boldsymbol{k}}(\boldsymbol{x}) \cdot \big(\boldsymbol{u}_\phi \times \boldsymbol{\omega}'\big)(\boldsymbol{x}, t), \tag{8}$$

where $\boldsymbol{\psi}_{\boldsymbol{k}}$ is the linear velocity eigenfunction of mode $\boldsymbol{k}$, with the normalisation convention $E_{\boldsymbol{k}} = \frac{1}{2}|a_{\boldsymbol{k}}|^2$ (Supplementary S2 A). This identification is physical (a consequence of scale separation and statistical independence), not an algebraic identity of the projector. The discarded contributions are absorbed into the streaming term and into reactive forces whose net work on the swell mode vanishes.

The second fluctuation-dissipation relation (FDR-II)[3, 24] is

$$K_{\boldsymbol{k}}(\tau) = \frac{\langle F_{\boldsymbol{k}}(0)\,F^*_{\boldsymbol{k}}(\tau)\rangle}{\langle |a_{\boldsymbol{k}}|^2 \rangle_{\mathrm{ref}}}. \tag{9}$$

This is an algebraic consequence of the projection operators and holds for any stationary ρ_{ss}. No detailed balance, time reversal, or equilibrium structure is required[44, 45]. The force autocorrelation factorises as $\langle F_{\boldsymbol{k}}(0)\,F^*_{\boldsymbol{k}}(\tau)\rangle = 2E_{\boldsymbol{k}}\,\mathcal{G}_{\boldsymbol{k}}(\tau)$ (Supplementary S2 C), where $\mathcal{G}_{\boldsymbol{k}}$ depends only on bath statistics. This cancels the $E_{\boldsymbol{k}}$ in the denominator of equation (2), making Γ a material property of the bath independent of wave amplitude, analogous to the friction coefficient of a Brownian particle[46], which depends on solvent viscosity but not on the particle's velocity. Under A2 the GLE reduces to the Markovian amplitude equation

$$\dot{a}_{\boldsymbol{k}} = \mathrm{i}(\omega_{\boldsymbol{k}} + \Delta\omega_{\boldsymbol{k}})\,a_{\boldsymbol{k}} - \Gamma(\boldsymbol{k})\,a_{\boldsymbol{k}} + F_{\boldsymbol{k}}(t), \tag{10}$$

with $\Delta\omega_{\boldsymbol{k}} = \int_0^\infty \mathrm{Im}[K_{\boldsymbol{k}}(\tau)]\,\mathrm{d}\tau$ ($|\Delta\omega|/\omega \sim \delta^2 \sim 10^{-6}$-$10^{-4}$, Supplementary S2 G).

Non-negativity of the Green-Kubo damping rate

Because $F_{\boldsymbol{k}}(t)$ is a stationary process with finite variance (A3 i, A5 i, A6), its autocorrelation $C_F(\tau) = \langle F_{\boldsymbol{k}}(0)\,F^*_{\boldsymbol{k}}(\tau)\rangle$ is positive-definite in the sense of Bochner:

$$\sum_{j,\ell} \alpha_j \alpha^*_\ell\, C_F(t_j - t_\ell) \geq 0 \quad \text{for any finite set } \{t_j\}, \{\alpha_j\}. \tag{11}$$

Bochner's theorem[47] guarantees that the power spectral density $S_F(\nu) = \int_{-\infty}^{\infty} C_F(\tau)\,e^{\mathrm{i}\nu\tau}\,\mathrm{d}\tau \geq 0$ for all ν. The Hermitian symmetry $C_F(-\tau) = C_F(\tau)^*$ allows the half-line integral to be written as

$$\int_0^\infty \mathrm{Re}[C_F(\tau)]\,\mathrm{d}\tau = \tfrac{1}{2}S_F(0) \geq 0, \tag{12}$$

so that $\Gamma(\boldsymbol{k}) = S_F(0)/(4E_{\boldsymbol{k}}) \geq 0$. The proof chain is as follows. Stationarity $\Rightarrow$ positive-definiteness $\Rightarrow$ $S_F(\nu) \geq 0 \Rightarrow S_F(0) \geq 0 \Rightarrow \Gamma \geq 0$. No assumption on the bath spectrum enters at any step. The result holds equally for Kolmogorov, viscous, or any intermediate regime, and for wind seas as well as swell (Supplementary S2 F, Theorem 1). Equality ($\Gamma = 0$) requires the zero-frequency spectral density to vanish, $S_F(0) = 0$. A time-independent (frozen) bath is one sufficient condition. Irreversibility requires the eddy field to evolve during the encounter.

Spectral overlap and vertex

Fourier-expanding the SVF and evaluating the mode-projected force autocorrelation along the wave-energy trajectory $\boldsymbol{X}(t) = \boldsymbol{c}_g t$ yields (Supplementary S3 A-D):

$$\Gamma(k) = \frac{1}{2E_k} \int \mathrm{d}^3q \int \mathrm{d}\Omega\; S_u(q,\Omega)\,\big|V(\boldsymbol{q};k)\big|^2\,\mathcal{W}_\Omega(\Omega - \boldsymbol{q}\cdot\boldsymbol{c}_{\mathrm{g}}), \tag{13}$$

where $S_u(q,\Omega)$ is the turbulent velocity spectrum, $|V|^2$ the vortex-force vertex, and $\mathcal{W}_\Omega$ the temporal memory window from the Green-Kubo time integral. For isotropic turbulence the angular integration over eddy orientations gives $\widetilde{G}_{\mathrm{geom}} = 2/3$. Anisotropy extends this to $[2/3,\ 3/4]$ (Supplementary S5 A).

Scale-selection window

The coupling kernel $\mathcal{W}(q/k)$ is suppressed at both extremes of the eddy spectrum (Supplementary S3 D).

At $q \ll k$, Galilean invariance ($q = 0$) and wave-action conservation (q/k first order) force the first irreversible contribution to enter at $\mathcal{O}(q^2/k^2)$. At $q \gg k$, the depth-overlap integral between the wave orbital layer ($\sim k^{-1}$) and the eddy ($\sim q^{-1}$) suppresses coupling as q^{-1} or steeper. The effective vertex is

$$\left|V(\boldsymbol{q};k)\right|^2_{\rm eff} = U_0^2\, q^2\, \widetilde{G}_{\rm geom}\, \mathcal{W}\Big(\frac{q}{k}\Big)\,, \qquad (14)$$

with the baseline analytical window $\widehat{W}(x) = x^2/(1+x^2)^2$ for surface-injected turbulence. The one-parameter family $\widehat{W}_\alpha(x) = x^2/(1+x^2)^\alpha$ spans $\alpha \in [3/2,\, 5/2]$. In all cases the contribution density peaks near $x \approx 1$, confirming scale locality $q \simeq k$ (Supplementary S5 B).

Sweep dominance and closure

The four-dimensional spectrum factorises as $S_u(q,\Omega) = S_u(q)\,\chi(\Omega;q)$ with $\int \chi\,{\rm d}\Omega = 1$, where χ has characteristic width $\omega_q \sim (\varepsilon q^2)^{1/3}$ (the eddy turnover frequency). Inserting this into equation (13) and performing the Ω-integral converts the temporal memory window into an effective correlation time $\tau_{\rm eff}(q;k)$ (Supplementary S3 E). For oceanic swell, $|\boldsymbol{q}\cdot\boldsymbol{c}_g|\,\tau_{\rm eddy} \gg 1$ at all relevant scales, so decorrelation is controlled by advective sweeping rather than eddy turnover:

$$\tau_{\rm eff}(q;k) \;\simeq\; \frac{C_\tau}{q\, c_g(k)}, \qquad (15)$$

with $C_\tau \in [0.89,\, 1.25]$ (Extended Data Fig. 2, Supplementary S5 C). The crossover wavenumber $q_* = \varepsilon/c_g^3$ lies far below the swell wavenumber k for $\varepsilon \lesssim 10^{-6}\,{\rm m^2\,s^{-3}}$. Hence the advective limit applies at all contributing eddy scales.

Combining the angular integral, scale-selection window, advective correlation time, and depth-projection factor $C_E = 1$ (Supplementary S3 D), the one-dimensional Green-Kubo form is

$$\Gamma(k) \;\simeq\; \frac{C_\tau\, \widetilde{G}_{\rm geom}\, U_0^2}{2\, E_k\, c_{\rm g}(k)} \int_0^\infty {\rm d}q\; E_u(q)\, q\, \mathcal{W}\Big(\frac{q}{k}\Big)\,. \qquad (16)$$

Kolmogorov closure

With the Kolmogorov spectrum

$$E_u(q) = C_K\, \varepsilon_{\rm eff}^{2/3}\, q^{-5/3}, \qquad (17)$$

($C_K \approx 1.5 \pm 0.1$[48, 49]), the integrand of equation (16) carries a definite power of q from each factor. $q^{-5/3}$ from the one-dimensional Kolmogorov spectrum $E_u(q)$, q^{+2} from the curl in the vorticity vertex (q^2 in $|V|^2$), q^{-1} from the sweep-dominated correlation time $\tau_{\rm eff} \propto (qc_g)^{-1}$. The net integrand exponent is $-5/3 + 2 - 1 = -2/3$. Changing variables to $x = q/k$:

$$\int_0^\infty {\rm d}q\; q^{-2/3}\, \mathcal{W}\Big(\frac{q}{k}\Big) = k^{1/3} \underbrace{\int_0^\infty x^{-2/3}\, \mathcal{W}(x)\, {\rm d}x}_{C_S}, \qquad (18)$$

yielding $\Gamma(k) \propto k^{1/3}$. The spatial attenuation rate $\mu = 2\Gamma/c_g$ inherits factors of c_g^{-1} and U_0^2/E_k that combine with the dispersion relation $k = \omega^2/g$ to give $\mu(\omega) \propto \omega^{8/3}$ (Supplementary S4). The q^2 from the curl vertex and the q^{-1} from the advective decorrelation are the only factors that depend on the specific physical mechanism. The remaining powers are kinematic bookkeeping. The geometric vertex factor $\widetilde{G}_{\rm geom} = 2/3$ is q-independent and does not affect the exponent.

Independent closure tests on homogeneous isotropic turbulence quantify how accurately the Kolmogorov surrogate reproduces the actual vorticity spectrum within the kernel window. The solenoidal normalisation on 1024^3 JHTDB subvolumes gives $\beta^{\rm sol} = 0.96$, placing the total prefactor $C_{\rm tot}^{\rm DNS} = 2.01$, within 4% of the analytical baseline $2\pi/3 \approx 2.09$ (Extended Data Fig. 4, Supplementary S5 H).

Environmental inputs and path integration

The effective dissipation rate $\varepsilon_{\rm eff}(k)$ is the orbital-weighted depth average of $\varepsilon(z)$ below the breaking layer, evaluated under law-of-the-wall scaling (Supplementary S5 D-E). Wind stress fields are from ERA5 reanalysis[50] (0.25°, 6-hourly) for the global map (Fig. 3) and CCMP V2.0 satellite wind vectors[34, 35] (0.25°, 6-hourly) for the 241-track validation (Fig. 4). Mixed-layer depths are from ECCO V4r4[36] (0.5°, daily). Model predictions along each ray are computed by integrating $\mu(\omega;\varepsilon_{\rm eff}(\boldsymbol{x}))$ along the great-circle path using concurrent data. Storm sources are identified with a local minimum detection algorithm (1000 km exclusion radius).

Comparing theory with satellite tracks requires one additional step. The theoretical quantity μ_E governs the decay of ensemble-mean energy. Satellite altimeters, however, return a finite-length regression estimator $\hat{\mu}_i$ for each track. Its path-averaged expectation equals $2\mu_E$, the Itô correction associated with multiplicative noise (Methods). The model prediction for each track is equation (5), evaluated along the great-circle trajectory using concurrent environmental data.

Satellite data and validation

Observed attenuation rates follow the altimeter tracking method[5]. Along-track $H_{\rm s}$ from Jason-2, Jason-3, and Sentinel-3A. Selection criteria: (i) $\lambda = 250$-500 m, (ii) propagation distance > 2000 km, (iii) directional spread $< 30°$, (iv) $H_{\rm s,swell}/H_{\rm s,total} > 0.7$. After quality filtering, $N = 241$ cases remain (Supplementary S7 B-C). The observed rate:

$$\ln H_{\rm s}(s) = \ln H_{\rm s,0} - \tfrac{1}{2}\,\mu_{\rm obs}\, s. \qquad (19)$$

Statistical diagnostics: PDFs of $\mu_{\rm obs}$ and $\mu_{\rm model}$, paired Wilcoxon signed-rank test, log-ratio $\log_{10}(\mu_{\rm model}/\mu_{\rm obs})$, coverage diagrams. Frequency-scaling tests: $\log_{10}\mu$ versus $\log_{10}\omega$ regression with bootstrap CIs. Variance budget and cross-dataset consistency checks are

in Supplementary S7 D-E. Uncertainty sources: altimeter noise (∼5% in H_s), storm-source localisation (∼100 km), and along-track sampling gaps, propagated to case-by-case error estimates.

Observable bridge and Itô correction

The Markovian dynamics (10) imply that the band-integrated swell energy satisfies

$$\frac{\mathrm{d}E_w}{\mathrm{d}t} = -2\Gamma\, E_w + \tilde{\eta}(t), \tag{20}$$

with noise autocorrelation locked by FDR-II (equation 9):

$$\langle \tilde{\eta}(0)\,\tilde{\eta}(\tau)\rangle = \frac{2D_E}{\tau_c}\, g(\tau/\tau_c), \qquad D_E = 4\,\Gamma\, E_w^2, \tag{21}$$

with g a normalised correlator ($\int_0^\infty g(s)\,\mathrm{d}s = 1$, Supplementary S6 A). Because $D_E \propto E_w^2$, the noise is multiplicative. Passing to $\ln E_w$ introduces an Itô correction. The standard log-slope estimator $\hat{\mu}_i$ therefore measures the sum of the physical damping rate Γ and a noise-induced geometric drift of equal magnitude. Its ensemble mean is systematically larger than the physical energy-loss rate, $\langle\hat{\mu}\rangle = 2\mu_E$, a positive bias that must be corrected before any trackwise altimeter estimate can be compared to μ_E. The derivation of the full pathwise distribution proceeds in four steps.

The instantaneous power delivered to the wave mode is $\dot{W}_k = \mathrm{Re}(a_k^* F_k)$ (Supplementary S6 A). Its autocorrelation $C_{\dot{W}}(\tau)$ involves the product of two bilinear expressions in a_k and F_k. Using the identity $\mathrm{Re}(z_1)\mathrm{Re}(z_2) = \frac{1}{2}\mathrm{Re}(z_1 z_2^*) + \frac{1}{2}\mathrm{Re}(z_1 z_2)$ with $z_1 = a_k^* F_k(0)$, $z_2 = a_k^* F_k(\tau)$. The first average gives $\langle z_1 z_2^*\rangle = 2E_k\, C_F(\tau)$ (since $|a_k|^2 = 2E_k$). The anomalous correlator $\langle z_1 z_2\rangle$ vanishes to leading order by the properness of the narrow-band mode process (equivalently, by translational invariance of the underlying real homogeneous field, Supplementary S6 A). Hence

$$C_{\dot{W}}(\tau) = E_k\, \mathrm{Re}\, C_F(\tau). \tag{22}$$

The factor E_k in $C_{\dot{W}}$ relative to C_F is the structural reason the variance coefficient is twice the drift coefficient at encounter level, yielding $\beta_\xi = 2\alpha$ after FDR-II is applied.

Over one advective correlation time $\tau_{\mathrm{adv}} \sim \ell_c/c_g$, the fractional energy change $\xi \equiv \Delta E/E$ has mean $\langle\xi\rangle = -\alpha\,\delta^2$ with $\alpha = 2\Gamma\tau_{\mathrm{adv}}/\delta^2$ (from the ensemble-mean decay equation (20) and FDR-II), and variance $\mathrm{Var}(\xi) = \beta_\xi\,\delta^2$ with $\beta_\xi = 2\tau_{\mathrm{adv}} I_F/(E_k\delta^2)$ (from equation (22) integrated via the Green-Kubo approximation). The FDR-II relation gives $I_F \equiv \int_0^\infty \mathrm{Re}\, C_F\,\mathrm{d}\tau = 2E_k\Gamma$ (from $\Gamma = I_F/(2E_k)$, equation (2)). Substituting:

$$\beta_\xi = \frac{2\tau_{\mathrm{adv}}\cdot 2E_k\Gamma}{E_k\delta^2} = \frac{4\Gamma\tau_{\mathrm{adv}}}{\delta^2} = 2\alpha, \qquad \text{hence} \quad \frac{\alpha}{\beta_\xi} = \frac{1}{2} \tag{23}$$

This ratio is fixed by FDR-II and the bilinear coupling structure. It is independent of δ, ℓ_c, the shape of $C_F(\tau)$, and E_k (Supplementary S6 A).

Expanding $\Delta\varepsilon \equiv \ln(1+\xi) \approx \xi - \frac{1}{2}\xi^2 + \mathcal{O}(\delta^3)$ and using $\langle\xi^2\rangle = \mathrm{Var}(\xi) + \langle\xi\rangle^2 = \beta_\xi\delta^2 + \mathcal{O}(\delta^4)$:

$$\begin{aligned}\langle\Delta\varepsilon\rangle &= -\alpha\delta^2 - \tfrac{1}{2}\beta_\xi\delta^2 \equiv -A\,\delta^2,\\ A &= \alpha + \tfrac{1}{2}\beta_\xi = \beta_\xi,\\ \mathrm{Var}(\Delta\varepsilon) &= \beta_\xi\,\delta^2 \equiv B\,\delta^2.\end{aligned} \tag{24}$$

The $\frac{1}{2}\beta_\xi$ term in A is the Itô correction, the geometric drift due to multiplicative noise, analogous to the $-\frac{1}{2}\sigma^2$ in geometric Brownian motion.

The ensemble-mean energy decay rate (from S3-S5) is $\mu_E = \alpha\delta^2/\ell_c$, while the satellite estimator mean is $\langle\hat{\mu}\rangle = A\delta^2/\ell_c = (A/\alpha)\mu_E = 2\mu_E$. The estimator variance is $\mathrm{Var}(\hat{\mu}) = B\delta^2/(L\,\ell_c) = (B/\alpha)\mu_E/L = 2\mu_E/L$. Both δ and ℓ_c cancel in these ratios. Here and throughout, "zero-parameter" (or equivalently "parameter-free") refers to the first-moment prediction $\beta = 1$. The second moment has a structural baseline $c_0 = 1$ but is a closure-level prediction that can be renormalised by correlations and non-intrinsic noise.

The intrinsic-variance coefficient is

$$\sigma^2_{\hat{\mu}} = c_0\,\frac{\mu}{L}, \qquad c_0 = \frac{B}{A} = \frac{\beta_\xi}{\beta_\xi} = 1. \tag{25}$$

No specific form for $C_F(\tau)$ has been assumed. No thermal-equilibrium hypothesis enters. The relation between drift and diffusion is inherited from FDR-II and the multiplicative coupling structure (Supplementary S6 B). By the central limit theorem ($N \sim 10^5$ encounters, approximate independence from A6):

$$\hat{\mu}_i \;\sim\; \mathcal{N}\Big(2\,\mu_{E,i},\; \underbrace{\frac{2\,\mu_{E,i}}{L_i}}_{\sigma^2_{\mathrm{intr},i}} + \sigma^2_{\mathrm{meas}}\Big). \tag{26}$$

The factors 2 (mean) and 2 (variance) are exact at leading order in δ. The ratio $c_0 = 1$ is determined by the universal structural ratio $\alpha/\beta_\xi = 1/2$. Because satellite retrievals fit a multi-point ordinary least-squares (OLS) regression rather than a two-endpoint difference, the intrinsic variance acquires an estimator efficiency factor $f(M) = (6/5)(M^2+1)/[M(M+1)]$, where M is the number of effectively independent distance measurements per event (typically 3-15). At these low M, $f(M)$ lies between 1.00 and 1.13 (Supplementary S6 C). Physically significant departures from $c_0 = 1$ arise from $\mathcal{O}(1)$ effects outside the leading-order framework. Turbulence intermittency (enhances variance, pushes c_0 above 1) and weak cross-encounter correlations (pulls in the opposite direction). The expected range is $c_0 \sim 0.5$-2 (Supplementary S6 D).

Negative-rate prediction

The probability of a negative single-track estimate is

$$\begin{aligned}P(\hat{\mu}_i < 0) &= \Phi(-\,\mathcal{S}_{\mathrm{tot},i})\,,\\ \mathcal{S}_{\mathrm{tot},i} &= \frac{\mu_{\mathrm{model},i}}{\sqrt{c_0\,\mu_{\mathrm{svf},i}/L_i + \sigma^2_{\mathrm{meas}}}}\,.\end{aligned} \tag{27}$$

where Φ is the standard normal CDF. The intrinsic signal-to-noise ratio $\mathcal{S}_{\rm int}(\omega) = \sqrt{2\mu_E L} \propto \omega^{4/3}\sqrt{L}$ increases with both frequency and path length. Higher-frequency swell and longer paths yield smaller negative fractions. The frequency and path-length dependences constitute two independent one-sided falsification tests of the $\omega^{8/3}$ exponent through the distribution rather than the mean.

To test whether any global rescaling is required, a multiplicative factor β is applied to both the mean and intrinsic variance:

$$\hat{\mu}_i \;\sim\; \mathcal{N}\Big(2\beta\,\mu_{E,i}^{\rm SVF} + \mu_{v,i}^{\rm Dore},\; c_0\,\frac{2\,\beta\,\mu_{E,i}^{\rm SVF}}{L_i} + \sigma^2_{\rm meas}\Big). \quad (28)$$

The Green-Kubo prediction corresponds to $\beta = 1$. The profile log-likelihood is evaluated over the 241-track sample, profiling over c_0 to obtain the marginal β estimate and vice versa. Model adequacy is assessed via a coverage (reliability) diagram and profile-likelihood confidence intervals (Extended Data Fig. 8). Standardised residuals $z_i = (\hat{\mu}_i - \mu_{{\rm model},i})/\sigma_{{\rm tot},i}$ test normality (Supplementary S7 D-E).

The total variance of single-track estimates decomposes into three mutually independent channels:

$$\sigma^2_{\hat{\mu}} \;=\; \underbrace{\frac{2\,\mu_E}{L}}_{\text{intrinsic}} \;+\; \underbrace{\sigma^2_{\rm env}}_{\text{environmental}} \;+\; \underbrace{\sigma^2_{\rm obs}}_{\text{observational}}, \quad (29)$$

where the intrinsic term follows from equation (26). The environmental term captures variability of $\varepsilon_{\rm eff}$ along propagation paths (propagated through the scaling law on a logarithmic scale, Supplementary S6 F). The observational term collects altimetric noise, spectral partitioning uncertainty, and regression error, estimated from the four independent error sources identified in the altimetric error analysis[5] (Supplementary S7 D). In the predictive distribution (6), the environmental and observational channels are absorbed into $\sigma^2_{\rm meas}$, which therefore represents the total non-intrinsic variance. We adopt $\sigma_{\rm meas} = 0.63 \times 10^{-7}$ m^{-1} as a lower bound reflecting observational errors alone. This maximises the variance attributable to the intrinsic channel and provides the most conservative test of $\beta = 1$. A joint profile likelihood over $(c_0, \sigma_{\rm meas})$ at $\beta = 1$ yields a data-driven estimate $\sigma_{\rm meas} \approx 1.2 \times 10^{-7}$ m^{-1} (95% CI [1.00, 1.38], Extended Data Fig. 6a,c), with the excess over the observational baseline attributable to residual $\varepsilon_{\rm eff}$ prediction error. The first-moment prediction $\beta = 1$ is insensitive to this choice (Extended Data Fig. 6b,c). Because all three physical channels are independent (microscopic encounters, synoptic weather variability, and instrument characteristics), the variances add in quadrature (Extended Data Fig. 9).

ACKNOWLEDGEMENTS

We thank Haoyu Jiang (Shenzhen University) for providing the reprocessed altimeter swell-tracking dataset[5] used throughout this study. This work was supported by Khalifa University of Science and Technology, Abu Dhabi, UAE.

DATA AVAILABILITY

The satellite swell-tracking data used in this study are derived from the reprocessed altimeter dataset[5]. ERA5 reanalysis fields are available from the Copernicus Climate Data Store (`cds.climate.copernicus.eu`). Cross-Calibrated Multi-Platform (CCMP) Ocean Surface Wind Vector Analyses (V2.0) are available from Remote Sensing Systems (`www.remss.com`). ECCO V4r4 daily mixed-layer depth fields are available from the NASA Physical Oceanography Distributed Active Archive Center. Processed data supporting the findings of this study are available from the corresponding author upon reasonable request. The DNS data used for the kernel assessment (Supplementary S5) are from the Johns Hopkins Turbulence Database (JHTDB, `http://turbulence.pha.jhu.edu`).

CODE AVAILABILITY

The code used for data processing, model evaluation, and figure generation is available at https://zenodo.org/records/19135704.

AUTHOR CONTRIBUTIONS

G.L. conceived the theoretical framework, derived all analytical results, performed the numerical and statistical analyses, and wrote the manuscript. M.A. contributed to data analysis and interpretation.

COMPETING INTERESTS

The authors declare no competing interests.

CORRESPONDENCE

Correspondence and requests for materials should be addressed to G.L. (`guoqiang.liu@ku.ac.ae`).

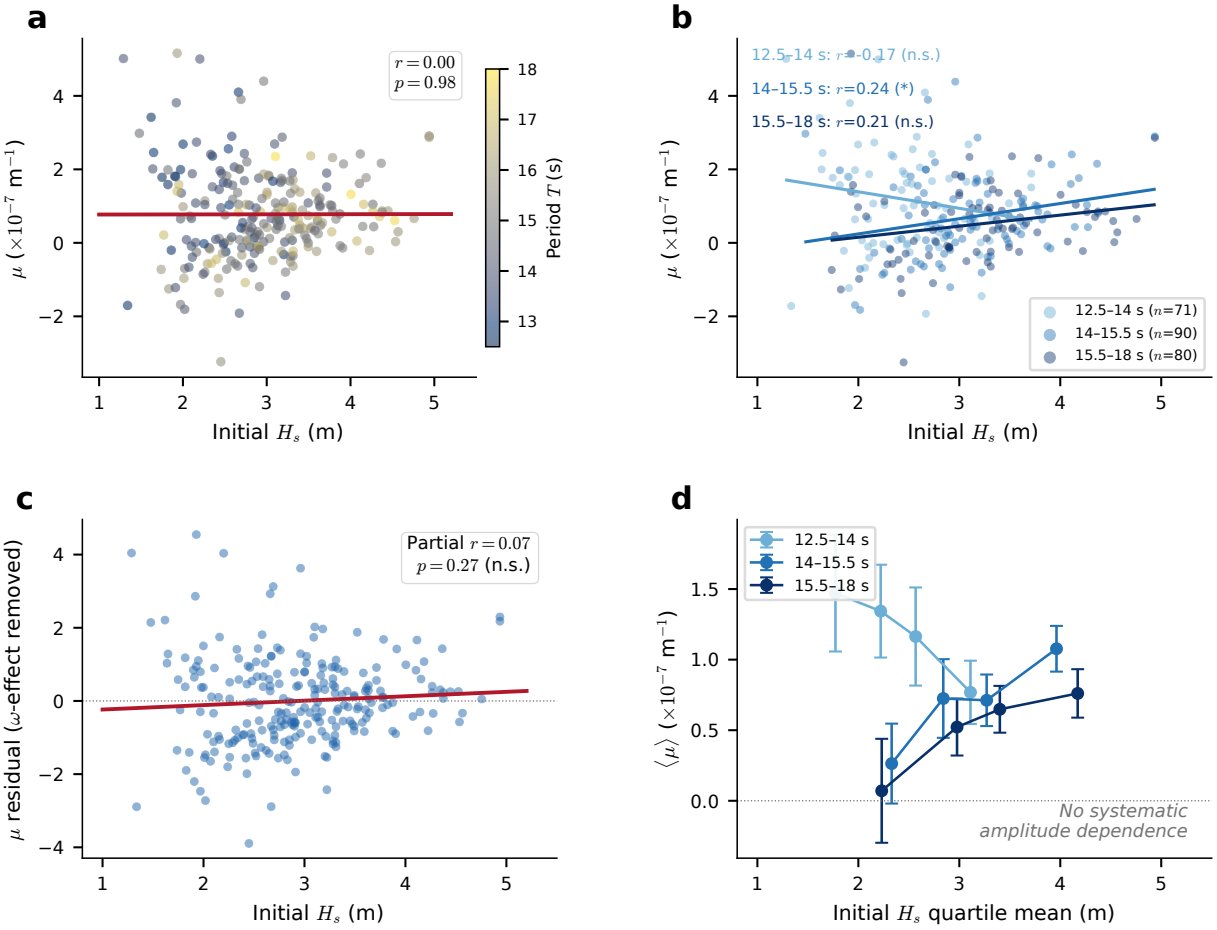

Extended Data Fig. 1. **Amplitude dependence of the attenuation rate. a**, Observed $\hat{\mu}$ versus initial significant wave height $H_{s,0}$ for 241 satellite swell tracks, coloured by wave period. The red line is the ordinary least-squares fit ($r = 0.00$, $p = 0.98$). The empirical amplitude-dependent formulation predicts $\mu_E \propto H_s^2$, implying a factor-of-14 variation across the observed dynamic range, yet none is detected. **b**, Data partitioned into three period bins with regression lines per bin. No bin shows a significant positive trend at the 1% level ($|r| \leq 0.24$, $R^2 \lesssim 0.06$). **c**, Partial correlation after removing the $\omega^{8/3}$ dependence by regression: $r_{\text{partial}} = 0.07$ ($p = 0.27$), confirming no residual amplitude effect. **d**, Quartile-binned mean $\langle\hat{\mu}\rangle$ (± 1 s.e.m.) versus $H_{s,0}$ within each period group, showing no systematic trend. The non-detection is particularly significant because the factor-of-3.8 dynamic range in $H_{s,0}$ would produce a factor-of-14 signal under the empirical amplitude-dependent parameterisation, well above the observational noise floor.

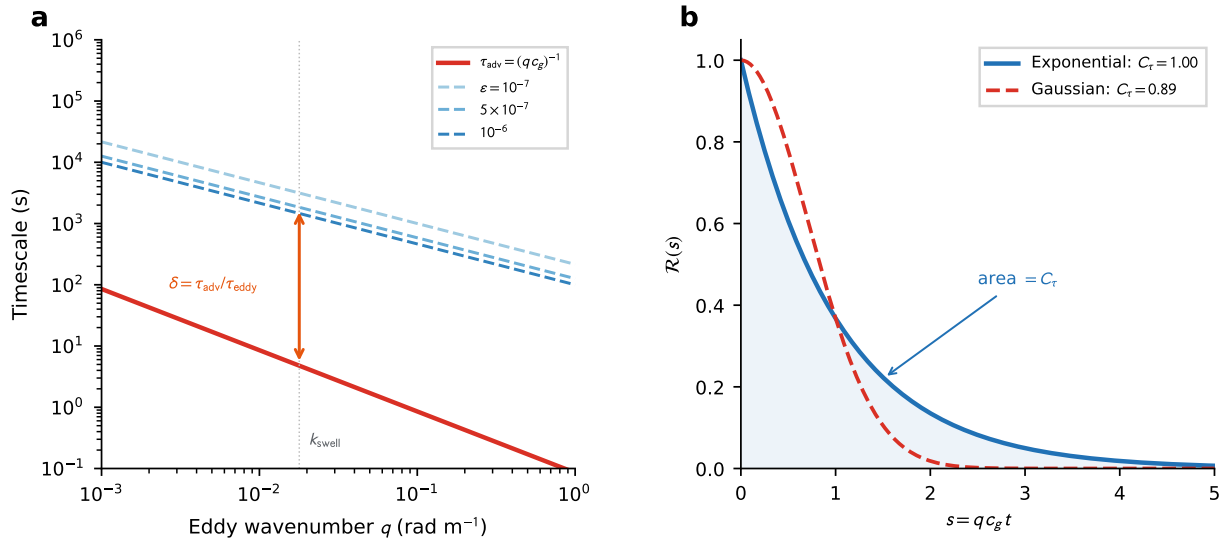

Extended Data Fig. 2. **Decorrelation timescale comparison at swell-selected scales.** The Green-Kubo friction coefficient depends on the autocorrelation time of the stochastic vortex force. Two mechanisms compete to destroy that correlation: eddy turnover, with timescale $\tau_{\rm eddy} \sim (\varepsilon q^2)^{-1/3}$, and advective sweeping by the wave packet, with timescale $\tau_{\rm adv} = (qc_g)^{-1}$. For remote swell the group speed $c_g \sim$ 8-15 $\mathrm{m\,s^{-1}}$ far exceeds mixed-layer turbulent velocities, making sweeping faster by orders of magnitude at all relevant eddy scales. **a**, Timescale comparison for $T = 15\,\mathrm{s}$ swell ($c_g \approx 11.7\ \mathrm{m\,s^{-1}}$). Red: $\tau_{\rm adv}$; blue family: $\tau_{\rm eddy}$ for $\varepsilon = 10^{-7}$, 5×10^{-7}, and $10^{-6}\ \mathrm{m^2\,s^{-3}}$. At the swell wavenumber $k_{\rm swell} \approx 0.018\ \mathrm{rad\,m^{-1}}$ the ratio $\delta = \tau_{\rm adv}/\tau_{\rm eddy} \approx 0.003$, confirming that, during each encounter, the eddy field is quasi-frozen for spatial sampling, even though its weak internal evolution remains essential for irreversibility. **b**, Normalised spatial correlation functions $\rho(s)$ with $s = qc_gt$. Exponential correlator (solid): $C_\tau = 1.00$; Gaussian correlator (dashed): $C_\tau = 0.89$. Shaded area equals C_τ. The physical range $C_\tau \in [0.89, 1.25]$ contributes less than 15% uncertainty to the total prefactor $C_{\rm tot}$, making the theory insensitive to the unknown functional form of the turbulent correlator.

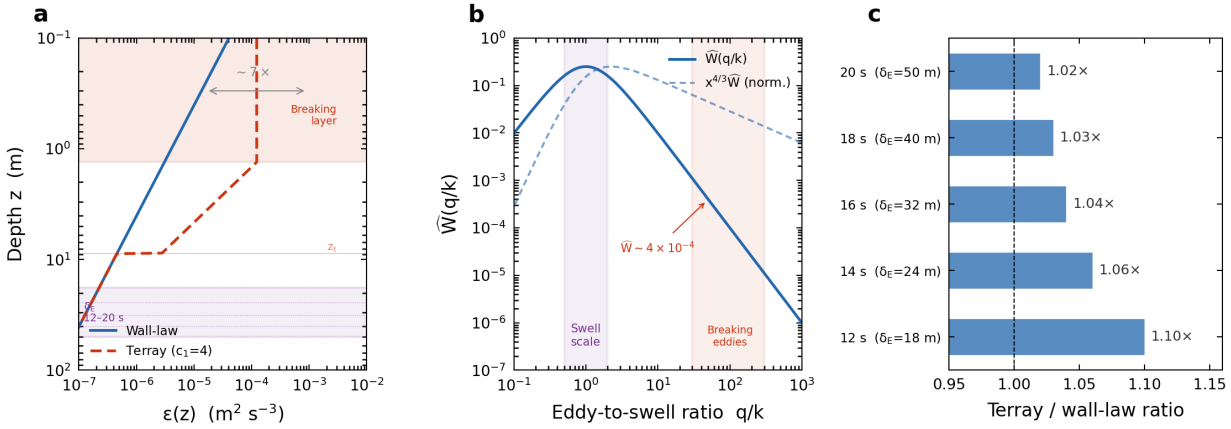

Extended Data Fig. 3. **Breaking-layer contamination test for the swell coupling efficiency.** The effective dissipation rate $\varepsilon_{\rm eff}$ entering the scaling law is the orbital-weighted depth average of the turbulent dissipation profile (Supplementary S5 E). Near-surface wave-breaking eddies could, in principle, bias $\varepsilon_{\rm eff}$ upward, but the scale-selection window suppresses their contribution. Parameters: $U_{10} = 10\ \mathrm{m\,s^{-1}}$, local wind-wave $H_{s,w} = 2.2\,\mathrm{m}$ (Pierson-Moskowitz), swell band $T = 12$-$20\,\mathrm{s}$. **a**, Depth profiles of turbulent dissipation rate $\varepsilon(z)$ under the wall-law model (blue solid) and the Terray surface-enhanced model with $c_1 = 4$ (red dashed). The Terray profile shows three layers: constant dissipation at $z < z_b = 0.6\,H_{s,w} = 1.3\,\mathrm{m}$ (dark shading), power-law decay to $z_t = c_1\,H_{s,w} = 9\,\mathrm{m}$ (light shading), and wall-law asymptote below. Near-surface enhancement reaches $\sim 7\times$. Coloured dotted lines mark the swell orbital penetration depth $\delta_E = (2k)^{-1}$ for periods 12-20 s (purple band), which lies entirely below the breaking layer. **b**, Scale-selection window $\widehat{W}(q/k) = x^2/(1+x^2)^2$ (solid) and spectral contribution density $x^{4/3}\widehat{W}(x)$ (dashed). Swell-scale eddies ($q \sim k$, purple band) dominate the coupling integral. Wind-wave breaking eddies ($q_b/k \sim$ 30-300, red band) are suppressed by $\widehat{W} \sim 4\times10^{-4}$: including them in $\varepsilon_{\rm eff}$ while retaining the baseline C_S would double-count their contribution. **c**, Integrated Terray-to-wall-law ratio for swell damping as a function of swell period, after applying the coupling filter and orbital weight e^{-2kz}. All ratios are within 10% of unity, confirming that the wall-law baseline used throughout this paper is self-consistent with the spectral framework even when near-surface breaking enhancement is present.

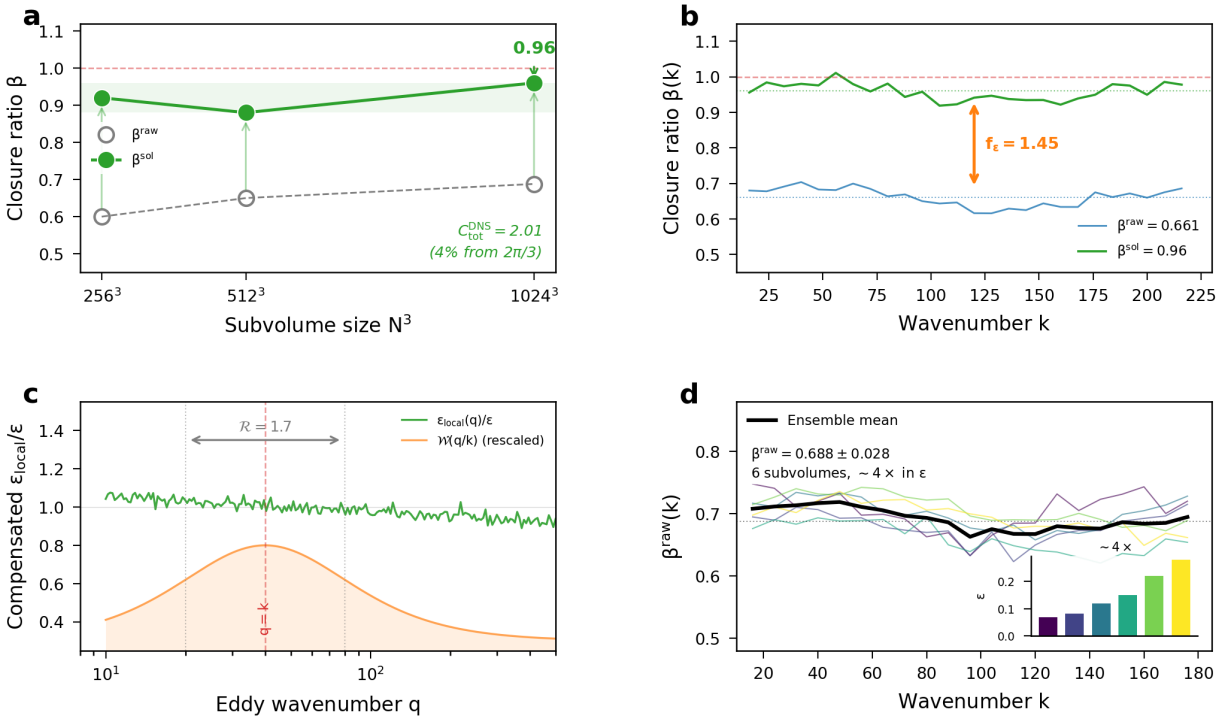

Extended Data Fig. 4. **Kolmogorov closure accuracy on `isotropic8192` DNS turbulence.** The closed-form law replaces the true vorticity spectrum by the Kolmogorov form inside the coupling kernel. This figure tests that replacement on homogeneous isotropic turbulence (HIT) from the JHTDB `isotropic8192` dataset (8192^3, $\mathrm{Re}_\lambda \approx 1300$), using 256^3, 512^3, and 1024^3 subvolumes. **a**, Closure ratio β at three subvolume resolutions. Open circles: raw values biased low by longitudinal spectral leakage from non-periodic FFT. Filled circles: after parameter-free Helmholtz projection. β^{sol} compresses from 0.60-0.69 to 0.88-0.96. The 1024^3 value reaches 0.96 ($C_{\mathrm{tot}}^{\mathrm{DNS}} = 2.01$, 4% from $2\pi/3$). **b**, Wavenumber-resolved closure ratio on the representative 1024^3 subvolume. Blue: $\beta^{\mathrm{raw}} = 0.661$; green: $\beta^{\mathrm{sol}} = 0.96$. The gap is explained by the ε bias ($f_\varepsilon = 1.45$). **c**, Compensated solenoidal spectrum (green) and rescaled scale-selection window $\widehat{W}(q/k)$ (orange shading). The residual non-uniformity across the kernel window produces the 4% departure from unity. **d**, $\beta^{\mathrm{raw}}(k)$ for six independent 1024^3 subvolumes. std = 0.028 despite a $\sim$4$\times$ variation in ε (inset), confirming that β is insensitive to the local dissipation rate. These tests do not validate the SVF mechanism itself (no waves are present) but quantify how accurately the Kolmogorov surrogate reproduces the actual vorticity spectrum within the kernel window. Because oceanic Reynolds numbers far exceed DNS values, this closure error is expected to decrease in the ocean. A separate moving-probe experiment reveals a finite, channel-specific Green-Kubo kernel for the mode-projected SVF in Navier-Stokes turbulence, providing microscopic support for the channel whose macroscopic closure is tested here[38].

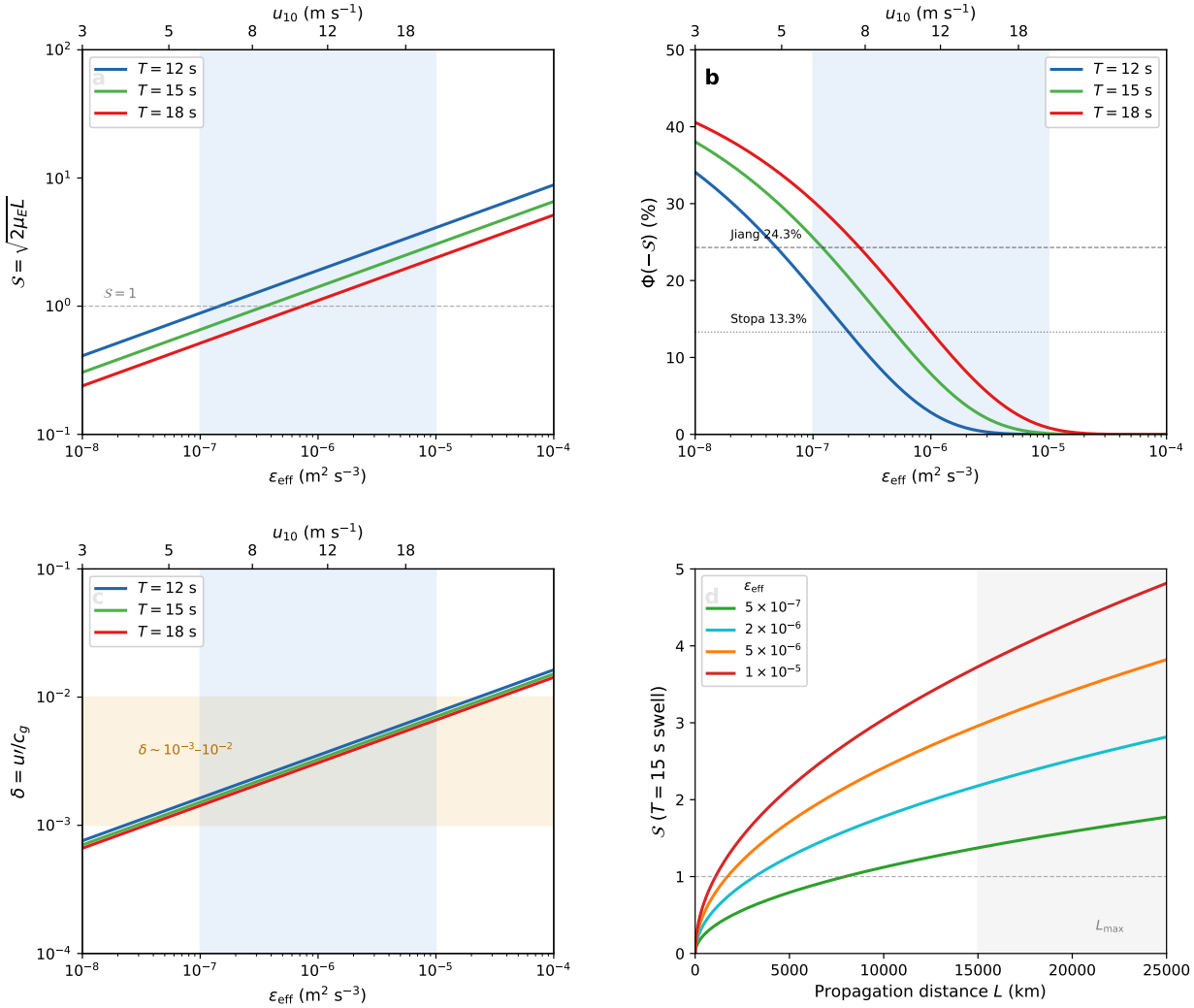

Extended Data Fig. 5. **Signal-to-noise regime of far-field swell tracks.** A single satellite track measures the log-energy slope $\hat{\mu}$, which scatters around the ensemble mean $2\mu_E$ with intrinsic standard deviation $\sqrt{2\mu_E/L}$. The signal-to-noise ratio $\mathcal{S} = \sqrt{2\mu_E L}$ determines whether a given track can resolve the mean: when $\mathcal{S} \lesssim 1$ the negative tail of the estimator distribution extends past zero, producing apparent energy gain. This figure maps $\mathcal{S}$ and the resulting negative fraction across the realistic far-field parameter space. Parameters: $L = 10{,}000$ km, $c_0 = 1$. Upper axes convert $\varepsilon_{\rm eff}$ to indicative 10-m wind speed via the wall-law parameterisation; light blue shading marks the typical far-field range $\varepsilon_{\rm eff} \sim 10^{-7}$-$10^{-5}$ m^2 s^{-3}. **a**, $\mathcal{S}$ versus $\varepsilon_{\rm eff}$ for three swell periods $T = 12$, 15, and 18 s. Shorter-period swell (higher ω) has larger $\mu_E \propto \omega^{8/3}$ and hence higher $\mathcal{S}$. **b**, Predicted negative fraction $\Phi(-\mathcal{S})$ versus $\varepsilon_{\rm eff}$, showing the transition from $\sim$40% (calm, long-period) to $\lesssim$1% (windy, short-period). Dashed lines: observed aggregate fractions from the two datasets. **c**, Small parameter $\delta = u'/c_g$ versus $\varepsilon_{\rm eff}$, confirming $\delta \sim 10^{-3}$-10^{-2} and justifying the weak-coupling expansion underlying the entire framework. **d**, $\mathcal{S}$ versus propagation distance L for $T = 15$ s swell. Because $\mathcal{S} \propto \sqrt{L}$ and trans-oceanic propagation distances are finite, the intrinsic scatter cannot be eliminated by better instruments. It is a fundamental prediction of the theory.

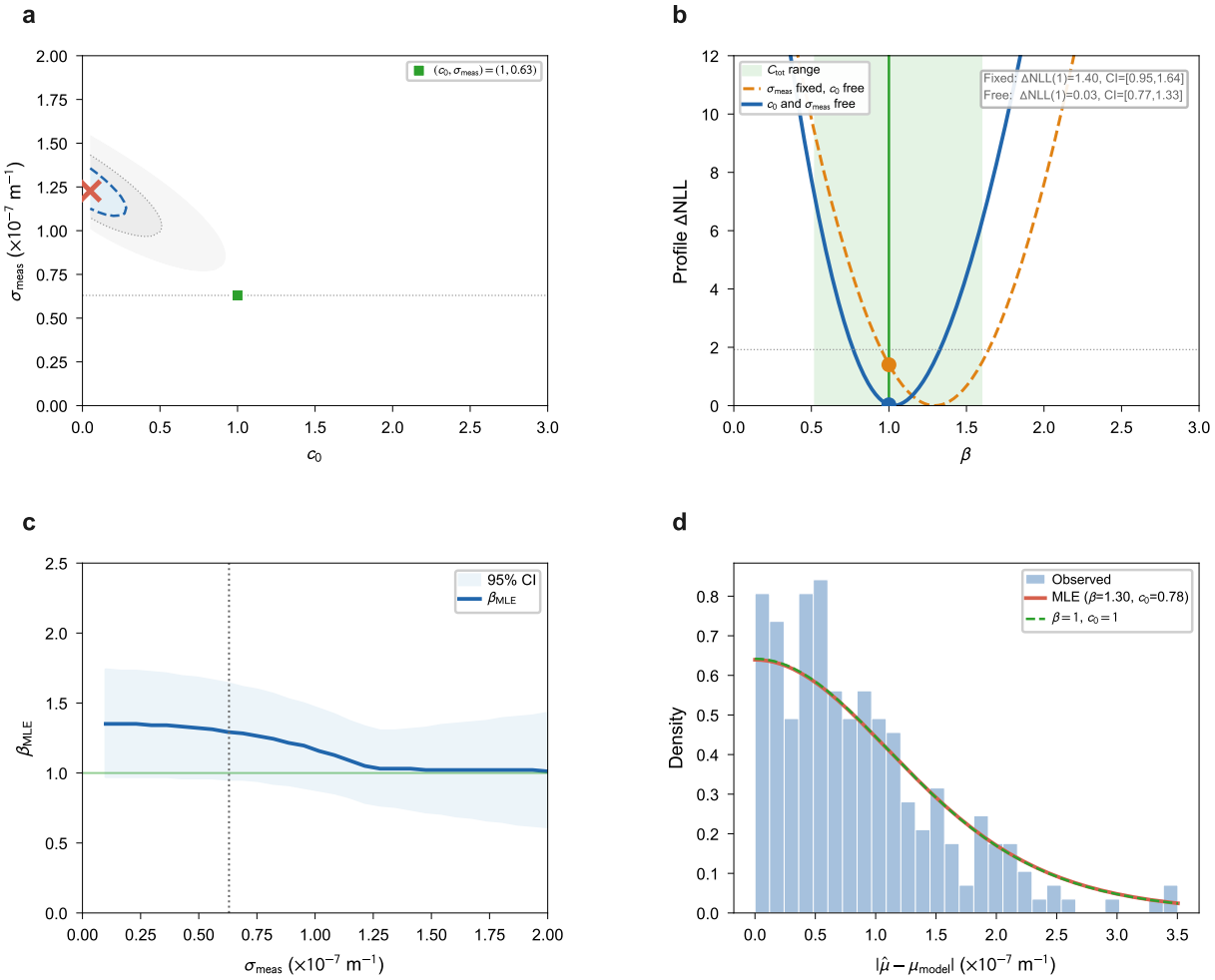

Extended Data Fig. 6. **Joint likelihood analysis confirms the robustness of the zero-parameter mean law to the variance decomposition.** The predictive variance contains two channels: intrinsic encounter noise $c_0\,\mu_{\mathrm{svf},i}/L_i$ and a non-intrinsic term σ^2_{meas}. These are partially degenerate in the likelihood. **a**, Joint ΔNLL at $\beta = 1$ in the $(c_0, \sigma_{\mathrm{meas}})$ plane. Dashed curves: 95% and 99% contours. Red cross: MLE ($c_0 \approx 0.1$, $\sigma_{\mathrm{meas}} \approx 1.25 \times 10^{-7}$ m^{-1}), located on a likelihood ridge along which c_0 and σ_{meas} trade off at nearly constant total variance. Green square: baseline operating point $(c_0, \sigma_{\mathrm{meas}}) = (1, 0.63)$ adopted in Figures 4-5. **b**, Profile ΔNLL for $\beta = C_{\mathrm{tot}}/(2\pi/3)$ under two treatments. Orange dashed: $\sigma_{\mathrm{meas}} = 0.63 \times 10^{-7}$ fixed, c_0 free ($\Delta\mathrm{NLL}(\beta{=}1) = 1.40$; 95% CI [0.95, 1.64]). Blue solid: c_0 and σ_{meas} jointly free ($\Delta\mathrm{NLL}(\beta{=}1) = 0.03$; 95% CI [0.77, 1.33]). Green band: theoretical C_{tot} range [1.10, 3.34] from Supplementary S5. Under both treatments $\beta = 1$ lies well within the 95% CI and the C_{tot} range; with both nuisance parameters free, $\beta = 1$ is nearly indistinguishable from the MLE. **c**, β_{MLE} and its 95% CI (shaded) as a function of the assumed σ_{meas}. The MLE remains in the range 1.0-1.35 and the 95% band includes $\beta = 1$ throughout, confirming that the first-moment prediction is immune to the variance partition. Vertical dotted line: reference value 0.63×10^{-7}. **d**, Absolute residual distribution. Histogram: observed $|\hat{\mu}_i - \mu_{\mathrm{model},i}|$. Red solid: MLE prediction ($\beta = 1.30$, $c_0 = 0.78$). Green dashed: baseline $(\beta, c_0) = (1, 1)$. Both capture the shape of the residuals. $N = 241$.

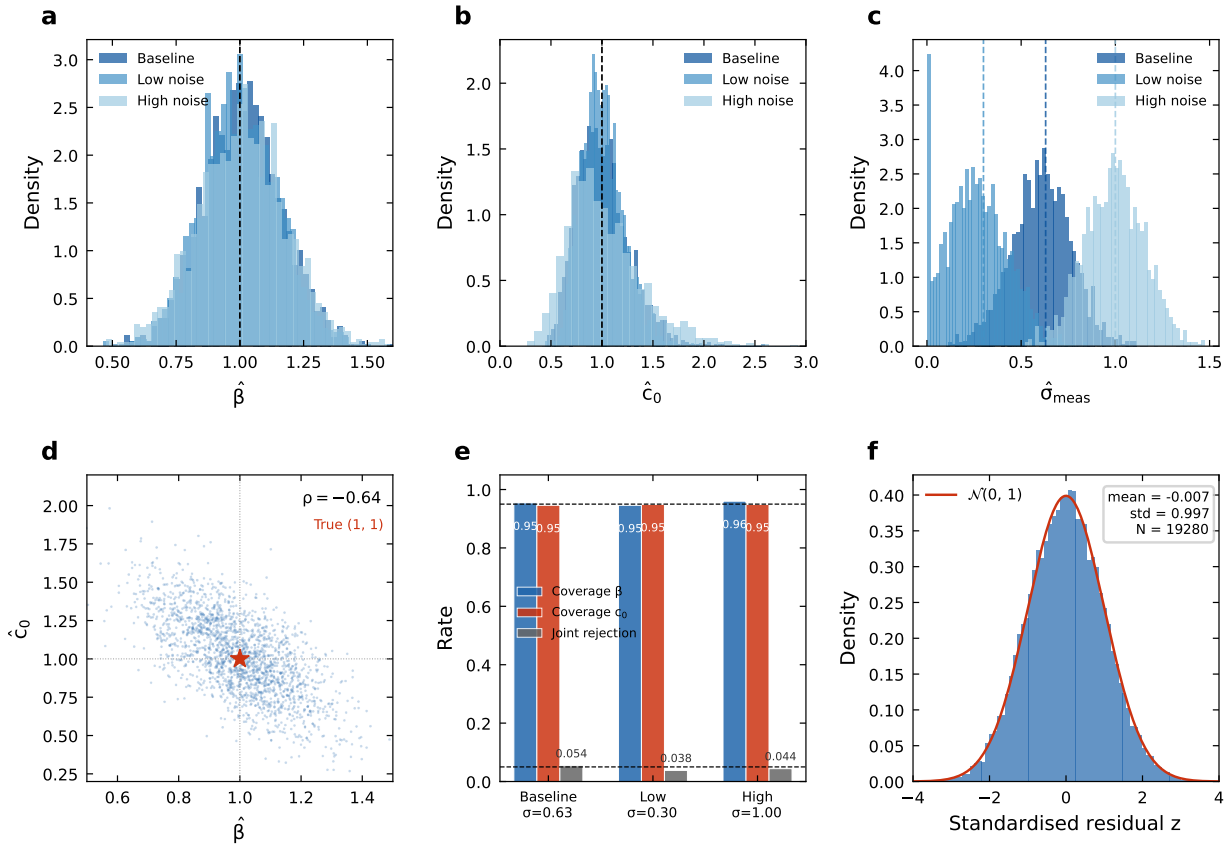

Extended Data Fig. 7. **Fixed-design Monte Carlo validation of the heteroscedastic inference layer.** The 241-track design matrix $(L_i,\, \mu_{\mathrm{svf},i})$ is held fixed and only the observations are regenerated from the model $\hat{\mu}_i \sim \mathcal{N}(\beta^* \mu_{\mathrm{svf},i},\ c_0^* \beta^* \mu_{\mathrm{svf},i}/L_i + \sigma^{*2}_{\mathrm{meas}})$ with $(\beta^*, c_0^*) = (1, 1)$ and $R = 2000$ replications per scenario. Three noise levels are tested: baseline $\sigma^*_{\mathrm{meas}} = 0.63$ (dark shading), low noise 0.30 (medium), and high noise 1.00 (light), all in units of $10^{-7}\,\mathrm{m}^{-1}$. **a**, $\hat{\beta}$ recovery. All three scenarios centre on $\beta^* = 1$ (dashed) with $|\mathrm{bias}| < 0.003$. **b**, $\hat{c}_0$ recovery. The distribution is right-skewed ($c_0 \geq 0$ by construction) but $|\mathrm{bias}| < 0.02$ in every case. **c**, $\hat{\sigma}_{\mathrm{meas}}$ recovery. Dashed lines mark the imposed truth for each scenario. **d**, Joint $(\hat{\beta}, \hat{c}_0)$ cloud for the baseline scenario. The moderate anticorrelation ($\rho \approx -0.64$) reflects a partial trade-off between mean scaling and variance scaling but does not compromise identifiability. **e**, Coverage and joint rejection summary. Profile-likelihood 95% coverage for β (blue) and c_0 (red) is 94.6-96.0% across all scenarios (nominal 95%, dashed line). Joint true-value rejection rates (green) are 3.8-5.4% (nominal 5%). **f**, Pooled standardised residuals from the first 80 baseline replicates ($N = 19{,}280 = 80 \times 241$). Mean 0.003, standard deviation 1.000, consistent with $\mathcal{N}(0, 1)$ (red curve).

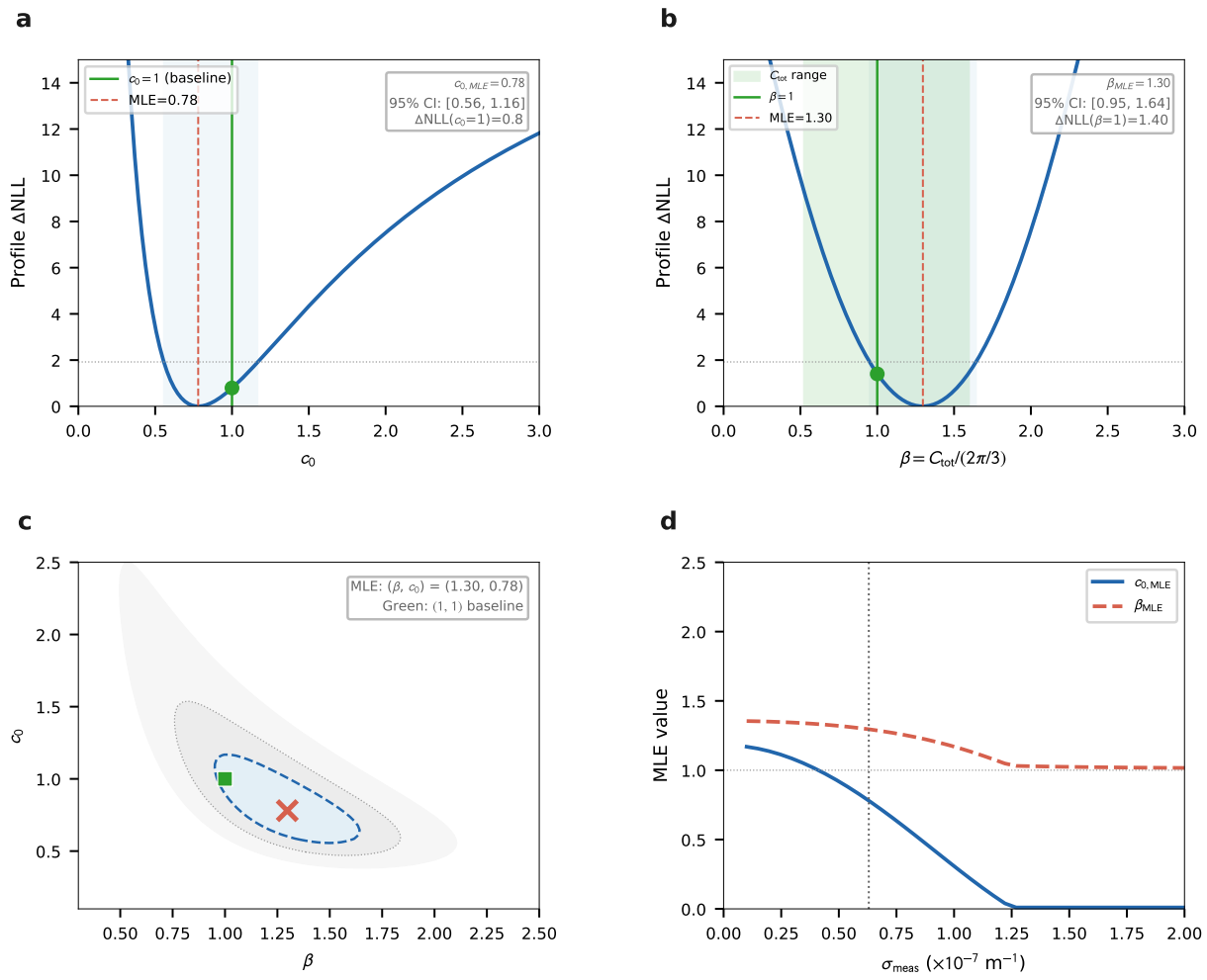

Extended Data Fig. 8. **Likelihood analysis confirms the zero-parameter prediction at both the first- and second-moment levels.** The predictive distribution for each track is $\hat{\mu}_i \sim \mathcal{N}\big(\mu_{\mathrm{model},i},\ c_0 \cdot 2\mu_{E,i}^{\mathrm{SVF}}/L_i + \sigma^2_{\mathrm{meas}}\big)$ where $\mu_{\mathrm{model},i} = 2\beta\mu_{E,i}^{\mathrm{SVF}} + \mu_{v,i}^{\mathrm{Dore}}$; β scales the SVF component while the laminar term remains fixed. The intrinsic variance is proportional to the SVF part alone, because the Dore channel is deterministic. The Green-Kubo zero-parameter prediction corresponds to $\beta = 1$ ($C_{\mathrm{tot}} = 2\pi/3$) with $c_0 = 1$. **a**, Profile negative log-likelihood for c_0 (marginalised over β). $c_{0,\mathrm{MLE}} = 0.78$ (red dashed), 95% CI [0.56, 1.16]. The baseline $c_0 = 1$ (green) lies within the 95% CI ($\Delta\mathrm{NLL} = 0.8$), so the near-independent-encounter second-moment prediction is not rejected. The MLE lying below 1 is consistent with weak inter-encounter correlations that partially cancel the random-walk scatter (Supplementary S6 D). **b**, Profile negative log-likelihood for $\beta = C_{\mathrm{tot}}/(2\pi/3)$, marginalised over c_0. $\beta_{\mathrm{MLE}} = 1.30$, 95% CI [0.95, 1.64]. Green band: theoretical C_{tot} range [1.10, 3.34] (Supplementary S5). $\beta = 1$ falls within both the statistical 95% CI ($\Delta\mathrm{NLL} = 1.40$) and the C_{tot} range. The zero-parameter mean law is not rejected. **c**, Joint (β, c_0) likelihood contour. Dashed curves: 68% and 95% contours. Red cross: joint MLE (β, c_0) = (1.30, 0.78); green square: zero-parameter baseline (1, 1). The baseline sits inside the 95% contour: both moments are simultaneously consistent with the data. **d**, Sensitivity to the assumed measurement noise σ_{meas}. Blue: $c_{0,\mathrm{MLE}}$; red dashed: β_{MLE}. Vertical dotted: reference value $\sigma_{\mathrm{meas}} = 0.63 \times 10^{-7}$ m^{-1}. β_{MLE} stabilises near 1.0-1.3 across the full range; $c_{0,\mathrm{MLE}}$ decreases as more variance is absorbed by σ_{meas}. The first-moment prediction is immune to the variance partition.

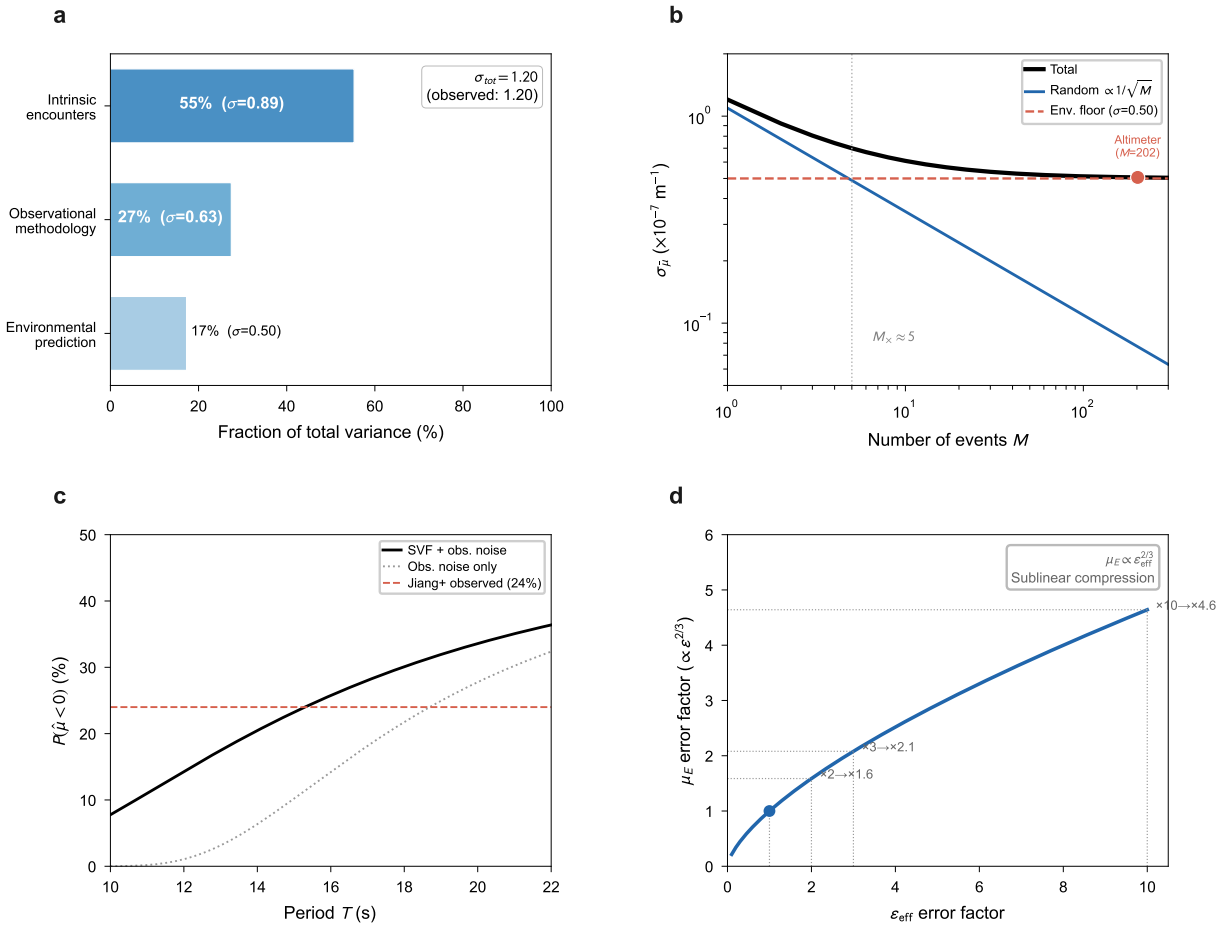

Extended Data Fig. 9. **Variance budget and frequency dependence of the negative tail.** Each satellite-derived attenuation rate $\hat{\mu}$ deviates from the true ensemble mean $2\mu_E$ for three independent reasons: random turbulent encounters along the propagation path (intrinsic), observational methodology errors, and spatial variability of the environment. This figure quantifies the three channels and shows that the frequency dependence of the negative-rate fraction is an unambiguous fingerprint of the intrinsic mechanism. Representative parameters: $\bar{\mu}_{\rm obs} = 0.8{\times}10^{-7}$ m^{-1} ($\mu_E \approx 0.40{\times}10^{-7}$), $L = 10{,}000$ km, $c_0 = 1$. **a**, Variance decomposition. Intrinsic encounter noise contributes 55% of the total variance ($\sigma_{\rm int} = 0.89 \times 10^{-7}$ m^{-1}), observational methodology 27% ($\sigma_{\rm obs} = 0.63$), and environmental prediction 17% ($\sigma_{\rm env} = 0.50$). The predicted total $\sigma_{\rm tot} = 1.20$ is consistent with the observed spread, confirming closure of the variance budget without tuning. **b**, Standard deviation of the ensemble-mean estimator versus number of averaged events M. The crossover $M_\times \approx 5$ separates the random-scatter-limited regime ($\sigma \propto 1/\sqrt{M}$) from the environment-limited floor. The altimeter dataset[5] ($M = 202$) is deeply environment-limited, explaining why adding more tracks cannot sharpen the ensemble mean further. **c**, Frequency-resolved negative-rate fraction $P_{\rm neg}(T)$. Observational noise alone (grey dotted) gives a nearly flat curve; the combined prediction (black solid) shows a steep rise from $\sim$7% at $T = 11$ s to $\sim$28% at $T = 20$ s. This steep frequency dependence is the discriminating signature: it vanishes if the negative rates were purely instrumental. The altimeter-observed aggregate of 24% (red dashed) is consistent with the theory across the observed period range. **d**, Error buffering by the 2/3 exponent in $\mu_E \propto \varepsilon_{\rm eff}^{2/3}$: a factor-of-3 uncertainty in $\varepsilon_{\rm eff}$ compresses to a factor-of-2.1 in μ_E, and even a factor-of-10 error produces less than a factor-of-5 bias. This sublinear compression explains why a climatological estimate of $\varepsilon_{\rm eff}$ suffices for quantitative prediction.

* Corresponding author: guoqiang.liu@ku.ac.ae

[1] M. S. Green, J. Chem. Phys. **22**, 398 (1954).
[2] R. Kubo, J. Phys. Soc. Jpn. **12**, 570 (1957).
[3] R. Zwanzig, *Nonequilibrium Statistical Mechanics* (Oxford University Press, 2001).
[4] F. E. Snodgrass, G. W. Groves, K. F. Hasselmann, G. R. Miller, W. H. Munk, and W. H. Powers, Phil. Trans. R. Soc. Lond. A **259**, 431 (1966).
[5] H. Jiang, J. E. Stopa, H. Wang, R. Husson, A. Mouche, B. Chapron, and G. Chen, J. Geophys. Res. Oceans **121**, 1446 (2016).
[6] W. K. Melville, Annu. Rev. Fluid Mech. **28**, 279 (1996).
[7] A. V. Babanin, *Breaking and Dissipation of Ocean Surface Waves* (Cambridge University Press, 2011).
[8] W. Wang and R. X. Huang, J. Phys. Oceanogr. **34**, 1276 (2004).
[9] N. Rascle, F. Ardhuin, and E. A. Terray, J. Geophys. Res. **111**, C03016 (2006).
[10] S. E. Belcher, A. L. M. Grant, K. E. Hanley, B. Fox-Kemper, L. Van Roekel, P. P. Sullivan, W. G. Large, A. Brown, A. Hines, D. Calvert, A. Rutgersson, H. Pettersson, J.-R. Bidlot, P. A. E. M. Janssen, and J. A. Polton, Geophys. Res. Lett. **39**, L18605 (2012).
[11] B. Fox-Kemper, L. Johnson, and F. Qiao, in *Ocean Mixing* (Elsevier, 2022) pp. 65–94.
[12] F. Ardhuin, E. Rogers, A. V. Babanin, *et al.*, J. Phys. Oceanogr. **40**, 1917 (2010).
[13] B. D. Dore, Geophys. Astrophys. Fluid Dyn. **10**, 215 (1978).
[14] F. Ardhuin, B. Chapron, and F. Collard, Geophys. Res. Lett. **36**, L06607 (2009).
[15] A. D. D. Craik and S. Leibovich, J. Fluid Mech. **73**, 401 (1976).
[16] S. Leibovich, Annu. Rev. Fluid Mech. **15**, 391 (1983).
[17] K. Hasselmann, Boundary-Layer Meteorol. **6**, 107 (1974).
[18] G. J. Komen, L. Cavaleri, M. Donelan, K. Hasselmann, S. Hasselmann, and P. A. E. M. Janssen, *Dynamics and Modelling of Ocean Waves* (Cambridge University Press, 1994).
[19] S. Zieger, A. V. Babanin, W. E. Rogers, and I. R. Young, Ocean Model. **96**, 2 (2015).
[20] J. E. Stopa, F. Ardhuin, and F. Girard-Ardhuin, Geophys. Res. Lett. **43**, 3423 (2016).
[21] G. K. Batchelor, *An Introduction to Fluid Dynamics* (Cambridge University Press, 1967).
[22] J. C. McWilliams, *Quasi-linear Theory for Surface Wave–Current Interactions* (Springer, 2022).
[23] J. C. McWilliams, P. P. Sullivan, and C.-H. Moeng, J. Fluid Mech. **334**, 1 (1997).
[24] H. Mori, Prog. Theor. Phys. **33**, 423 (1965).
[25] R. Zwanzig, Phys. Rev. **124**, 983 (1961).
[26] M. Han, M. Fruchart, C. Scheibner, S. Vaikuntanathan, J. J. de Pablo, and V. Vitelli, Nature Physics **17**, 1260 (2021).
[27] M. D. Chekroun, H. Liu, and J. C. McWilliams, Proc. Natl. Acad. Sci. U.S.A. **118**, e2113650118 (2021).
[28] Y. Katznelson, *An Introduction to Harmonic Analysis*, 3rd ed. (Cambridge University Press, 2004).
[29] F. P. Bretherton and C. J. R. Garrett, Proc. R. Soc. Lond. A **302**, 529 (1968).
[30] M. A. C. Teixeira and S. E. Belcher, J. Fluid Mech. **458**, 229 (2002).
[31] N. S. Oakey, J. Phys. Oceanogr. **12**, 256 (1982).
[32] E. Kunze, J. Phys. Oceanogr. **49**, 385 (2019).
[33] H. Jiang, J. E. Stopa, H. Wang, R. Husson, A. Mouche, B. Chapron, and G. Chen, Remote Sens. Environ. **200**, 446 (2017).
[34] R. Atlas, R. N. Hoffman, J. Ardizzone, S. M. Leidner, J. C. Jusem, D. K. Smith, and D. Gombos, Bull. Amer. Meteor. Soc. **92**, 157 (2011).
[35] C. A. Mears, D. K. Smith, and F. J. Wentz, Remote Sens. **14**, 4083 (2022).
[36] ECCO Consortium, I. Fukumori, O. Wang, I. Fenty, G. Forget, P. Heimbach, and R. M. Ponte, ECCO central estimate, version 4 release 4, PO.DAAC (2021).
[37] Q. Liu, A. V. Babanin, Y. Fan, S. Zieger, C. Guan, and I. R. Young, Ocean Model. **118**, 73 (2017).
[38] G. Liu and M. Al Alshehhi, A moving wave probe reveals a friction kernel hidden by phase averaging in turbulence, EarthArXiv preprint (2026).
[39] F. Qiao, Y. Yuan, Y. Yang, Q. Zheng, C. Xia, and J. Ma, Geophys. Res. Lett. **31**, L11303 (2004).
[40] T. G. Mason and D. A. Weitz, Phys. Rev. Lett. **74**, 1250 (1995).
[41] T. M. Squires and T. G. Mason, Annu. Rev. Fluid Mech. **42**, 413 (2010).
[42] O. Bühler, *Waves and Mean Flows*, 2nd ed. (Cambridge University Press, 2014).
[43] A. Webb and B. Fox-Kemper, Ocean Modelling **40**, 273 (2011).
[44] D. J. Evans and G. P. Morriss, *Statistical Mechanics of Nonequilibrium Liquids*, 2nd ed. (Cambridge University Press, 2008).
[45] U. Marini Bettolo Marconi, A. Puglisi, L. Rondoni, and A. Vulpiani, Physics Reports **461**, 111 (2008).
[46] A. Einstein, Annalen der Physik **322**, 549 (1905).
[47] S. Bochner, Math. Ann. **108**, 378 (1933).
[48] S. B. Pope, *Turbulent Flows* (Cambridge University Press, 2000).
[49] K. R. Sreenivasan, Phys. Fluids **7**, 2778 (1995).
[50] H. Hersbach *et al.*, Q. J. R. Meteorol. Soc. **146**, 1999 (2020).

Supplementary Information for
Fluctuation-induced dissipation for ocean surface waves

Guoqiang Liu[1,*] and Maryam Al Alshehhi[1]

[1]*Civil, Infrastructural and Environmental Engineering,*
Khalifa University of Science and Technology, Abu Dhabi, United Arab Emirates

[*]*Corresponding author: guoqiang.liu@ku.ac.ae*

Contents

The following Sections S1-S9 provide the complete derivation chain from the Navier-Stokes equations to the universal swell attenuation law and its observational predictions. The empirical accuracy of the Kolmogorov closure on DNS turbulence data is assessed within Section S5.

S1. From Navier-Stokes to the stochastic vortex force

We derive the stochastic vortex force (SVF) from the incompressible Navier-Stokes equations under the assumptions stated in the main text (bulk incompressible flow, non-breaking potential waves, negligible air-side friction). We work at leading order in the small wave slope and assume clear separation between the fast wave phase and the slower evolution of currents and turbulent vorticity.

A. Incompressible Navier-Stokes equations and Helmholtz decomposition

Consider an incompressible Newtonian fluid of constant density ρ, neglecting buoyancy, stratification and surface tension. The total Eulerian velocity field $\boldsymbol{U}(\boldsymbol{x}, t)$ satisfies

$$\partial_t \boldsymbol{U} + (\boldsymbol{U} \cdot \nabla)\boldsymbol{U} = -\frac{1}{\rho}\nabla P + \nu \nabla^2 \boldsymbol{U}, \qquad \nabla \cdot \boldsymbol{U} = 0, \tag{S.1}$$

where P is the mechanical pressure (including the hydrostatic contribution $\rho g z$, so that gravity does not appear explicitly) and ν the kinematic viscosity. Following the Helmholtz theorem [1, 2], we decompose the total velocity into an irrotational wave part and a rotational part,

$$\boldsymbol{U}(\boldsymbol{x}, t) = \boldsymbol{u}_\phi(\boldsymbol{x}, t) + \boldsymbol{u}(\boldsymbol{x}, t), \tag{S.2}$$

where $\boldsymbol{u}_\phi = \nabla\phi$ solves the linear free-surface boundary-value problem for the surface-wave potential, and $\boldsymbol{u}$ contains all rotational motions. For small-amplitude, non-breaking surface gravity waves, the potential approximation is standard [e.g. 3–5] and implies

$$\nabla \times \boldsymbol{u}_\phi \approx \boldsymbol{0}, \qquad \nabla \cdot \boldsymbol{u}_\phi = 0 \quad \text{(in the bulk)}. \tag{S.3}$$

Since each component of $\boldsymbol{u}_\phi = \nabla\phi$ satisfies the Laplace equation in the bulk, $\nabla^2 \boldsymbol{u}_\phi = \nabla(\nabla^2\phi) = \boldsymbol{0}$. The bulk viscous term $\nu\nabla^2\boldsymbol{u}_\phi$ therefore vanishes in the interior and drops out of the subtraction below. (Viscous boundary-layer effects on the wave field-Lamb damping-are a separate, much weaker dissipation pathway that is negligible for remote swell and lies outside the present framework.)[1] Since $\boldsymbol{u}_\phi = \nabla\phi$ is irrotational and divergence-free in the bulk, it satisfies the Euler equation for potential flow in the same pressure convention as Eq. (S.1),

$$\partial_t \boldsymbol{u}_\phi + (\boldsymbol{u}_\phi \cdot \nabla)\boldsymbol{u}_\phi = -\frac{1}{\rho}\nabla p^\varphi, \qquad \nabla \cdot \boldsymbol{u}_\phi = 0, \tag{S.4}$$

where p^φ is the irrotational pressure field in the bulk (equivalently, $p^\varphi/\rho = -\partial_t\phi - \frac{1}{2}|\nabla\phi|^2$ via Bernoulli's relation, with gravity already absorbed into the pressure as in Eq. S.1). Substituting (S.2) into (S.1) and subtracting (S.4) eliminates both the irrotational self-advection $\boldsymbol{u}_\phi \cdot \nabla\boldsymbol{u}_\phi$ and the irrotational pressure gradient, giving the governing equation for the rotational component in the bulk (cf. Eq. (2.5) of Xuan et al. 2. Boundary conditions are specified where energy budgets are taken),

$$\partial_t \boldsymbol{u} + (\boldsymbol{u} \cdot \nabla)\boldsymbol{u} = -\boldsymbol{u}_\phi \cdot \nabla\boldsymbol{u} - \boldsymbol{u} \cdot \nabla\boldsymbol{u}_\phi - \frac{1}{\rho}\nabla p + \nu \nabla^2 \boldsymbol{u}, \qquad \nabla \cdot \boldsymbol{u} = 0, \tag{S.5}$$

where p is the pressure associated with $\boldsymbol{u}$ (defined up to an arbitrary function of time). The only approximations are incompressibility and the potential nature of the wave field (S.3).

[1] Throughout Sections S1-S4, z is measured upward with the free surface at $z = 0$ ($z \le 0$ in the fluid, orbital decay $\propto e^{kz}$). Section S5 switches to a depth-downward convention $z \ge 0$, giving kernels e^{-2kz}. The switch is flagged where it occurs (Eq. S.141).

B. Orbital vortex force and its energetic role

We recast the wave-current coupling terms in (S.5) in vortex-force form. Applying the standard vector identity $(\boldsymbol{A}\cdot\nabla)\boldsymbol{B}+(\boldsymbol{B}\cdot\nabla)\boldsymbol{A}=\nabla(\boldsymbol{A}\cdot\boldsymbol{B})-\boldsymbol{A}\times(\nabla\times\boldsymbol{B})-\boldsymbol{B}\times(\nabla\times\boldsymbol{A})$ [e.g. 1] with $\boldsymbol{A}=\boldsymbol{u}_\phi$, $\boldsymbol{B}=\boldsymbol{u}$, noting that $\nabla\times\boldsymbol{u}_\phi\approx\boldsymbol{0}$ (Eq. (S.3)), and absorbing the resulting gradient $\nabla(\boldsymbol{u}_\phi\cdot\boldsymbol{u})$ into a modified pressure $\Pi\equiv p+\rho\,\boldsymbol{u}_\phi\cdot\boldsymbol{u}$, equation (S.5) becomes

$$\boxed{\partial_t\boldsymbol{u}+(\boldsymbol{u}\cdot\nabla)\boldsymbol{u}=\boldsymbol{u}_\phi\times\boldsymbol{\omega}-\frac{1}{\rho}\nabla\Pi+\nu\,\nabla^2\boldsymbol{u},\qquad\nabla\cdot\boldsymbol{u}=0.} \tag{S.6}$$

where $\boldsymbol{\omega}\equiv\nabla\times\boldsymbol{u}$ is the vorticity of the rotational flow. The instantaneous coupling between the wave orbital motion and the rotational flow appears as the instantaneous *orbital vortex force*

$$\boldsymbol{f}_v(\boldsymbol{x},t)\;\equiv\;\boldsymbol{u}_\phi(\boldsymbol{x},t)\times\boldsymbol{\omega}(\boldsymbol{x},t). \tag{S.7}$$

We show that $\boldsymbol{f}_v$ is the *only* term in (S.6) that can exchange energy between the wave field and the rotational flow. Taking the inner product of (S.6) with $\boldsymbol{u}$ and integrating over the fluid volume V,

$$\frac{\mathrm{d}}{\mathrm{d}t}\int_V\tfrac{1}{2}\rho\,|\boldsymbol{u}|^2\,\mathrm{d}V=\rho\int_V\boldsymbol{u}\cdot(\boldsymbol{u}_\phi\times\boldsymbol{\omega})\,\mathrm{d}V-\int_V\boldsymbol{u}\cdot\nabla\Pi\,\mathrm{d}V+\rho\nu\int_V\boldsymbol{u}\cdot\nabla^2\boldsymbol{u}\,\mathrm{d}V-\rho\int_V\boldsymbol{u}\cdot[(\boldsymbol{u}\cdot\nabla)\boldsymbol{u}]\,\mathrm{d}V. \tag{S.8}$$

Under horizontally periodic boundary conditions, a rigid-lid upper surface[2], and sufficient decay of the rotational field at depth ($z\to-\infty$), the pressure gradient term $\boldsymbol{u}\cdot\nabla\Pi=\nabla\cdot(\Pi\boldsymbol{u})$ and the advective nonlinearity $\boldsymbol{u}\cdot[(\boldsymbol{u}\cdot\nabla)\boldsymbol{u}]=\frac{1}{2}\nabla\cdot(|\boldsymbol{u}|^2\boldsymbol{u})$ both integrate to zero by the divergence theorem (the latter redistributes kinetic energy within the rotational subspace but cannot transfer energy to/from the wave). The viscous term gives $\int_V\boldsymbol{u}\cdot\nabla^2\boldsymbol{u}\,\mathrm{d}V=-\int_V|\nabla\boldsymbol{u}|^2\,\mathrm{d}V\le0$ (the integration by parts produces a boundary term $\oint\boldsymbol{u}\cdot(\nabla\boldsymbol{u}\cdot\hat{\boldsymbol{n}})\,\mathrm{d}S$ that vanishes under the adopted periodic/impermeable boundary conditions). The energy budget therefore reduces to

$$\frac{\mathrm{d}}{\mathrm{d}t}\int_V\tfrac{1}{2}\rho\,|\boldsymbol{u}|^2\,\mathrm{d}V=\rho\int_V\boldsymbol{u}\cdot(\boldsymbol{u}_\phi\times\boldsymbol{\omega})\,\mathrm{d}V-\rho\nu\int_V|\nabla\boldsymbol{u}|^2\,\mathrm{d}V, \tag{S.9}$$

confirming that the orbital vortex force $\boldsymbol{u}_\phi\times\boldsymbol{\omega}$ is the sole retained bulk-interior non-viscous channel of energy exchange between swell and rotational motions. Within the potential-wave approximation, the only bulk term that can transfer energy between the two subspaces is this volume integral. Other wave-energy pathways (boundary layers, breaking, air-side stress) are excluded by construction. The viscous term is strictly dissipative and cannot return energy to the wave.

C. Wave-phase averaging, Stokes drift and gradient equivalence

The classical Craik-Leibovich (CL) theory [6–10] describes the effect of non-breaking surface waves on slowly evolving currents by averaging over the fast wave phase. Let $\langle\cdot\rangle_\varphi$ denote this wave-phase (fast-time) average at fixed Eulerian position. (Throughout this paper, $\langle\cdot\rangle_\varphi$ denotes the wave-phase average and $\langle\cdot\rangle$ the ensemble average over the stationary mixed-layer measure ρ_{ss}, defined in Section S2.) Any field A decomposes as

$$A=\overline{A}+A',\qquad\overline{A}\equiv\langle A\rangle_\varphi,\qquad\langle A'\rangle_\varphi=0. \tag{S.10}$$

For a monochromatic deep-water wave propagating along $\hat{\boldsymbol{x}}$ with phase $\varphi\equiv kx-\omega t$, the orbital velocity at a fixed Eulerian position is

$$\boldsymbol{u}_\phi=a\omega\,e^{kz}\big(\cos\varphi\,\hat{\boldsymbol{x}}+\sin\varphi\,\hat{\boldsymbol{z}}\big), \tag{S.11}$$

[2]The rigid-lid approximation for the rotational flow is the energetically consistent companion to the CL framework [6, Eq. (3.16)]. It introduces errors of $O((ak)^2)$ in the energy balance-of order 10^{-4}-10^{-3} for remote swell ($ak\sim0.01$-0.05)-the same order as terms already neglected in the potential-wave approximation. The phase-resolved simulations of Xuan et al. [2] adopt the same boundary treatment at $O(1)$ (their Eq. (A3)).

with a the wave amplitude, ω the angular frequency and k the wavenumber ($\omega^2 = gk$ in deep water). Every component is proportional to $\cos\varphi$ or $\sin\varphi$, so averaging over one full period gives

$$\langle \boldsymbol{u}_\phi \rangle_\varphi = \mathbf{0}, \tag{S.12}$$

exact for the linear wave field at each spatial point. Following McWilliams [6, Chap. 4], we assume clear separation between the wave scales and the mean-flow/turbulence scales. Slowly varying fields have characteristic length scale L and time scale L/V. The waves have wavelength $\lambda \sim 2\pi/k$ and period $T = 2\pi/\omega$. The scale-separation parameter

$$\varepsilon_{\mathrm{CL}} \equiv \frac{V}{C} = \frac{\text{current speed}}{\text{wave phase speed}} \ll 1, \tag{S.13}$$

with $C = \omega/k$ the linear deep-water phase speed, guarantees that any slowly varying field S is effectively constant during a single wave period and can be factored out of the phase average,

$$\langle S\, Q \rangle_\varphi = S\, \langle Q \rangle_\varphi + O\big(\varepsilon_{\mathrm{CL}}/(kL)\big). \tag{S.14}$$

We refer to (S.14) as the *slow-field extraction rule* and invoke it repeatedly below. The error is controlled by the fractional change of the slow field during one wave period. If S evolves on an advective time scale L/V, then $|T\,\partial_t S|/|S| = O\big(V/(\omega L)\big) = O\big(\varepsilon_{\mathrm{CL}}/(kL)\big)$. Under the standard CL scale separation $kL \gg 1$ (slow fields vary weakly over a wavelength), this quantity is small [6, Chap. 4]. More generally, the extraction requires only that S be independent of the fast wave phase, i.e. $T/\tau_S \ll 1$ where τ_S is the characteristic evolution time of S. The estimate L/V is the standard large-scale value in the CL setting. Applying (S.10) to the vorticity gives a split into phase-averaged (slow) and wave-slaved (oscillatory) parts,

$$\boldsymbol{\omega} = \boldsymbol{\Omega}_s + \boldsymbol{\omega}_{\mathrm{wave}}, \qquad \boldsymbol{\Omega}_s \equiv \langle \boldsymbol{\omega} \rangle_\varphi, \qquad \langle \boldsymbol{\omega}_{\mathrm{wave}} \rangle_\varphi = \mathbf{0}. \tag{S.15}$$

The slow vorticity $\boldsymbol{\Omega}_s$ includes all fields that do not depend on the wave phase. It contains both the mean-flow vorticity and the autonomous turbulent vorticity driven by local forcing (wind stress, wave breaking, and buoyancy). Its further decomposition requires a second averaging operation and is carried out in Section D. Let $\boldsymbol{\xi}(\boldsymbol{x}, t) = \int^t \boldsymbol{u}_\phi(\boldsymbol{x}, t')\, \mathrm{d}t'$ be the T-periodic wave-induced displacement, satisfying $\nabla \cdot \boldsymbol{\xi} = 0$ and $\langle \boldsymbol{\xi} \rangle_\varphi = \mathbf{0}$. The Stokes drift is defined in Eulerian form [6, Eq. (3.11)] as

$$\boldsymbol{u}_s(\boldsymbol{x}) \equiv \big\langle (\boldsymbol{\xi} \cdot \nabla) \boldsymbol{u}_\phi \big\rangle_\varphi. \tag{S.16}$$

Unlike $\langle \boldsymbol{u}_\phi \rangle_\varphi = \mathbf{0}$, the Stokes drift is a nonzero *second-order* quantity-the phase average of two correlated first-order oscillatory fields. Within the Generalised Lagrangian Mean (GLM) framework, $\nabla \cdot \boldsymbol{u}_s = 0$ [6, Eq. (3.12), Appendix C]. Finally, we adopt the gradient-equivalence convention

$$\boldsymbol{F} \equiv_\nabla \boldsymbol{G} \quad \Longleftrightarrow \quad \boldsymbol{F} - \boldsymbol{G} = \nabla \chi \ \text{ for some scalar field } \chi(\boldsymbol{x}). \tag{S.17}$$

Two forces that are $\equiv_\nabla$-equivalent have the same curl and produce the same vorticity forcing and volume-integrated power (under the incompressibility and boundary conditions adopted in Eq. (S.9) below), since any gradient can be absorbed into the Bernoulli head. All equalities between forces below are understood in this sense unless stated otherwise.

D. Three-layer vorticity decomposition and the McWilliams identity

The phase-averaged vorticity $\boldsymbol{\Omega}_s \equiv \langle \boldsymbol{\omega} \rangle_\varphi$ introduced in (S.15) contains all fields that vary slowly compared with the wave period. We decompose it further using a second averaging operation-the ensemble average $\langle \cdot \rangle$ over the stationary mixed-layer measure ρ_{ss},

$$\boldsymbol{\Omega}_s = \bar{\boldsymbol{\Omega}} + \boldsymbol{\omega}', \qquad \bar{\boldsymbol{\Omega}} \equiv \langle \boldsymbol{\Omega}_s \rangle = \big\langle \langle \boldsymbol{\omega} \rangle_\varphi \big\rangle, \qquad \langle \boldsymbol{\omega}' \rangle = \mathbf{0}. \tag{S.18}$$

Here $\bar{\boldsymbol{\Omega}}$ is the ensemble-mean vorticity of the mean flow and $\boldsymbol{\omega}' \equiv \boldsymbol{\Omega}_s - \bar{\boldsymbol{\Omega}}$ is the zero-ensemble-mean vorticity fluctuation. Physically, $\boldsymbol{\omega}'$ is driven predominantly by local forcing (wind stress, wave breaking, buoyancy) and the turbulent cascade, not by the remote-source swell-a characterisation formalised in Assumptions A3 and A5 (Section S2) and supported by the energetic estimates therein. Under standard ergodicity assumptions, the ensemble mean coincides with the Reynolds mean used in turbulence theory.

A notational convention. From Eq. (S.18) onward, the overbar denotes the *ensemble* mean ($\bar{\boldsymbol{\Omega}} \equiv \langle \boldsymbol{\Omega}_s \rangle$) and the prime the turbulent fluctuation ($\boldsymbol{\omega}' \equiv \boldsymbol{\Omega}_s - \bar{\boldsymbol{\Omega}}$), replacing the earlier phase-decomposition usage. The two averaging operators are always distinguished by the bracket subscript, $\langle\cdot\rangle_\varphi$ for phase, $\langle\cdot\rangle$ for ensemble. Combined with (S.15), this gives the *three-layer* decomposition of the total vorticity,

$$\boxed{\boldsymbol{\omega} = \bar{\boldsymbol{\Omega}} + \boldsymbol{\omega}' + \boldsymbol{\omega}_{\text{wave}}.} \tag{S.19}$$

The first step (phase averaging, yielding $\boldsymbol{\Omega}_s$ and $\boldsymbol{\omega}_{\text{wave}}$) follows the standard CL framework of McWilliams [6], who treats $\boldsymbol{\Omega}_s$ as a single deterministic slow field. The second step is where the statistical-mechanical structure enters. By splitting $\boldsymbol{\Omega}_s$ into its ensemble mean $\bar{\boldsymbol{\Omega}}$ and the zero-mean turbulent fluctuation $\boldsymbol{\omega}'$, we assign the roles that the Mori-Zwanzig formalism (Section S2) will formalise: the swell amplitude is the slow observable, and $\boldsymbol{\omega}'$ is the fast bath whose autonomous dynamics supply both the random force and the dissipation kernel. This separation is absent in the CL framework, whose design target is the phase-averaged wave-induced forces acting on the slow-time current evolution, not wave dissipation [6, Chap. 11]. Within CL, $\boldsymbol{\Omega}_s$ enters diagnostically as a given field. For any configuration of the slow flow it determines the Stokes vortex force $\boldsymbol{u}_s \times \boldsymbol{\Omega}_s$. As a deterministic framework, CL does not introduce the statistical-mechanical structure (ensemble averaging, autocorrelation functions) from which a friction coefficient could be constructed. Wave dissipation is explicitly left to other mechanisms [6, p. 54]. Our contribution is to show that the dissipation mechanism is already encoded in the CL vortex-force decomposition. It is the fluctuating component $\boldsymbol{u}_\phi \times \boldsymbol{\omega}'$, which requires retaining the phase-resolved orbital velocity and adding a statistical-mechanical projection over the bath degrees of freedom.

The wave orbital motion tilts and stretches the slow vorticity $\boldsymbol{\Omega}_s$, generating $\boldsymbol{\omega}_{\text{wave}}$ as a phase-locked oscillation. Taking the curl of (S.6) gives the vorticity equation $\partial_t \boldsymbol{\omega} = \nabla \times [(\boldsymbol{u}_\phi + \boldsymbol{u}) \times \boldsymbol{\omega}] + \nu \nabla^2 \boldsymbol{\omega}$. On the fast wave timescale T, $\boldsymbol{\Omega}_s$ is effectively frozen ($T/\tau_{\text{eddy}} \ll 1$). Decomposing $\boldsymbol{\omega} = \boldsymbol{\Omega}_s + \boldsymbol{\omega}_{\text{wave}}$ in the wave-driven term $\nabla \times (\boldsymbol{u}_\phi \times \boldsymbol{\omega})$, the leading-order contribution is $\nabla \times (\boldsymbol{u}_\phi \times \boldsymbol{\Omega}_s)$. The feedback $\nabla \times (\boldsymbol{u}_\phi \times \boldsymbol{\omega}_{\text{wave}})$ is $O(ak)$ relative to this, because $\boldsymbol{\omega}_{\text{wave}}/\boldsymbol{\Omega}_s = O(ak)$. Iterating, it produces corrections to $\boldsymbol{\omega}_{\text{wave}}$ at $O((ak)^2)$ relative to $\boldsymbol{\Omega}_s$. The rotational self-interaction $\nabla \times (\boldsymbol{u} \times \boldsymbol{\omega})$ is $O(\varepsilon_{\text{CL}})$ relative to the wave-driven term. Both are negligible at leading order. Hence $\partial_t \boldsymbol{\omega}_{\text{wave}} \approx \nabla \times (\boldsymbol{u}_\phi \times \boldsymbol{\Omega}_s)$. Writing $\boldsymbol{u}_\phi = \partial_t \boldsymbol{\xi}$ and noting that $\boldsymbol{\Omega}_s$ does not depend on the fast time, the time integration acts only on $\boldsymbol{\xi}$ (with $\nabla \cdot \boldsymbol{u}_\phi = 0$ and $\nabla \cdot \boldsymbol{\Omega}_s = 0$ simplifying the curl-of-cross product), giving

$$\boldsymbol{\omega}_{\text{wave}} \approx \nabla \times (\boldsymbol{\xi} \times \boldsymbol{\Omega}_s). \tag{S.20}$$

No additional long-wavelength expansion of $\boldsymbol{\Omega}_s$ is required. The derivation is carried out at a fixed Eulerian position, with $\nabla\boldsymbol{\Omega}_s$ treated as the given spatial derivative field wherever it appears. The only approximation is temporal freezing, with corrections of $O(T/\tau_{\text{eddy}})$. This is the particular (forced) solution of the linearised vorticity equation. It carries no independent degrees of freedom. It is entirely determined by the wave kinematics ($\boldsymbol{\xi}$) and the full slow vorticity $\boldsymbol{\Omega}_s$, and oscillates synchronously with the wave. Because it is linear in $\boldsymbol{\Omega}_s$,

$$\boldsymbol{\omega}_{\text{wave}} = \underbrace{\nabla \times (\boldsymbol{\xi} \times \bar{\boldsymbol{\Omega}})}_{\text{driven by mean vorticity}} + \underbrace{\nabla \times (\boldsymbol{\xi} \times \boldsymbol{\omega}')}_{\text{driven by turbulent vorticity}}. \tag{S.21}$$

The first term is deterministic, the second stochastic but phase-locked to the wave (proportional to $\boldsymbol{\xi}$).

The autonomous turbulent vorticity $\boldsymbol{\omega}' = \boldsymbol{\Omega}_s - \bar{\boldsymbol{\Omega}}$ is driven by local forcing and the turbulent cascade, not by the remote swell. It therefore carries no dependence on the fast wave phase at a fixed Eulerian position and is approximately frozen over one wave period: $\tau_{\text{eddy}} \sim \ell/u' \gg T$. Statistical independence from the wave phase is a separate statement from this kinematic freezing and follows from the remote

origin of swell. For trans-oceanic swell generated by a distant storm, the local realisation of $\boldsymbol{\omega}'$ carries no information about the wave phase at a fixed point on the ray. The local turbulence is driven by local wind, breaking and buoyancy forcing, whereas the swell phase is set by conditions thousands of kilometres away. This physical decoupling underpins the phase-independence assumption A3(ii) formalised in Section S2.

On the wave timescale, $\boldsymbol{\omega}'$ therefore looks the same as $\bar{\boldsymbol{\Omega}}$ in the narrow sense that both are approximately constant during one period T. The critical distinction lies in their *internal structure*:

1. $\bar{\boldsymbol{\Omega}}$ is the ensemble-mean vorticity, a single deterministic vector at each position, with no internal degrees of freedom accessible to the wave. Its contribution to $\boldsymbol{\omega}_{\text{wave}}$ (Eq. S.21) is a periodic oscillation synchronous with the wave phase. Any work done during one half-cycle is returned during the other, yielding zero net energy transfer over a full period.

2. $\boldsymbol{\omega}'$, by contrast, is a full turbulent field possessing its own internal degrees of freedom, including the full hierarchy of the turbulent cascade and local forcing. Although $\boldsymbol{\omega}'$ is approximately frozen on the wave timescale, its internal dynamics continuously redistribute energy among its modes on the eddy-turnover time ℓ/u'. During a single wave period, a small fraction $T\,u'/\ell \sim O(10^{-2})$ of any energy injected by the wave into an eddy is redistributed among the eddy's internal modes before the wave phase returns to its original value. This small but nonzero redistribution prevents exact energy return.

This distinction, the presence or absence of internal degrees of freedom, is the microscopic origin of irreversibility in the SVF theory, analogous to the distinction between elastic scattering off a rigid wall and inelastic scattering off a thermal-bath molecule (Section S2 I).

The connection between the wave-slaved coupling and the Stokes-drift form used in CL theory is established by the McWilliams identity [6, Appendix G]. For any solenoidal field $\boldsymbol{Z}$ that is independent of the fast wave phase (i.e. varies only on timescales $\gg T$),

$$\left\langle \boldsymbol{u}_\phi \times \left[\nabla \times (\boldsymbol{\xi} \times \boldsymbol{Z})\right]\right\rangle_\varphi = \boldsymbol{u}_s \times \boldsymbol{Z} + \nabla C, \tag{S.22}$$

where C is a scalar field. The identity rectifies a quadratic wave-phase correlation into the Stokes-drift form. It is linear in $\boldsymbol{Z}$ and relies on small slope, incompressibility, and phase-independence of $\boldsymbol{Z}$ [6, Appendix G]. To verify (S.22), one expands $\nabla \times (\boldsymbol{\xi} \times \boldsymbol{Z})$ via the BAC-CAB identity, takes the cross product with $\boldsymbol{u}_\phi$, and phase-averages term by term using the explicit orbital velocity (S.11). The key step is that the second-order correlator $\langle u_i^\varphi\, \partial_j \xi_k \rangle_\varphi$ evaluates, by direct calculation with the deep-water eigenfunction, to a combination of Stokes-drift components and gradient corrections. Collecting terms yields the right-hand side of (S.22). A self-contained proof occupies approximately two pages of vector algebra and is given in McWilliams [6, Appendix G].

Remark 1 (Assumptions behind the McWilliams identity) *Identity* (S.22) *is a kinematic consequence of wave-period averaging of quadratic wave quantities. It requires only that* $\boldsymbol{Z}$ *be solenoidal and independent of the fast wave phase, so that it may be treated as frozen in time during the one-period phase average. No additional weak-spatial-variation assumption is required for the identity itself beyond the conditions stated in McWilliams [6, Appendix G]. Any spatial dependence of* $\boldsymbol{Z}$ *enters only through gradient terms that are absorbed into* ∇C*. Since* $\nabla \times (\nabla C) = \boldsymbol{0}$*, such terms do not affect the vorticity forcing. The fact that the residual term indeed takes pure gradient form is proved in McWilliams [6, Appendix G, Eq. (G.7)] for* any *non-divergent* $\boldsymbol{Z}$*. Separately, the approximation* (S.20) *for the wave-slaved vorticity relies on temporal scale separation (*$\partial_t \boldsymbol{\Omega}_s$ *negligible over one wave period), with corrections controlled by* T/τ_{slow} *for the relevant slow component.*

Setting $\boldsymbol{Z} = \boldsymbol{\Omega}_s = \bar{\boldsymbol{\Omega}} + \boldsymbol{\omega}'$ in (S.22) and using (S.20),

$$\langle \boldsymbol{u}_\phi \times \boldsymbol{\omega}_{\text{wave}} \rangle_\varphi \equiv_\nabla \boldsymbol{u}_s \times \boldsymbol{\Omega}_s = \boldsymbol{u}_s \times \bar{\boldsymbol{\Omega}} + \boldsymbol{u}_s \times \boldsymbol{\omega}'. \tag{S.23}$$

The first term, $\boldsymbol{u}_s \times \bar{\boldsymbol{\Omega}}$, is the deterministic CL vortex force driving Langmuir circulations [11, 12]. These studies address the forward problem of how wind waves modify upper-ocean turbulence and currents,

not the inverse problem of swell decay. We cite them here solely to identify the mathematical structure of the CL vortex force. The second, $\boldsymbol{u}_s \times \boldsymbol{\omega}'$, is a slow stochastic contribution. The full phase-averaged force $\boldsymbol{u}_s \times \boldsymbol{\Omega}_s$ modifies the mean flow on time scales $\gg T$, but carries no power at the swell frequency ω and thus does not, by itself, damp the wave mode. (A separate, direction-dependent CL energy pathway $\propto \cos\Delta\theta$ exists in wind seas but is expected to be small in path mean for remote swell owing to sign cancellations, see Section S9.)

The identity (S.23) and the wave-slaved vorticity (S.20) have been independently verified by wave-resolving simulation [13], which solved the full Navier-Stokes equations without invoking CL averaging. In our notation, their mean-vorticity analysis confirms that the wave-induced torque $\nabla \times \langle \boldsymbol{u}_\phi \times \boldsymbol{\omega}_{\text{wave}} \rangle_\varphi$ agrees with the curl of the vortex force $\nabla \times (\boldsymbol{u}_s \times \boldsymbol{\Omega}_s)$ to correlation coefficients exceeding 0.99, and that $\boldsymbol{\omega}_{\text{wave}}$ is produced by tilting and stretching of the slow vorticity $\boldsymbol{\Omega}_s$ by wave motion, consistent with (S.20).

E. Identification of the stochastic vortex force

Substituting the three-layer decomposition (S.19) into the orbital vortex force (S.7) separates three physically distinct couplings. Interaction with the ensemble-mean vorticity $\bar{\boldsymbol{\Omega}}$, with the wave-slaved vorticity $\boldsymbol{\omega}_{\text{wave}}$, and with the autonomous turbulent fluctuation $\boldsymbol{\omega}'$. The turbulent fluctuation $\boldsymbol{\omega}'$ participates in two of these. First, wave orbital motion acting on $\boldsymbol{\omega}'$ generates a component of the wave-slaved vorticity $\boldsymbol{\omega}_{\text{wave}} = \nabla \times (\boldsymbol{\xi} \times \boldsymbol{\Omega}_s)$ (Term II below). The resulting phase-averaged force is the zero-frequency CL contribution $\boldsymbol{u}_s \times \boldsymbol{\omega}'$, which does not project onto the wave mode. Second, $\boldsymbol{\omega}'$ couples directly to the oscillating orbital velocity through $\boldsymbol{u}_\phi \times \boldsymbol{\omega}'$ (Term III below). This force has zero phase mean but nonzero autocorrelation, and constitutes the microscopic coupling analysed in Sections S2-S5. The three-term split is,

$$\boldsymbol{f}_v = \boldsymbol{u}_\phi \times \boldsymbol{\omega} = \underbrace{\boldsymbol{u}_\phi \times \bar{\boldsymbol{\Omega}}}_{\text{Term I}} + \underbrace{\boldsymbol{u}_\phi \times \boldsymbol{\omega}_{\text{wave}}}_{\text{Term II}} + \underbrace{\boldsymbol{u}_\phi \times \boldsymbol{\omega}'}_{\text{Term III}}. \tag{S.24}$$

We evaluate the phase average of each term in turn. For Term I, $\bar{\boldsymbol{\Omega}}$ is slowly varying. By (S.14) and (S.12),

$$\langle \boldsymbol{u}_\phi \times \bar{\boldsymbol{\Omega}} \rangle_\varphi = \boldsymbol{0}. \tag{S.25}$$

For Term II, the McWilliams identity (S.23) gives

$$\langle \boldsymbol{u}_\phi \times \boldsymbol{\omega}_{\text{wave}} \rangle_\varphi \equiv_\nabla \boldsymbol{u}_s \times \boldsymbol{\Omega}_s = \boldsymbol{u}_s \times \bar{\boldsymbol{\Omega}} + \boldsymbol{u}_s \times \boldsymbol{\omega}'. \tag{S.26}$$

For Term III, $\boldsymbol{\omega}'$ is slowly varying on the wave timescale ($\tau_{\text{eddy}} \gg T$). By the slow-field extraction rule,

$$\langle \boldsymbol{u}_\phi \times \boldsymbol{\omega}' \rangle_\varphi = \langle \boldsymbol{u}_\phi \rangle_\varphi \times \boldsymbol{\omega}' + O(T/\tau_{\text{eddy}}) = \boldsymbol{0} \times \boldsymbol{\omega}' + O(T/\tau_{\text{eddy}}) = O(T/\tau_{\text{eddy}}), \tag{S.27}$$

so its phase average vanishes to leading order. This vanishing is a *kinematic* consequence of the slow-field extraction rule and $\langle \boldsymbol{u}_\phi \rangle_\varphi = \boldsymbol{0}$ and it holds regardless of how $\boldsymbol{\omega}'$ was generated. The deeper requirement is that $\boldsymbol{\omega}'$ should be *statistically independent* of the wave phase, not merely slow. This requirement enters only at the ensemble level in the Green-Kubo analysis of Section S2 (Assumption A3(ii)). Collecting the three results,

$$\langle \boldsymbol{f}_v \rangle_\varphi \equiv_\nabla \boldsymbol{u}_s \times \boldsymbol{\Omega}_s, \tag{S.28}$$

recovering the classical CL result. On time scales long compared with the wave period, the net effect of the orbital motion on the slow flow is the CL vortex force.

All three terms in (S.24) have zero or slow phase averages, so the question of irreversibility cannot be resolved at the level of first-order (mean-force) diagnostics. Whether swell is damped or not depends on the cumulative work done by the *fluctuating* part of the force as the wave packet propagates through the turbulent field. We therefore examine each term's capacity for net energy transfer on the wave timescale.

Mean-vorticity term ($\boldsymbol{u}_\phi \times \bar{\boldsymbol{\Omega}}$). $\bar{\boldsymbol{\Omega}}$ has no accessible internal degrees of freedom. Its coupling to the orbital motion therefore produces a phase-locked, reversible response. At the leading order, it renormalises the wave frequency, but does not contribute to the dissipative Green-Kubo real part that defines the mode-level damping rate.

Wave-slaved term ($\boldsymbol{u}_\phi \times \boldsymbol{\omega}_{\rm wave}$). The wave-slaved vorticity $\boldsymbol{\omega}_{\rm wave} = \nabla \times (\boldsymbol{\xi} \times \boldsymbol{\Omega}_s)$ carries no independent degrees of freedom at leading order. The retained wave-slaved contribution is fully determined by the instantaneous wave kinematics and the frozen slow field, leaving no autonomous bath-like dynamics that could generate irreversible redistribution of energy. Because both $\boldsymbol{u}_\phi$ and $\boldsymbol{\omega}_{\rm wave}$ oscillate at the wave frequency ω, their product has spectral support at leading order only at frequencies 0 and 2ω. (For a narrowband wave packet with slowly modulated envelope, the spectral leakage away from 0 and 2ω is higher order and does not generate a secular component at ω to leading order.) The slow (0-frequency) component is precisely the CL force $\boldsymbol{u}_s \times \boldsymbol{\Omega}_s$, which modifies the mean-flow evolution on timescales $\gg T$ but carries no spectral weight at the swell frequency ω and therefore cannot contribute to the Green-Kubo damping rate of that wave mode. The 2ω component likewise has no projection onto the swell mode. Term II therefore cannot contribute to the mode-level damping rate.

Turbulent-fluctuation term ($\boldsymbol{u}_\phi \times \boldsymbol{\omega}'$). By contrast, $\boldsymbol{\omega}'$ possesses internal degrees of freedom that prevent exact reversal (as discussed in Section D and quantified in Section S6). Furthermore, as the swell propagates at $c_g \sim$ 10-15 m s^{-1}, it successively encounters statistically independent turbulent regions, providing a finite decorrelation length along the ray. Within this decomposition, Term III is the only component that possesses both ingredients for irreversible energy transfer. It has internal degrees of freedom, preventing exact reversal over a cycle, and spatial decorrelation, preventing coherent cancellation over many cycles. The two ingredients play distinct roles. Spatial decorrelation controls the *magnitude* of the damping rate by setting the Green-Kubo convergence time. The internal evolution of $\boldsymbol{\omega}'$ guarantees its *sign* (Section I). Within the present bulk, non-breaking, potential-wave framework, Term III is the unique candidate for irreversible swell attenuation. We define the *stochastic vortex force* (SVF),

$$\boxed{\boldsymbol{f}_{\rm svf} \;\equiv\; \boldsymbol{u}_\phi \times \boldsymbol{\omega}'.} \tag{S.29}$$

The statistical-mechanical framework of Section S2 formalises this picture. Projecting the full dynamics onto the swell subspace via the Mori-Zwanzig formalism identifies the orthogonal (noise) force that drives the memory kernel. Under the scale-separation and statistical-decoupling assumptions A2-A4, this projected force reduces precisely to the SVF,

$$F_{\boldsymbol{k}}(t) = \big[Q(\boldsymbol{u}_\phi \times \boldsymbol{\omega})\big]_{\boldsymbol{k}} \;\longrightarrow\; \big[\boldsymbol{u}_\phi \times \boldsymbol{\omega}'\big]_{\boldsymbol{k}}, \tag{S.30}$$

where $Q = 1 - P$ is the orthogonal projector in the Hilbert space of observables and the arrow denotes the identification that holds under Assumptions A2-A4 (not an algebraic identity). The discarded contributions are absorbed into the streaming term and into gradient/solenoidal forces whose net work on the swell mode vanishes.

A deliberate choice underlies the derivation. We keep a phase-resolved *Eulerian* description rather than working directly in the Generalised Lagrangian Mean (GLM) framework of classical Craik-Leibovich theory. GLM absorbs wave effects into Lagrangian-mean quantities and yields the phase-averaged CL vortex force ($\boldsymbol{u}_s \times \boldsymbol{\Omega}_s$), while practical mean-flow applications often focus on its ensemble-mean component ($\boldsymbol{u}_s \times \bar{\boldsymbol{\Omega}}$). Here our target is different. The irreversible attenuation arises from the *fluctuating* coupling $\boldsymbol{f}_{\rm svf} = \boldsymbol{u}_\phi \times \boldsymbol{\omega}'$. This term has zero phase mean and is therefore absent from the mean CL force, yet its *two-time* autocorrelation determines the friction coefficient via the Green-Kubo formula. Retaining the wave-slaved response $\boldsymbol{\omega}_{\rm wave}$ and the instantaneous force $\boldsymbol{f}_{\rm svf}$ makes the subsequent statistical closure and the link to observations explicit.

S2. Non-negativity of the Green-Kubo damping coefficient

This section proves that $\Gamma(\boldsymbol{k}) \geq 0$ for any surface gravity wave propagating through turbulence, using the Green-Kubo relation [14, 15]

$$\Gamma(\boldsymbol{k}) = \frac{1}{2E_{\boldsymbol{k}}} \int_0^\infty \mathrm{Re}\big\langle F_{\boldsymbol{k}}(0)\, F^*_{\boldsymbol{k}}(\tau)\big\rangle \,\mathrm{d}\tau, \tag{S.31}$$

where $F_{\boldsymbol{k}}$ is the mode-projected stochastic vortex force identified in Section S1 and connected to the Mori-Zwanzig formalism below. The inequality follows from Bochner's theorem [16] and holds regardless of the bath spectrum $E_\omega(q)$. The quantitative evaluation is carried out in Sections S3-S5. We retain the notation of Section S1: $\langle\cdot\rangle_\varphi$ for the wave-phase average, $\langle\cdot\rangle$ for the ensemble average over the stationary bath measure $\rho_{\rm ss}$.

A. Assumptions A1-A6

To connect the microscopic SVF to a coarse-grained damping rate we make six assumptions. We first state them in compact form. The subsequent discussion gives physical motivation and typical values (verified a posteriori).

A1 (Resolved wave band). There exists a narrow band $\mathcal{B}$ of swell wavenumbers such that each $\boldsymbol{k} \in \mathcal{B}$ admits a linear dispersion relation $\omega(\boldsymbol{k})$ and a complex amplitude $a_{\boldsymbol{k}}(t)$, with modal energy

$$E_{\boldsymbol{k}}(t) \equiv \tfrac{1}{2}|a_{\boldsymbol{k}}(t)|^2. \tag{S.32}$$

Ensemble averages $\langle\cdot\rangle$ act on the bath degrees of freedom $\boldsymbol{\omega}'$ at fixed $\{a_{\boldsymbol{k}}\}$. When needed, a further average over wave realisations is denoted explicitly. Nonlinear wave-wave interactions are negligible on the attenuation time scale Γ^{-1} for far-field swell [17].

A2 (Time-scale separation). The force autocorrelation decays on a correlation time $\tau_{\rm c}$ much shorter than the attenuation time,

$$\tau_{\rm c} \ll \Gamma(\boldsymbol{k})^{-1} \quad \text{for all } \boldsymbol{k} \in \mathcal{B}. \tag{S.33}$$

A3 (Bath statistics and phase decoupling). Three sub-conditions on the autonomous turbulent vorticity $\boldsymbol{\omega}'$:

- **(i)** *Local stationarity and homogeneity.* The statistics of $\boldsymbol{\omega}'$ are stationary and translation-invariant within analysis patches of size $O(k^{-1})$. The slow along-ray variation of the bath parameters is treated by a local closure (Section S5 E).
- **(ii)** *Phase decoupling.* The statistics of $\boldsymbol{\omega}'$ are independent of the swell phase.
- **(iii)** *Zero ensemble mean.* $\langle\boldsymbol{\omega}'\rangle_{\rho_{\rm bath}} = \boldsymbol{0}$.

A4 (Linear truncation in wave amplitude). The SVF enters the amplitude equation at first order in $\{a_{\boldsymbol{k}}\}$. Feedback terms of order $|a_{\boldsymbol{k}}|^2$ can be neglected.

A5 (Locally stationary reference measure). Two sub-conditions:

- **(i)** *Local stationarity.* For each fixed value of the resolved wave amplitudes $\{a_{\boldsymbol{k}}\}$ (treated as quasi-constant over $\tau \lesssim \tau_{\rm c}$), the mixed-layer turbulence admits a locally stationary reference measure $\rho_{\rm bath}(\boldsymbol{\omega}')$ over the support of the memory kernel.
- **(ii)** *Factorisation.* The full reference measure factorises approximately into independent wave and bath parts:

$$\rho_{\rm ss}(\{a_{\boldsymbol{k}}\}, \boldsymbol{\omega}') \approx \rho_{\rm wave}(\{a_{\boldsymbol{k}}\})\, \rho_{\rm bath}(\boldsymbol{\omega}'). \tag{S.34}$$

No equilibrium-specific properties (Boltzmann form, detailed balance, equipartition) are imposed. The NESS structure is discussed in Section B. No global stationary measure for the coupled wave-turbulence system is assumed. The wave amplitude is quasi-frozen over $\tau \lesssim \tau_{\rm c}$ ($\Gamma\tau_{\rm c} \sim 10^{-6}$-$10^{-4}$), making $C_F(\tau)$ and the Mori-Zwanzig inner product well-defined to leading order in δ.

A6 (Finite memory). The mode-projected SVF has an absolutely integrable autocorrelation, so that the Green-Kubo integral converges.

The physical origin of τ_c in A2 is advective phase decorrelation along the wave-energy trajectory. For a $T = 15$ s swell ($k \approx 0.018\ \mathrm{m}^{-1}$, $c_g \approx 11.7\ \mathrm{m\,s}^{-1}$), the dominant coupling is with eddies of scale $\ell \sim k^{-1} \approx 56$ m (Section S3 F). As the wave-energy trajectory advances at c_g, the mode-projected force from a turbulent mode at wavenumber q acquires an advected phase $\exp(\mathrm{i}\boldsymbol{q} \cdot \boldsymbol{c}_g\, t)$. At the dominant scale $q \sim k$ this phase reaches $O(1)$ in $\tau_{\mathrm{adv}} \sim 1/(k\, c_g) \approx 4.8$ s, after which successive eddy-scale patches contribute to the Green-Kubo integral with randomised phases. The decorrelation is spatial in origin. The wave-energy trajectory advances through a spatially incoherent turbulent field, not a temporally evolving one. Irreversibility requires the eddy's internal degrees of freedom to evolve during the encounter ($\delta = \tau_c/\tau_{\mathrm{eddy}} > 0$, Section I). Over the attenuation time $\Gamma^{-1} \sim 10^5$-10^6 s, the packet encounters $\Gamma^{-1}/\tau_c \sim 10^5$ eddies in sequence along its ray. A2 is not needed for the inequality $\Gamma \geq 0$, which follows from Bochner's theorem alone. It enters when interpreting Γ as the rate of exponential decay in the Markovian limit.

Assumption A3 draws on the three-layer decomposition of Sec. S1: $\boldsymbol{\omega} = \bar{\boldsymbol{\Omega}} + \boldsymbol{\omega}' + \boldsymbol{\omega}_{\mathrm{wave}}$, with $\boldsymbol{\Omega}_s = \bar{\boldsymbol{\Omega}} + \boldsymbol{\omega}'$ the phase-averaged (slow) vorticity. Sub-condition A3(i) requires that the vorticity statistics be translation-invariant within each analysis patch of size $O(k^{-1})$. With this local homogeneity the SVF correlation takes the form

$$\left\langle \boldsymbol{f}_{\mathrm{svf}}(\boldsymbol{x}, t) \otimes \boldsymbol{f}_{\mathrm{svf}}(\boldsymbol{x}', t') \right\rangle = \boldsymbol{C}_f\big(\boldsymbol{x} - \boldsymbol{x}',\, t - t'\big). \tag{S.35}$$

Sub-condition A3(ii), the phase decoupling, follows from the remote origin of swell (as discussed in Sec. S1). Even when swell-driven Stokes drift modifies the local turbulence-for instance by driving Langmuir circulation, this modification depends only on the phase-averaged Stokes drift $\boldsymbol{u}_s \propto |a_k|^2 \omega k\, e^{2kz}$, a second-order quantity that carries no information about the instantaneous wave phase. The turbulence statistics may therefore depend on the swell *amplitude* (a higher-order effect addressed under A4) but remain independent of the swell *phase*, which is set by conditions thousands of kilometres away. The observed amplitude-independence of attenuation rates [18, 19] provides empirical confirmation of this decoupling. Sub-condition A3(iii), the zero ensemble mean, holds by definition of the Reynolds decomposition $\boldsymbol{\omega}' = \boldsymbol{\Omega}_s - \bar{\boldsymbol{\Omega}}$ (Section S1, Eq. S.18). The SVF $\boldsymbol{f}_{\mathrm{svf}} = \boldsymbol{u}_\phi \times \boldsymbol{\omega}'$ vanishes under both the phase average (because $\langle \boldsymbol{u}_\phi \rangle_\varphi = \boldsymbol{0}$) and the ensemble average (because $\langle \boldsymbol{\omega}' \rangle = \boldsymbol{0}$), as required for a fluctuating force in the Mori-Zwanzig sense.

The coupling parameter in A4 is $\delta \equiv u'/c_g$ (formally defined in Eq. S.71 below), where u' is a typical turbulent velocity at the eddy scale $\ell \sim k^{-1}$ that couples most strongly to the swell (Sec. S3) and c_g is the group velocity. For far-field swell, $\delta \sim 10^{-3}$-10^{-2}. Two estimates confirm the validity of the linear truncation. First, per-encounter is linearity. Over one correlation time $\tau_c \sim 5$ s the fractional amplitude change is $\Gamma\tau_c \sim 10^{-6}\ \mathrm{s}^{-1} \times 5\ \mathrm{s} \sim 5 \times 10^{-6}$ (the value $\Gamma \sim 10^{-6}\ \mathrm{s}^{-1}$ follows from the closed-form evaluation in Sections S3-S5), well inside the linear-response regime. Nonlinear corrections enter at $O(\delta^2) \sim 10^{-6}$-10^{-4}. Second, it is under the weak-probe condition. The total power extracted from the swell, $\dot{W} \sim 2\Gamma E_{\mathrm{w}} \sim 5 \times 10^{-3}\ \mathrm{W\,m}^{-2}$ for typical far-field amplitudes ($H_s \sim 2$ m), is two orders of magnitude below the ~ 0.1-$1\ \mathrm{W\,m}^{-2}$ supplied to the mixed-layer turbulent bath by wind-wave breaking, current shear and Langmuir circulations [20–22]. Since $\dot{W} \propto H_s^2$, the weak-probe condition is comfortably satisfied for the far-field swell regime $H_s \lesssim 5$ m considered throughout this work. Near-storm conditions ($H_s \gtrsim 10$ m) violate A4 together with A1 and A3(ii).

Assumption A5 posits the existence of at least one stationary measure $\rho_{\mathrm{ss}}(\{a_{\boldsymbol{k}}\}, \boldsymbol{\omega}')$ for the wind-driven mixed layer, maintained in a statistically steady state by the balance of forcing and dissipation. Correlation functions under ρ_{ss} are time-translation invariant on the support of the memory kernel ($\sim \tau_c$). The measure factorises to good approximation as in Eq. (S.34), reflecting the negligible back-reaction of remote-source swell on local turbulence. The mode-projected stochastic force in A6,

$$F_{\boldsymbol{k}}(t) = \int \mathrm{d}^3\boldsymbol{x}\ \boldsymbol{\psi}^*_{\boldsymbol{k}}(\boldsymbol{x}) \cdot \boldsymbol{f}_{\mathrm{svf}}(\boldsymbol{x}, t), \tag{S.36}$$

is defined by expanding the wave velocity field onto the linear deep-water eigenfunctions, $\boldsymbol{u}_\phi(\boldsymbol{x}, t) = \sum_{\boldsymbol{k} \in \mathcal{B}} a_{\boldsymbol{k}}(t)\, \boldsymbol{\psi}_{\boldsymbol{k}}(\boldsymbol{x}) + \mathrm{c.c.}$, with normalisation chosen such that $E_{\boldsymbol{k}} = \frac{1}{2}|a_{\boldsymbol{k}}|^2$. For deep-water surface gravity

waves the linearised operator is self-adjoint under the energy inner product, so $\boldsymbol{\psi}_{\boldsymbol{k}}$ serves simultaneously as the eigenfunction and its adjoint. The projection (S.36) is therefore unambiguous. The memory kernel is diagonal in wavevector as a consequence of the translational invariance of the bath statistics (A3(i)) and the Fourier structure of the mode functions. Cross-correlations $\langle F_{\boldsymbol{k}} F^*_{\boldsymbol{k}'}\rangle$ vanish for $\boldsymbol{k} \neq \boldsymbol{k}'$. The mode-projected force has an absolutely integrable autocorrelation

$$\int_0^\infty \left|\langle F_{\boldsymbol{k}}(0)\, F_{\boldsymbol{k}}(\tau)^*\rangle\right| \mathrm{d}\tau < \infty. \tag{S.37}$$

By stationarity, $C_F(-\tau) = C_F(\tau)^*$, so half-axis integrability implies $C_F \in L^1(\mathbb{R})$ and the Fourier transform $S_F(\omega)$ is well defined. The physical mechanism ensuring rapid convergence is the same advective phase decorrelation discussed under A2. Sweeping at $c_g \gg u'$ suppresses long-time tails (cf. the $t^{-3/2}$ Alder-Wainwright tails of molecular fluids [23]), placing the system deep in the Markovian regime. Assumptions A1, A3(i), A5(i) and A6 are the structural inputs to the non-negativity theorem. A2, A3(ii) and A4 enter later, when we pass from the generalised Langevin equation to a Markovian damping rate and to pathwise statistics. A5(ii) enters in the cancellation of probe energy from Γ (Section C.4). None of these assumptions refers to the specific form of the bath spectrum $E_\omega(q)$. The non-negativity theorem is therefore independent of whether the turbulence is in the inertial range, the viscous range, or a transitional regime.

Remark 2 (Swell-driven Langmuir feedback and the weak-probe condition) *The weak-probe estimates in A4 show that far-field swell extracts at most a few percent of the bath TKE input. A subtler back-reaction channel is the modification of ε through swell-Stokes-drift-driven Langmuir turbulence. In moderate winds, the swell band contributes $\lesssim O(10\%)$ of the total near-surface u_s [22, 24]. In light winds this fraction can be larger, and even when the surface fraction is small the swell Stokes drift penetrates to depths $\sim 1/(2k) \sim 30\,m$, well below the wind-wave contribution. The relevant question is not whether swell modifies ε, but whether that modification depends on swell* amplitude*-and thereby introduces a nonlinear feedback on Γ. Since the Stokes drift scales as $u_s \propto |a_k|^2$, any such feedback enters at $O(|a_k|^2)$ relative to the leading-order SVF coupling, consistent with the A4 truncation. The observed amplitude-independence of attenuation rates [18, 19] confirms that this feedback is negligible in the far-field regime.*

B. Non-equilibrium steady states and FDR-II

The Mori-Zwanzig projection starts from a stationary measure ρ_{ss}, defines an inner product

$$\langle A, B\rangle_\rho = \int A(\boldsymbol{X})\, B^*(\boldsymbol{X})\, \rho_{\mathrm{ss}}(\boldsymbol{X})\, \mathrm{d}\boldsymbol{X}, \tag{S.38}$$

and constructs the orthogonal projector $\mathcal{P}$ onto the chosen slow subspace. The derivation of the generalised Langevin equation and of the second fluctuation-dissipation relation uses only the algebra of $\mathcal{P}$ and $\mathcal{Q} = 1 - \mathcal{P}$ and the stationarity of ρ_{ss}, not its functional form or any symmetry of the Liouville operator [25, 26]. In particular, the second fluctuation-dissipation relation (FDR-II),

$$K_{\boldsymbol{k}}(\tau) = \frac{\langle F_{\boldsymbol{k}}(0)\, F_{\boldsymbol{k}}(\tau)^*\rangle}{\langle |a_{\boldsymbol{k}}|^2\rangle_{\mathrm{ref}}}, \tag{S.39}$$

holds for any stationary measure, whether equilibrium or driven-dissipative. It follows from the algebra of the Mori-Zwanzig projectors alone. The construction uses only two properties. First, the self-adjointness of $\mathcal{P}$ under $\langle\cdot,\cdot\rangle_\rho$ ($\langle \mathcal{P}A, B\rangle_\rho = \langle A, \mathcal{P}B\rangle_\rho$), which holds by construction as an orthogonal projection. Second, the time-translation invariance of correlation functions under ρ_{ss}, which requires only $\mathcal{L}$-invariance of the measure, not detailed balance or self-adjointness of $\mathcal{L}$ [25, 26]. The local forcing-driven mixed layer is a mechanically forced NESS in the sense of Evans and Morriss [27]. Analogous Green-Kubo relations have been validated in mechanically driven fluids [27, 28] and active-matter systems [29, 30]. The stationarity required here is only local in time. ρ_{ss} must be time-translation invariant over the support of the memory kernel ($\sim \tau_c$), not over the full swell propagation time. Section D shows that this condition is satisfied with four orders of magnitude of margin ($\tau_c/\tau_{\mathrm{NESS}} \sim 10^{-4}$), even in the most conservative climate zone along the ray.

C. Operational construction of the reference measure

The Mori-Zwanzig formalism requires an inner product weighted by ρ_{ss}, but not its explicit functional form. For swell, three properties are sufficient. Stationarity, factorisation into wave and bath sectors, and finite second moments of the bath vorticity.

C.1. Factorisation and orthogonality

Remote swell and local turbulence are forced by independent mechanisms. The factorisation (S.34) expresses the negligible back-reaction of remote-source swell on local turbulence. Under this factorisation, the orthogonality required by the projection formalism follows directly,

$$\langle F_{\boldsymbol{k}}\, a_{\boldsymbol{k}}^{*}\rangle = \Big\langle a_{\boldsymbol{k}}^{*} \underbrace{\langle F_{\boldsymbol{k}}\rangle_{\rho_{\mathrm{bath}}}}_{=0}\Big\rangle_{\rho_{\mathrm{wave}}} = 0, \tag{S.40}$$

since $F_{\boldsymbol{k}}$ is linear in $\boldsymbol{\omega}'$ and $\langle\boldsymbol{\omega}'\rangle_{\rho_{\mathrm{bath}}} = \mathbf{0}$ (A3(iii)). Orthogonality thus reflects the physical decoupling between swell and bath, rather than an additional postulate.

C.2. Bath sector: second-order vorticity statistics

The Green-Kubo numerator involves the force autocorrelation

$$C_F(\tau) = \left\langle \int \mathrm{d}^3\boldsymbol{x}\, \boldsymbol{\psi}_{\boldsymbol{k}}^{*}\cdot\left(\boldsymbol{u}_\phi\times\boldsymbol{\omega}'\right)(\boldsymbol{x},0) \int \mathrm{d}^3\boldsymbol{x}'\, \boldsymbol{\psi}_{\boldsymbol{k}}\cdot\left(\boldsymbol{u}_\phi\times\boldsymbol{\omega}'\right)^{*}(\boldsymbol{x}',\tau)\right\rangle. \tag{S.41}$$

Given the wave field $\boldsymbol{u}_\phi$, this depends on ρ_{bath}, only through the second-order vorticity statistics. For locally isotropic turbulence-an assumption justified within the ocean mixed layer in Section S5 G and implicit throughout the spectral evaluation of Sections S3-S5. The vorticity covariance takes the solenoidal form

$$\langle\omega_i'(\boldsymbol{q})\,\omega_j'^{*}(\boldsymbol{q}')\rangle_{\rho_{\mathrm{bath}}} = \frac{E_\omega(q)}{4\pi}\left(\delta_{ij}-\hat{q}_i\hat{q}_j\right)\delta(\boldsymbol{q}-\boldsymbol{q}'), \tag{S.42}$$

where $E_\omega(q) = q^2E_u(q)$ is the enstrophy spectrum and $E_u(q) = 4\pi q^2 S_u(q)$ the isotropic one-dimensional velocity spectrum, normalised so that $\int_0^\infty E_u(q)\,\mathrm{d}q = \frac{1}{2}\langle|\boldsymbol{u}'|^2\rangle$. The prediction chain therefore closes as

$$E_\omega(q) \;\longrightarrow\; C_F(\tau;\boldsymbol{k}) \;\longrightarrow\; S_F(0;\boldsymbol{k}) \;\longrightarrow\; \Gamma(\boldsymbol{k}), \tag{S.43}$$

once $E_\omega(q)$ is specified. No higher-order vorticity statistics are needed. The full complexity of the turbulent bath is filtered through a single spectral function. Unlike the pair correlation function $g(r)$ required in the analogous Green-Kubo integral for simple-liquid viscosity [31], the turbulent vorticity spectrum $E_\omega(q)$ in the inertial range is fixed by the Kolmogorov cascade [32] to $E_\omega(q)\propto\varepsilon^{2/3}q^{1/3}$. No closure beyond the Kolmogorov inertial-range spectrum is needed (Sec. S4).

C.3. What we need from ρ_{wave}. Externally prescribed modal energy

The denominator of FDR-II (S.39) is the reference modal energy $\langle|a_{\boldsymbol{k}}|^2\rangle_{\mathrm{ref}} = 2E_{\boldsymbol{k}}$, prescribed by the remote storm, not by the local bath. Probe and bath are parameterised by independent energy scales-$E_{\boldsymbol{k}}$ and ε-so $E_{\boldsymbol{k}}$ cancels exactly from Γ (Section C.4).

C.4. Independence of the damping rate from probe energy

Although both numerator and denominator of (S.31) depend on $E_{\boldsymbol{k}}$, the dependence cancels exactly when linear coupling and statistical decoupling both hold. The stochastic vortex force is bilinear: $\boldsymbol{f}_{\mathrm{svf}} = \boldsymbol{u}_\phi\times\boldsymbol{\omega}'$, with $\boldsymbol{u}_\phi\propto a_{\boldsymbol{k}}$. Under the linear truncation (A4), the mode-projected force inherits this linearity, $F_{\boldsymbol{k}}\propto a_{\boldsymbol{k}}$. Over the short correlation window $\tau\lesssim\tau_{\mathrm{c}}$, the amplitude varies negligibly (A2 and Eq. (S.49)), so that $a_{\boldsymbol{k}}(0)a_{\boldsymbol{k}}^{*}(\tau)\approx|a_{\boldsymbol{k}}|^2$ within the Green-Kubo integral. Factorisation A5(ii) then permits the numerator to be decomposed as

$$\left\langle F_{\boldsymbol{k}}(0)\,F_{\boldsymbol{k}}^{*}(\tau)\right\rangle = \left\langle|a_{\boldsymbol{k}}|^2\right\rangle \times \mathcal{G}_{\boldsymbol{k}}(\tau), \tag{S.44}$$

where $\mathcal{G}_{\boldsymbol{k}}(\tau)$ depends only on the bath vorticity statistics and the mode geometry (wave polarisation $\boldsymbol{\psi}_{\boldsymbol{k}}$ and wavenumber k), but not on $E_{\boldsymbol{k}}$. Substituting (S.44) into (S.31) and noting $\langle |a_{\boldsymbol{k}}|^2 \rangle = 2E_{\boldsymbol{k}}$ gives

$$\Gamma(\boldsymbol{k}) = \frac{1}{2E_{\boldsymbol{k}}} \int_0^\infty \mathrm{Re}\big[\langle |a_{\boldsymbol{k}}|^2 \rangle \, \mathcal{G}_{\boldsymbol{k}}(\tau)\big] \, \mathrm{d}\tau = \int_0^\infty \mathrm{Re}\big[\mathcal{G}_{\boldsymbol{k}}(\tau)\big] \, \mathrm{d}\tau. \tag{S.45}$$

We define

$$K_{\boldsymbol{k}}(\tau) \equiv \frac{\langle F_{\boldsymbol{k}}(0)\, F_{\boldsymbol{k}}(\tau)^* \rangle}{2E_{\boldsymbol{k}}} = \mathcal{G}_{\boldsymbol{k}}(\tau), \qquad \Gamma(\boldsymbol{k}) = \int_0^\infty \mathrm{Re}\big[K_{\boldsymbol{k}}(\tau)\big] \, \mathrm{d}\tau, \tag{S.46}$$

independent of the wave energy. Both assumptions are essential. If the SVF entered at second order ($F_{\boldsymbol{k}} \propto |a_{\boldsymbol{k}}|^2$), the numerator would scale as $E_{\boldsymbol{k}}^2$, making the memory kernel $K_{\boldsymbol{k}} \propto E_{\boldsymbol{k}}$ and the damping rate probe-dependent, like the nonlinear-microrheology regime. Likewise, if the bath statistics depended on the surface wave energy, $\mathcal{G}_{\boldsymbol{k}}$ would carry an implicit $E_{\boldsymbol{k}}$-dependence and the cancellation would be incomplete. For trans-oceanic swell, both conditions hold with large margins (Remark 2).

D. Time-scale separation and local validity

The Green-Kubo formula (defined formally in Section F below, Eq. S.58) is derived under a stationary reference measure, yet the swell amplitude decays along the ray at rate Γ. As noted in A5, no joint global steady state of $(\{a_{\boldsymbol{k}}\}, \omega')$ exists. The resolution rests on a three-level time-scale hierarchy and on a local application of the Green-Kubo relation. The force autocorrelation $C_F(\tau)$ is supported on $\tau_c \sim 5\,\mathrm{s}$ (A2). For the Green-Kubo integral to be evaluated under a locally stationary bath, the turbulent statistics, principally the dissipation rate ε, must remain approximately constant over each such window. The relevant time scale is the *persistence* time τ_{NESS}, i.e. the time over which the wind-driven mixed layer maintains its current statistical state at a fixed point on the ocean surface. A trans-oceanic swell ray typically spans 10 000-15 000 km and traverses several distinct climate zones, such as the mid-latitude storm belt where the swell is generated, the subtropical high-pressure belt, the trade-wind region, and possibly the opposite-hemisphere storm track. Among these, the shortest persistence arises in the mid-latitude storm tracks, where synoptic-scale weather systems have characteristic horizontal extent $L_{\mathrm{syn}} \sim 10^3\,\mathrm{km}$ and propagation speed $V_{\mathrm{syn}} \sim 10\,\mathrm{m\,s^{-1}}$ [33], giving

$$\tau_{\mathrm{NESS}} \;\sim\; \frac{L_{\mathrm{syn}}}{V_{\mathrm{syn}}} \;\sim\; \frac{10^6\,\mathrm{m}}{10\,\mathrm{m\,s^{-1}}} \;\sim\; 10^5\,\mathrm{s} \;\sim\; 1\ \mathrm{day}. \tag{S.47}$$

In the trade-wind belt and subtropical highs, surface wind conditions persist on time scales of weeks or longer, so the mid-latitude estimate provides a *lower bound* on τ_{NESS} along the entire ray. Even this most conservative value yields

$$\frac{\tau_c}{\tau_{\mathrm{NESS}}} \;\sim\; 10^{-4}, \tag{S.48}$$

providing four orders of magnitude of margin. Over each short correlation window the bath may be treated as stationary, with an ε that is effectively constant on that window. The same hierarchy applied to the wave sector ensures that $E_{\boldsymbol{k}}$ is quasi-constant over each correlation window. The fractional energy change per window is

$$\tau_c\, \Gamma \;\lesssim\; 10^{-5} \qquad (\text{using } \Gamma \sim 10^{-6}\,\mathrm{s^{-1}} \text{ from Sections S3-S5}), \tag{S.49}$$

analogous to the Born-Oppenheimer separation of fast and slow degrees of freedom. Locally in time, we evaluate $\Gamma(\boldsymbol{k}; \varepsilon)$ from the instantaneous bath state and interpret it as the coefficient in a local equation

$$\frac{\mathrm{d}E_{\boldsymbol{k}}}{\mathrm{d}t} = -2\Gamma\big(\varepsilon(t), \boldsymbol{k}\big)\, E_{\boldsymbol{k}}(t), \tag{S.50}$$

which is the starting point for the path-averaged effective dissipation constructed in Section S5. On longer times ε varies along the ray, making $\Gamma = \Gamma(\varepsilon(t), \boldsymbol{k})$ slowly time-dependent. At each instant the local Green-Kubo construction applies, and the cumulative effect is obtained by integrating Eq. (S.50) (Section S5).

E. Projected dynamics and identification of the stochastic vortex force

We construct the projected dynamics and identify the microscopic force entering Eq. (S.31).

E.1. Generalised Langevin equation

In the Hilbert space $\mathcal{H} = L^2(\rho_{\rm ss})$ with inner product (S.38), where elements are phase-space observables $A(\boldsymbol{X})$, the orthogonal projection onto the swell subspace is

$$\mathcal{P}A = \sum_{\boldsymbol{k}\in\mathcal{B}} \frac{\langle A, a_{\boldsymbol{k}}\rangle_\rho}{\langle a_{\boldsymbol{k}}, a_{\boldsymbol{k}}\rangle_\rho}\, a_{\boldsymbol{k}}, \qquad \mathcal{Q} = 1 - \mathcal{P}. \tag{S.51}$$

By factorisation (A5(ii)), $\langle a_{\boldsymbol{k}}, a_{\boldsymbol{k}}\rangle_\rho = \langle |a_{\boldsymbol{k}}|^2\rangle = 2E_{\boldsymbol{k}}$. The microscopic amplitude equation can be written schematically as

$$\dot{a}_{\boldsymbol{k}}(t) = \mathrm{i}\sum_{\boldsymbol{k}'} \Omega_{\boldsymbol{k}\boldsymbol{k}'}\, a_{\boldsymbol{k}'}(t) + \mathcal{F}_{\boldsymbol{k}}(t), \tag{S.52}$$

where $\Omega_{\boldsymbol{k}\boldsymbol{k}'}$ is the linear frequency matrix (intrinsic dispersion plus Craik-Leibovich mean-flow corrections) and $\mathcal{F}_{\boldsymbol{k}}$ collects all remaining nonlinear coupling terms. The Mori-Zwanzig projection converts this into an exact generalised Langevin equation

$$\dot{a}_{\boldsymbol{k}}(t) = \mathrm{i}\sum_{\boldsymbol{k}'} \Omega_{\boldsymbol{k}\boldsymbol{k}'} a_{\boldsymbol{k}'}(t) - \int_0^t K_{\boldsymbol{k}}(t-s)\, a_{\boldsymbol{k}}(s)\,\mathrm{d}s + F_{\boldsymbol{k}}(t), \tag{S.53}$$

where $F_{\boldsymbol{k}}(t) = \mathrm{e}^{\mathrm{i}\mathcal{Q}\mathcal{L}t}\,\mathcal{Q}\mathcal{F}_{\boldsymbol{k}}(0)$ is the fluctuating force propagated entirely in the orthogonal subspace. The memory kernel is diagonal in wavevector, $K_{\boldsymbol{k}\boldsymbol{k}'}(\tau) = K_{\boldsymbol{k}}(\tau)\,\delta_{\boldsymbol{k}\boldsymbol{k}'}$, as a consequence of the spatial homogeneity assumed in A3, the $\rho_{\rm ss}$-weighted cross-correlations between distinct $\boldsymbol{k}$-modes vanish, so that the Mori-Zwanzig memory matrix reduces to a scalar kernel for each mode. By construction and the factorisation A5(ii), the fluctuating force satisfies

$$\mathcal{P}F_{\boldsymbol{k}}(t) = 0, \qquad \langle F_{\boldsymbol{k}}, a_{\boldsymbol{k}}\rangle_\rho = 0, \qquad \langle F_{\boldsymbol{k}}(t)\, a^*_{\boldsymbol{k}}(s)\rangle = 0 \quad (s \le t). \tag{S.54}$$

E.2. Stochastic vortex force as the microscopic coupling

In Section S1, the physical wave-vorticity coupling was decomposed into three pieces, $\boldsymbol{u}_\phi \times \bar{\boldsymbol{\Omega}}$ (coupling to the ensemble-mean vorticity), $\boldsymbol{u}_\phi \times \boldsymbol{\omega}_{\rm wave}$ (wave self-interaction via the wave-slaved vorticity), and $\boldsymbol{u}_\phi \times \boldsymbol{\omega}'$ (coupling to the turbulent vorticity fluctuation). The energy-budget analysis there showed that only the last term, the stochastic vortex force

$$\boldsymbol{f}_{\rm svf} = \boldsymbol{u}_\phi \times \boldsymbol{\omega}', \tag{S.55}$$

permits irreversible energy transfer from swell to turbulence. The mean-vorticity term is reactive and does not enter the dissipative Green-Kubo real part. The wave-slaved term carries spectral support only at zero and double frequency and therefore does not project onto the swell mode. The Mori-Zwanzig noise $F_{\boldsymbol{k}}(t)$, defined by the $\mathcal{Q}$-projector, satisfies three defining properties. Zero projection onto the wave subspace, zero correlation with the wave amplitudes, and propagation entirely within the orthogonal subspace (Eq. S.54). At the field level, the SVF $\boldsymbol{f}_{\rm svf}$ satisfies the same three properties under A1-A5. Zero ensemble mean (A3(iii)), zero correlation with $a_{\boldsymbol{k}}$ (A5(ii)), and autonomous temporal evolution governed by the turbulent cascade (A3(i)). Under the scale-separation and factorisation assumptions (A2-A5), the two selection procedures, Hilbert-space orthogonal projection and Navier-Stokes three-term decomposition, therefore isolate the same physical degrees of freedom.Fast fluctuations whose statistics are controlled by the bath, orthogonal to the resolved wave amplitudes. The abstract noise can accordingly be written as the mode projection of the physical field,

$$F_{\boldsymbol{k}}(t) = \int \mathrm{d}^3\boldsymbol{x}\; \boldsymbol{\psi}^*_{\boldsymbol{k}}(\boldsymbol{x}) \cdot \boldsymbol{f}_{\rm svf}(\boldsymbol{x}, t), \tag{S.56}$$

where $\boldsymbol{\psi}_{\boldsymbol{k}}(\boldsymbol{x})$ is the linear velocity eigenfunction of mode $\boldsymbol{k}$, with the normalisation convention $E_{\boldsymbol{k}} = \frac{1}{2}|a_{\boldsymbol{k}}|^2$ (Eq. S.32). Operationally, $\boldsymbol{\omega}'$ is obtained in a turbulence-resolving simulation by subtracting the wave-slaved vorticity $\boldsymbol{\omega}_{\mathrm{wave}} = \nabla \times (\boldsymbol{\xi} \times \boldsymbol{\Omega}_s)$ and the ensemble-mean $\bar{\boldsymbol{\Omega}}$ from the total vorticity. The SVF is then formed as $\boldsymbol{u}_{\phi} \times \boldsymbol{\omega}'$ and projected onto mode $\boldsymbol{k}$ via (S.56). This identification is a *physical equivalence under A2-A5*, not an algebraic identity. The $\boldsymbol{Q}$-projector acts in observable space while $\boldsymbol{f}_{\mathrm{svf}}$ is defined at the field level, but the assumptions guarantee that both yield the same force autocorrelation $C_F(\tau; \boldsymbol{k})$ and hence the same $\Gamma(\boldsymbol{k})$.

F. Green-Kubo relation and non-negativity of Γ

With $F_{\boldsymbol{k}}$ identified as the mode-projected SVF, FDR-II (S.39) can be written as

$$K_{\boldsymbol{k}}(\tau) = \frac{\langle F_{\boldsymbol{k}}(0)\, F_{\boldsymbol{k}}(\tau)^* \rangle}{2E_{\boldsymbol{k}}}. \tag{S.57}$$

The Green-Kubo damping coefficient is then

$$\Gamma(\boldsymbol{k}) \equiv \int_0^\infty \mathrm{Re}\big[K_{\boldsymbol{k}}(\tau)\big]\, \mathrm{d}\tau = \frac{1}{2E_{\boldsymbol{k}}} \int_0^\infty \mathrm{Re}\big[\langle F_{\boldsymbol{k}}(0)\, F_{\boldsymbol{k}}(\tau)^* \rangle\big]\, \mathrm{d}\tau. \tag{S.58}$$

The integral is convergent (A6). Stationarity here refers to the bath process conditional on quasi-frozen $a_{\boldsymbol{k}}$ over $\tau \lesssim \tau_{\mathrm{c}}$ (A5(i)), not to the globally evolving coupled system. Because $F_{\boldsymbol{k}}(t)$ is stationary with finite variance under this conditional measure, its autocorrelation is positive-definite in the sense of Bochner. To see this, let $\{t_j\}_{j=1}^n$ be any finite set of times and $\{\alpha_j\}$ arbitrary complex scalars. By the definition of C_F and the linearity of the expectation,

$$\sum_{j,\ell} \alpha_j \alpha_\ell^*\, C_F(t_j - t_\ell) = \sum_{j,\ell} \alpha_j \alpha_\ell^* \left\langle F_{\boldsymbol{k}}(t_j)\, F_{\boldsymbol{k}}(t_\ell)^* \right\rangle = \left\langle \left| \sum_j \alpha_j\, F_{\boldsymbol{k}}(t_j) \right|^2 \right\rangle \;\geq\; 0, \tag{S.59}$$

where $C_F(\tau) = \langle F_{\boldsymbol{k}}(0) F_{\boldsymbol{k}}(\tau)^* \rangle$. Bochner's theorem then implies that the power spectral density

$$S_F(\omega) = \int_{-\infty}^{\infty} C_F(\tau)\, \mathrm{e}^{\mathrm{i}\omega\tau}\, \mathrm{d}\tau \tag{S.60}$$

(we adopt the convention without 2π prefactors) is non-negative for all ω. By stationarity, $C_F(-\tau) = C_F(\tau)^*$, so $S_F(0)$ is real,

$$S_F(0)^* = \int_{-\infty}^{\infty} C_F(\tau)^*\, \mathrm{d}\tau = \int_{-\infty}^{\infty} C_F(-\tau)\, \mathrm{d}\tau = S_F(0). \tag{S.61}$$

The same symmetry allows the half-line integral in Eq. (S.58) to be extended to negative times: $\mathrm{Re}[C_F(-\tau)] = \mathrm{Re}[C_F(\tau)]$, hence $\int_0^\infty \mathrm{Re}[C_F(\tau)]\, \mathrm{d}\tau = \frac{1}{2} S_F(0)$, giving

$$\Gamma(\boldsymbol{k}) = \frac{S_F(0)}{4E_{\boldsymbol{k}}} \;\geq\; 0. \tag{S.62}$$

Because $C_F \in L^1(\mathbb{R})$ (A6, Section A), its Fourier transform $S_F(\omega)$ is a bounded continuous function, and thus $S_F(0)$ is finite. The autocorrelation of any second-order stationary process is positive-definite in the sense of (S.59). Since additionally $\langle F_{\boldsymbol{k}} \rangle = 0$ (A3(iii)), C_F is a centred autocorrelation. The non-negativity of $S_F(0)$, and hence of Γ, then follows from Bochner's theorem.

Theorem 1 (Non-negativity of Γ) *Under A1, A3*(i, iii)*, A5*(i) *and A6,*

$$\boxed{\Gamma(\boldsymbol{k}) \geq 0 \quad \textit{for all } \boldsymbol{k} \in \mathcal{B}.} \tag{S.63}$$

The stochastic vortex force cannot, on average, amplify swell. Individual propagation paths can exhibit apparent growth due to fluctuations (Section H), but the Markovian coarse-grained decay rate is non-negative. In the Markovian limit (A2), $\langle E_{\boldsymbol{k}}(t) \rangle$ decays monotonically for $t \gg \tau_{\mathrm{c}}$ (Section G, Eq. S.70).

The sign $\Gamma \geq 0$ is a purely kinematic property of stationary fluctuations. The Navier-Stokes content of the theory lies in identifying the correct microscopic force $F_{\boldsymbol{k}}$ and in evaluating its zero-frequency spectrum $S_F(0)$. The proof uses the following assumptions. A1 defines the wave amplitudes $a_{\boldsymbol{k}}$. A3(i) (stationarity and homogeneity of $\boldsymbol{\omega}'$) and A5(i) (local stationarity of the bath reference measure at fixed $a_{\boldsymbol{k}}$) guarantee that $C_F(\tau)$ is time-translation invariant. A3(iii) (zero ensemble mean under the bath measure) ensures $\langle F_{\boldsymbol{k}} \rangle = 0$, so that $C_F(\tau)$ is a centred autocorrelation. A6 ensures that $S_F(0)$ is finite. The non-negativity then follows from Bochner's theorem alone.

The following assumptions are *not* invoked in the sign proof. A2 (time-scale separation) enters only in the Markovian reduction (Section G). A3(ii) (phase decoupling) and A5(ii) (factorisation) enter only in the factorisation of ρ_{ss} and in the cancellation of $E_{\boldsymbol{k}}$ from the denominator (Section C.4). A4 (linear truncation) affects the amplitude dependence of Γ, but not its sign. The non-negativity theorem is both spectrum-agnostic (the form of $E_\omega(q)$ does not enter the proof) and wave-type-agnostic (it applies equally to wind waves and young seas). What changes across wave types is the value of Γ and whether the SVF damping can be isolated from competing processes (Section S9). The degeneracy $\Gamma(\boldsymbol{k}) = 0$ would require a fine-tuned cancellation $S_F(0) = 0$ between positive and negative lobes of $C_F(\tau)$. For a propagating wave packet that samples independent eddies, such cancellation is non-generic. The finite parameter $\delta = u'/c_g > 0$ ensures that each eddy evolves during the encounter time, breaking microscopic time-reversal symmetry and producing a strictly positive zero-frequency spectral density (Section I).

G. Markovian limit and monotonic energy decay

Under A2 the memory kernel $K_{\boldsymbol{k}}(\tau)$ decays on $\tau_{\mathrm{c}} \ll \Gamma^{-1}$. On times $t \gg \tau_{\mathrm{c}}$ the amplitude varies negligibly over the support of K, so

$$\int_0^t K_{\boldsymbol{k}}(\tau)\, a_{\boldsymbol{k}}(t-\tau)\, \mathrm{d}\tau \approx \Gamma(\boldsymbol{k})\, a_{\boldsymbol{k}}(t) + \mathrm{i}\,\Delta\omega_{\boldsymbol{k}}\, a_{\boldsymbol{k}}(t), \tag{S.64}$$

where we have split the integral into real and imaginary parts,

$$\Gamma(\boldsymbol{k}) = \int_0^\infty \mathrm{Re}\big[K_{\boldsymbol{k}}(\tau)\big]\, \mathrm{d}\tau, \qquad \Delta\omega_{\boldsymbol{k}} = \int_0^\infty \mathrm{Im}\big[K_{\boldsymbol{k}}(\tau)\big]\, \mathrm{d}\tau. \tag{S.65}$$

The frequency shift $\Delta\omega_{\boldsymbol{k}}$ can be absorbed into the dispersion relation. For swell, $|\Delta\omega|/\omega \sim \delta^2 \sim 10^{-6}$-$10^{-4}$, undetectable in practice. Substituting (S.64) into the GLE (S.53) yields

$$\dot{a}_{\boldsymbol{k}} = \mathrm{i}(\omega_{\boldsymbol{k}} + \Delta\omega_{\boldsymbol{k}})\, a_{\boldsymbol{k}} - \Gamma(\boldsymbol{k})\, a_{\boldsymbol{k}} + F_{\boldsymbol{k}}(t), \tag{S.66}$$

where for clarity we have suppressed the coupling to nearby $\boldsymbol{k}'$ in the intrinsic dispersion. Multiplying (S.66) by $a_{\boldsymbol{k}}^*$, adding the complex conjugate, and ensemble-averaging gives

$$\begin{aligned} \frac{\mathrm{d}}{\mathrm{d}t}\langle |a_{\boldsymbol{k}}|^2 \rangle &= 2\,\mathrm{Re}\Big\langle a_{\boldsymbol{k}}^* \dot{a}_{\boldsymbol{k}} \Big\rangle \\ &= 2\,\mathrm{Re}\Big[\mathrm{i}(\omega_{\boldsymbol{k}} + \Delta\omega_{\boldsymbol{k}})\langle |a_{\boldsymbol{k}}|^2 \rangle - \Gamma(\boldsymbol{k})\langle |a_{\boldsymbol{k}}|^2 \rangle + \langle a_{\boldsymbol{k}}^* F_{\boldsymbol{k}} \rangle\Big]. \end{aligned} \tag{S.67}$$

The first term is purely imaginary, so its real part vanishes. The third term vanishes by the orthogonality $\langle a_{\boldsymbol{k}}^* F_{\boldsymbol{k}} \rangle = 0$ (Eq. S.54). Using $\langle |a_{\boldsymbol{k}}|^2 \rangle = 2E_{\boldsymbol{k}}$ we obtain

$$\frac{\mathrm{d}}{\mathrm{d}t}\langle E_{\boldsymbol{k}}(t) \rangle = -2\Gamma(\boldsymbol{k})\, \langle E_{\boldsymbol{k}}(t) \rangle, \tag{S.68}$$

with solution

$$\langle E_{\boldsymbol{k}}(t) \rangle = E_{\boldsymbol{k}}(0)\, \mathrm{e}^{-2\Gamma(\boldsymbol{k})\, t}. \tag{S.69}$$

Since $\Gamma \geq 0$,

$$\frac{\mathrm{d}}{\mathrm{d}t}\langle E_{\boldsymbol{k}}(t) \rangle \leq 0 \quad \text{for all } t \gg \tau_{\mathrm{c}}. \tag{S.70}$$

The Markov approximation is controlled by the ratio τ_c/Γ^{-1}. With $\tau_c \sim \ell/c_g \sim 5$ s (Section A), the small parameter

$$\delta = \frac{u'}{c_g} \sim \left.\frac{\tau_c}{\tau_q}\right|_{q\sim k} \sim 10^{-3}\text{-}10^{-2} \tag{S.71}$$

simultaneously gives the turbulence-to-wave velocity ratio and, by the Kolmogorov relation $\varepsilon \sim u'^3/\ell$, the ratio of the advective decorrelation time to the eddy turnover time $\tau_q \sim (\varepsilon q^2)^{-1/3}\big|_{q\sim k}$. The finite but small value of δ has a dual role. It ensures that the Markov approximation is accurate, with $\tau_c/\Gamma^{-1} \sim 10^{-6}$-$10^{-4}$ under typical conditions and $\lesssim 10^{-4}$ even in extreme cases (the explicit dependence $\Gamma(\delta, \varepsilon, k)$ is derived in Sections S3-S5), and it provides the causal phase lag responsible for strict positivity $\Gamma > 0$ (Section I). Beyond the Markov limit, the GLE and FDR-II remain exact and define a frequency-dependent damping $\hat{\Gamma}(\omega) = \mathrm{Re}\int_0^\infty K_{\boldsymbol{k}}(\tau)\, e^{i\omega\tau} d\tau$. For trans-oceanic swell the extreme smallness of δ makes any departure from pure exponential decay negligible.

The non-negativity theorem holds for surface gravity waves propagating through turbulence. The closed-form scaling law requires additionally the weak-coupling and phase-decoupling conditions that characterise remote swell. A detailed analysis of the three dissipation channels and the domain of validity is given in Section S9.

H. Dual-line prediction structure

The Mori-Zwanzig projection fixes both the mean damping and the residual noise. For the band-integrated swell energy $E_w = \sum_{\boldsymbol{k}\in\mathcal{B}} E_{\boldsymbol{k}}$, the Markovian coarse-grained dynamics can be written as

$$\frac{dE_w}{dt} = -2\Gamma E_w + \tilde{\eta}(t), \tag{S.72}$$

where $\tilde{\eta}(t)$ is a zero-mean stochastic forcing inherited from $F_{\boldsymbol{k}}$. FDR-II constrains its autocorrelation. The noise diffusivity $D_E = 4\Gamma E_w^2$ is locked to the same Green-Kubo kernel that fixes the mean decay, so no additional parameter enters. Ensemble averaging removes $\tilde{\eta}$ and recovers Eq. (S.68). Converting to a spatial decay rate gives $\mu_E(\omega) = 2\Gamma/c_g$. Along a single satellite track, however, the integrated noise produces order-one relative fluctuations in the apparent rate $\hat{\mu}$. Because $\hat{\mu}$ is a log-energy regression slope while the dynamics are multiplicative, the pathwise estimator acquires an Itô correction, $\langle\hat{\mu}\rangle = 2\mu_E$. In the idealised near-independent-encounter limit (Section S6),

$$\mathrm{Var}(\hat{\mu}) = \frac{2\,\mu_E}{L}, \qquad c_0 \equiv \frac{\mathrm{Var}(\hat{\mu})}{\langle\hat{\mu}\rangle/L} = 1, \tag{S.73}$$

with L the path length, and the fraction of tracks with apparent negative attenuation is $P(\hat{\mu} < 0) = \Phi(-\sqrt{2\mu_E L})$, where Φ is the standard normal CDF. For trans-oceanic swell $\mathcal{S} = O(1)$, predicting a substantial minority of negative pathwise estimates-consistent with 13.3% (19) and ~24% (34). The full derivation, including the passage from the mode-sum to a scalar noise and the explicit evaluation of the constants 2, 2 and 1, is given in Section S6.

I. Physical origin of irreversibility: the single wave-eddy encounter

Bochner's theorem guarantees $\Gamma \geq 0$ whenever the force process is stationary (Section F). That $\Gamma > 0$ strictly requires a physical argument. The bath element must possess internal degrees of freedom that prevent the wave-eddy interaction from being elastic.

I.1. Encounter kinematics and modal energy exchange

The modal energy change during a single wave-eddy encounter of duration $\tau_{\mathrm{adv}} \sim \ell/c_g \sim 1/(q\, c_g)$ is

$$\Delta E_{\boldsymbol{k}} = \mathrm{Re}\int_0^{\tau_{\mathrm{adv}}} a_{\boldsymbol{k}}^*(t)\, F_{\boldsymbol{k}}(t)\, dt\,, \tag{S.74}$$

which can be positive or negative for any given encounter, depending on the instantaneous configuration of $\boldsymbol{\omega}'$.

I.2. Frozen-eddy limit and the physical origin of irreversibility

In the quasi-frozen limit where $\boldsymbol{\omega}'$ does not evolve during the encounter ($\tau_{\rm adv} \ll \tau_{\rm eddy}$ with $\delta \to 0$), a frozen but spatially inhomogeneous vorticity field can still exert a nonzero instantaneous force on the propagating wave packet. Along a given realisation, $F_{\boldsymbol{k}}(t)$ need not vanish, and the packet may undergo conservative redistribution of wave action among neighbouring wavevectors. That process is a within-wave-sector rearrangement, not the irreversible dissipation rate $\Gamma(\boldsymbol{k})$, defined by the Green-Kubo projection. The quantity $\Gamma(\boldsymbol{k})$ in Eq. (S.58) measures irreversible energy transfer from the wave field to the rotational bath, as enforced by the energy budget (Eq. S.9). In the strictly frozen-bath limit, the bath has no internal evolution during the encounter and therefore cannot absorb and retain net energy from the wave. Conservative mode-to-mode redistribution within the wave sector does not contribute to the positive-definite friction coefficient. Irreversibility requires the eddy to evolve during the encounter, providing the microscopic mechanism by which energy absorbed from the wave is redistributed among internal bath degrees of freedom before the wave phase returns. The characteristic evolution time of an inertial-range eddy is the Kolmogorov turnover time

$$\tau_{\rm eddy}(q) \;\sim\; (\varepsilon_{\rm eff}\, q^2)^{-1/3}\,, \tag{S.75}$$

which measures how long it takes for the eddy to lose memory of its initial configuration through the turbulent cascade. For far-field conditions with $\varepsilon_{\rm eff} \sim 5\times10^{-7}$ m^2 s^{-3} (Section S5 E, wall-law profile under $U_{10} \approx 10$ m s^{-1}) and $q \sim k \approx 0.02$ rad m^{-1}, $\tau_{\rm eddy} \sim 1.7\times10^3$ s (≈ 30 min). The ratio of the two time scales defines the key small parameter, recalling the key small parameter (Eq. S.71), $\delta \equiv \tau_{\rm adv}/\tau_{\rm eddy} \sim u'/c_g \sim 10^{-3}$-$10^{-2}$.

Here $u'(q) \sim (\varepsilon_{\rm eff}/q)^{1/3}$ is the Kolmogorov velocity at the swell-selected eddy scale. Since $\varepsilon_{\rm eff}$ varies along the swell ray with local forcing conditions (Section S5 E), the small parameter spans from $\delta \sim 2\times10^{-3}$ in light-wind regions ($\varepsilon_{\rm eff} \sim 5\times10^{-7}$) to $\delta \sim 10^{-2}$ in moderate-wind regions ($\varepsilon_{\rm eff} \sim 10^{-5}$).

I.3. Encounter-level energy statistics and the bias-to-fluctuation ratio

The modal energy change $\Delta E_{\boldsymbol{k}}$ fluctuates from encounter to encounter. To estimate its magnitude, we scale the mode-projected force $F_k \sim U_0\,|\boldsymbol{\omega}'| \sim U_0\,u'/\ell$ (orbital speed times vorticity at scale ℓ) and multiply by the amplitude times the advective decorrelation time $\tau_{\rm adv} \sim \ell/c_g$. The resulting fluctuation amplitude of the energy change per encounter is

$$\sigma_{\Delta E} \;\sim\; U_0\,\frac{u'^2}{\ell}\,\frac{\ell}{c_g} \;=\; \frac{U_0\,u'^2}{c_g}\,, \tag{S.76}$$

where $U_0 = a\omega$ is the surface orbital speed. In the quasi-frozen limit, $\langle\Delta E_{\boldsymbol{k}}\rangle = 0$ and the encounter is elastic. During the advective decorrelation time $\tau_{\rm adv}$, however, the eddy's vorticity evolves by a fraction $\Delta\omega'/\omega' \sim \tau_{\rm adv}/\tau_{\rm eddy} = \delta$: the configuration sampled at the end of the interval differs from that at the beginning by $O(\delta)$. This breaks the temporal symmetry of the force history, so the energy returned during the second half of the encounter falls short of that absorbed during the first half by a fraction δ, and the systematic (mean) energy change per encounter is

$$|\langle\Delta E_{\boldsymbol{k}}\rangle| \;\sim\; \delta\,\sigma_{\Delta E} \;\sim\; \frac{U_0\,u'^3}{c_g^2}\,. \tag{S.77}$$

Equivalently, in terms of fractional modal energy, the mean loss per encounter is $|\bar{\epsilon}| \sim E_k\,\delta^2$ and the standard deviation is $\sigma \sim E_k\,\delta$. The bias-to-fluctuation ratio per encounter is therefore

$$\boxed{\frac{|\langle\Delta E_{\boldsymbol{k}}\rangle|}{\sigma_{\Delta E}} \;\sim\; \delta \;=\; \frac{u'}{c_g} \;\sim\; 10^{-3}\text{-}10^{-2}\,,} \tag{S.78}$$

confirming that each wave-eddy encounter is nearly symmetric. The systematic loss is suppressed relative to the fluctuations by $\delta = \tau_{\rm adv}/\tau_{\rm eddy}$. Its sign is guaranteed by $S_F(\omega) \geq 0$ (Section F). The two distinct

roles of the time-scale hierarchy are worth emphasising: *advective decorrelation* ($c_g \gg u'$) controls the *magnitude* of dissipation by setting τ_{eff}, while the bath's *internal dynamics* (τ_{eddy} finite) guarantee its *sign* by providing the causal phase lag. Neither alone suffices. Advection without internal evolution gives an elastic encounter ($\langle \Delta E_{\boldsymbol{k}} \rangle = 0$). Internal evolution without advection gives an autocorrelation that does not decay along the ray, so the Green-Kubo integral does not converge.

The remote-swell problem falls within the generic Mori-Zwanzig regime identified by Chekroun et al. [35], in which memory corrections become subleading once the conditional-mean closure is accurate and the residual forcing decorrelates rapidly. Here phase averaging supplies the mean closure and the SVF supplies the fast residual. Unlike the data-adaptive closures in that framework, the noise autocorrelation closes analytically under inertial-range conditions.

S3. Evaluating the force autocorrelation in wavenumber space

Since we consider isotropic turbulence interacting with a unidirectional swell, we write $k = |\boldsymbol{k}|$ and suppress bold face on the swell wavevector throughout Sections S3 and S4. The turbulent wavevector $\boldsymbol{q}$ remains three-dimensional until angular integration is performed. Every turbulent eddy that overlaps with the wave orbital layer exerts a random force on the swell mode. The damping rate $\Gamma(k)$ is therefore a weighted integral over all turbulent scales, with the vorticity spectrum, the coupling geometry, and the decorrelation time along the ray setting the weight at each q.

Three facts convert the Green-Kubo time integral (S.58) into a time-free scaling law. First, advective sweeping at $c_g \gg u'$ dominates eddy turnover, so the effective correlation time is purely kinematic, $\tau_{\text{eff}}(q; k) = C_\tau/(q\, c_g)$. Second, the Kolmogorov spectrum fixes the force variance at each shell through the vorticity spectrum $E_\omega(q) = q^2 E_u(q) \propto \varepsilon^{2/3} q^{1/3}$, windowed by the scale-selection function $\mathcal{S}(q/k)$. Third, deep-water kinematics absorb the remaining scales. Amplitude dependence cancels by linearity of the SVF, and the dispersion relation $\omega^2 = gk$ converts $\Gamma(k) \propto \varepsilon^{2/3} k^{1/3}/c_g$ into $\mu_E(\omega) = C_{\text{tot}}\, \varepsilon^{2/3}\, g^{-7/3}\, \omega^{8/3}$, with no microscopic time scale remaining.

A. The Green-Kubo starting point

The Green-Kubo relation derived in Section S2 gives the amplitude damping rate for a swell mode with wavenumber k as

$$\Gamma(k) = \frac{1}{2E_k} \int_0^\infty \Re\left[\langle F_k(0)\, F_k^*(t)\rangle\right] \mathrm{d}t, \tag{S.79}$$

where $E_k = \frac{1}{2}|a_k|^2$ (convention of A1) and $F_k(t)$ is the projection of the stochastic vortex force onto the swell mode,

$$F_k(t) = \int \mathrm{d}^3\boldsymbol{x}\, \boldsymbol{\psi}_k^*(\boldsymbol{x}) \cdot \boldsymbol{f}_{\text{svf}}(\boldsymbol{x}, t). \tag{S.80}$$

Here $\boldsymbol{\psi}_k(\boldsymbol{x})$ is the normalised eigenfunction of the linear wave mode, with vertical structure $\propto e^{kz}$ for deep-water waves. Throughout this section, $a_k(t)$ denotes the slowly varying complex envelope of a narrowband wave packet centred at wavenumber k, not a global Fourier coefficient of the entire ocean surface. The mode function $\boldsymbol{\psi}_k$ is correspondingly understood as a wave-packet eigenfunction whose horizontal Fourier transform $\tilde{\boldsymbol{\psi}}_k(\boldsymbol{p})$ is sharply peaked at $\boldsymbol{p} = \boldsymbol{k}$ with spectral width $\Delta k \sim 1/L_{\text{env}} \ll k$ (where L_{env} is the packet length). The projection (S.80) therefore acts as a local spatial filter. It extracts the force component within the spectral bandwidth of the wave packet, not a single plane-wave Fourier coefficient that would enforce a strict $\delta(\boldsymbol{q}_h)$ selection in the wavenumber convolution. This local-envelope interpretation is consistent with the Mori-Zwanzig framework of Section S2 and with the standard WKB/Wigner representation used in wave-action transport theory [6, 36]. The turbulent field is modelled as a homogeneous, stationary random process characterised by its two-point spectrum $S_u(q, \Omega)$. Since $\Gamma(k)$ depends only on the two-point forcing correlation, higher-order cumulants do not enter at leading order.

Because $F_k \propto a_k$ (Section S2 C), the wave-energy factors in the numerator and denominator of (S.79) cancel exactly, making $\Gamma(k)$ independent of the modal normalisation (Eq. S.46). The explicit Fourier-space

calculations below are carried out in terms of F_k, retaining the $1/(2E_k)$ prefactor. The cancellation of the modal amplitude is tracked via the dimensionless overlap factor $C_E(k)$ defined in Section F.

B. Force autocorrelation in wavenumber-frequency space

The fluctuating turbulent velocity admits the Fourier representation [37, 38]

$$\boldsymbol{u}'(\boldsymbol{x},t) = \int \frac{\mathrm{d}^3 q}{(2\pi)^3} \int \frac{\mathrm{d}\Omega}{2\pi}\, \hat{\boldsymbol{u}}'(\boldsymbol{q},\Omega)\, e^{\mathrm{i}(\boldsymbol{q}\cdot\boldsymbol{x}-\Omega t)}. \tag{S.81}$$

For a statistically homogeneous and stationary field, the two-point correlation is

$$\langle \hat{u}_i'(\boldsymbol{q},\Omega)\, \hat{u}_j'^{*}(\boldsymbol{q}',\Omega')\rangle = (2\pi)^4 \delta(\boldsymbol{q}-\boldsymbol{q}')\delta(\Omega-\Omega')\, P_{ij}(\hat{\boldsymbol{q}})\, S_u(q,\Omega), \tag{S.82}$$

where $P_{ij}(\hat{\boldsymbol{q}}) = \delta_{ij} - \hat{q}_i\hat{q}_j$ enforces incompressibility and $S_u(q,\Omega)$ is the four-dimensional velocity spectrum (energy density per unit $\mathrm{d}^3 q\,\mathrm{d}\Omega$). Integrating over frequency gives the three-dimensional spectrum $S_u(q) = \int S_u(q,\Omega)\,\mathrm{d}\Omega$ (energy density per unit $\mathrm{d}^3 q$, normalised so that $\int S_u(q)\,\mathrm{d}^3 q = \frac{1}{2}\langle|\boldsymbol{u}'|^2\rangle$). The corresponding isotropic one-dimensional spectrum is $E_u(q) = 4\pi q^2 S_u(q)$. In the inertial range, $S_u(q,\Omega) = S_u(q)\,\chi(\Omega;q)$, where χ has width $\omega_q \sim (\varepsilon q^2)^{1/3}$ and unit area. The SVF $\boldsymbol{f}_{\mathrm{svf}} = \boldsymbol{u}_\phi \times \boldsymbol{\omega}'$ couples the swell to every turbulent mode simultaneously. Under Fourier transform, the vorticity becomes $\hat{\boldsymbol{\omega}}' = \mathrm{i}\boldsymbol{q}\times\hat{\boldsymbol{u}}'$. To expose the convolution structure we adopt a simplified linearly polarised orbital velocity,

$$\boldsymbol{u}_\phi(\boldsymbol{x},t) = U_0\hat{\boldsymbol{k}}\, e^{\mathrm{i}(\boldsymbol{k}\cdot\boldsymbol{x}-\omega t)} + \mathrm{c.c.}, \tag{S.83}$$

where $U_0 = a\omega$. This monochromatic form is a controlled schematic representation of the overlap structure. It isolates the wavenumber-convolution geometry that determines which turbulent scales couple to the swell. The complete phase-averaged treatment with circularly polarised deep-water orbits (Section S5 A) yields the same geometric factor $\widetilde{G}_{\mathrm{geom}} = 2/3$ for isotropic turbulence. Multiplying by the Fourier expansion of $\boldsymbol{\omega}'$ and retaining the co-rotating contribution gives

$$\hat{\boldsymbol{f}}_{\mathrm{svf}}(\boldsymbol{q},\Omega) = \mathrm{i}\,U_0\,\hat{\boldsymbol{k}}\times(\boldsymbol{q}\times\hat{\boldsymbol{u}}'(\boldsymbol{q},\Omega)), \tag{S.84}$$

where the vortex-force mode resides at $(\boldsymbol{k}+\boldsymbol{q},\ \omega+\Omega)$. Expanding via $\boldsymbol{a}\times(\boldsymbol{b}\times\boldsymbol{c}) = \boldsymbol{b}(\boldsymbol{a}\cdot\boldsymbol{c}) - \boldsymbol{c}(\boldsymbol{a}\cdot\boldsymbol{b})$,

$$\hat{\boldsymbol{f}}_{\mathrm{svf}}(\boldsymbol{q},\Omega) = \mathrm{i}\,U_0\big[\boldsymbol{q}(\hat{\boldsymbol{k}}\cdot\hat{\boldsymbol{u}}') - \hat{\boldsymbol{u}}'(\hat{\boldsymbol{k}}\cdot\boldsymbol{q})\big]. \tag{S.85}$$

The projected force (S.80) in Fourier space is

$$F_k(t) = \int \frac{\mathrm{d}^3 q}{(2\pi)^3} \int \frac{\mathrm{d}\Omega}{2\pi}\, \tilde{\psi}_k^{*}(\boldsymbol{k}+\boldsymbol{q})\cdot\hat{\boldsymbol{f}}_{\mathrm{svf}}(\boldsymbol{q},\Omega)\, e^{-\mathrm{i}(\omega+\Omega)t}, \tag{S.86}$$

where $\tilde{\psi}_k(\boldsymbol{p})$ is sharply peaked at $\boldsymbol{p} = \boldsymbol{k}$ in the horizontal, but has broad vertical support set by the depth eigenfunction e^{kz}. Because $a_k(t)$ is a narrow-band envelope (not a strict plane-wave coefficient), the projection acts as a local spectral filter with finite horizontal bandwidth $\Delta k \sim L_{\mathrm{env}}^{-1} \ll k$. The along-ray phase factor $e^{-\mathrm{i}(\Omega-\boldsymbol{q}\cdot\boldsymbol{c}_g)t}$ therefore weights the full range of locally overlapping eddy wavenumbers, not just $\boldsymbol{q}_h = \boldsymbol{0}$. As the wave packet advances at c_g, it sequentially samples turbulent structures at every horizontal wavenumber q_h. The residence time within each structure is $\sim 1/(q_h c_g)$, and the temporal memory window $\mathcal{W}_\Omega$ (Eq. S.90 below) performs the resulting frequency selection. The overlap integral that emerges after the time integration therefore runs over the full three-dimensional $\boldsymbol{q}$ space, weighted by the depth overlap e^{2kz}, the temporal memory kernel, and the geometric vertex-not by the horizontal envelope bandwidth. A turbulent mode evaluated along the wave-packet trajectory $\boldsymbol{x}(t) = \boldsymbol{x}_0 + \boldsymbol{c}_g t$ acquires the advected phase

$$e^{\mathrm{i}(\boldsymbol{q}\cdot\boldsymbol{x}-\Omega t)}\big|_{\boldsymbol{x}=\boldsymbol{x}_0+\boldsymbol{c}_g t} = e^{\mathrm{i}\boldsymbol{q}\cdot\boldsymbol{x}_0}\, e^{-\mathrm{i}(\Omega-\boldsymbol{q}\cdot\boldsymbol{c}_g)t}, \tag{S.87}$$

so the effective frequency seen by the packet is $\Omega_{\rm eff} = \Omega - \boldsymbol{q}\cdot\boldsymbol{c}_g$. The force autocorrelation $\langle F_k(0)\, F_k^*(t)\rangle$ involves two integrals over $(\boldsymbol{q}, \Omega)$. The turbulent correlation (S.82) collapses one via the delta functions, and the tensor contraction defines a scalar vertex $|V(\boldsymbol{q}; k)|^2$,

$$\langle F_k(0)\, F_k^*(t)\rangle = \int \mathrm{d}^3q \int \mathrm{d}\Omega\, |V(\boldsymbol{q}; k)|^2\, S_u(q, \Omega)\, e^{-\mathrm{i}(\Omega - \boldsymbol{q}\cdot\boldsymbol{c}_g)t}. \tag{S.88}$$

Inserting into the Green-Kubo relation (S.79) and performing the time integral, which converges because the force autocorrelation has finite memory (A6), yields

$$\boxed{\Gamma(k) = \frac{1}{2E_k} \int \mathrm{d}^3q \int \mathrm{d}\Omega\, S_u(q, \Omega)\, |V(\boldsymbol{q}; k)|^2\, \mathcal{W}_\Omega(\Omega - \boldsymbol{q}\cdot\boldsymbol{c}_g),} \tag{S.89}$$

where the *temporal memory window*

$$\mathcal{W}_\Omega(\Delta\Omega) \;\equiv\; \mathrm{Re}\int_0^\infty e^{-t/\tau_{\rm eff}}\, e^{-\mathrm{i}\Delta\Omega\, t}\, \mathrm{d}t \;=\; \frac{\tau_{\rm eff}^{-1}}{\tau_{\rm eff}^{-2} + \Delta\Omega^2} \tag{S.90}$$

is a Lorentzian peaked at $\Delta\Omega = 0$ with width $\sim \tau_{\rm eff}^{-1}$. In the idealised infinite-memory limit $\tau_{\rm eff} \to \infty$, the window reduces to the distributional form $\pi\delta(\Delta\Omega)$. The finite correlation time of the force process broadens this selection, concentrating contributions near the advective Doppler frequency without excluding any turbulent scale. Equation (S.89) sums contributions from every turbulent mode, weighted by the available energy $S_u(q, \Omega)$, the coupling geometry $|V(\boldsymbol{q}; k)|^2$, and the decorrelation weight $\mathcal{W}_\Omega$. Equation (S.89) therefore weights all locally overlapping turbulent modes through the same Doppler-shifted temporal memory kernel, rather than through a strict resonant matching rule. In the sections that follow, angular integrations over $\boldsymbol{q}$ are absorbed into a geometric factor $\widetilde{G}_{\rm geom}$ and a scale-selection window $\mathcal{S}(q/k)$. The remaining spectral integrals use the one-dimensional spectrum $E_u(q) = 4\pi q^2 S_u(q)$.

C. Vortex-force vertex and angular integration

The vertex $|V(\boldsymbol{q}; k)|^2$ governs the coupling strength between a turbulent Fourier mode and the swell. Choose coordinates with $\hat{\boldsymbol{k}} = \boldsymbol{e}_x$ and let $\boldsymbol{q}$ make angle θ with the swell direction. Incompressibility requires $\boldsymbol{q}\cdot\hat{\boldsymbol{u}}' = 0$, so $\hat{\boldsymbol{u}}'$ lies in the plane perpendicular to $\hat{\boldsymbol{q}}$. Constructing an orthonormal basis $\{\hat{\boldsymbol{q}}, \boldsymbol{e}_1, \boldsymbol{e}_2\}$ with $\boldsymbol{e}_1$ in the plane of $\hat{\boldsymbol{k}}$ and $\hat{\boldsymbol{q}}$,

$$\boldsymbol{e}_x = \cos\theta\, \hat{\boldsymbol{q}} + \sin\theta\, \boldsymbol{e}_1, \tag{S.91}$$

and $\hat{\boldsymbol{u}}' = u_1'\boldsymbol{e}_1 + u_2'\boldsymbol{e}_2$. Applying the BAC-CAB identity to $\hat{\boldsymbol{f}}_{\rm svf} = \boldsymbol{u}_\phi \times (\mathrm{i}\boldsymbol{q} \times \hat{\boldsymbol{u}}')$ and evaluating the inner products gives

$$|\hat{\boldsymbol{f}}_{\rm svf}|^2 = U_0^2 q^2 \left[u_1'^2 + u_2'^2 \cos^2\theta\right]. \tag{S.92}$$

For isotropic turbulence, $\langle u_1'^2\rangle = \langle u_2'^2\rangle = \frac{1}{2}u'^2(q)$, so the vertex is

$$|V(\boldsymbol{q}; k)|^2 \propto U_0^2\, q^2\, g(\cos\theta), \qquad g(\cos\theta) = \tfrac{1}{2}(1 + \cos^2\theta). \tag{S.93}$$

Integrating over solid angle, $\int \mathrm{d}\Omega_q\, g = \frac{1}{2}(4\pi + \frac{4\pi}{3}) = \frac{8\pi}{3}$, gives the direction-averaged vertex

$$\int \mathrm{d}\Omega_q\, |V(\boldsymbol{q}; k)|^2 = U_0^2\, q^2\, G_{\rm geom}, \qquad G_{\rm geom} = \frac{8\pi}{3}. \tag{S.94}$$

We define the normalised geometric factor

$$\widetilde{G}_{\rm geom} \;\equiv\; \frac{G_{\rm geom}}{4\pi} = \frac{2}{3}, \tag{S.95}$$

which enters $C_{\rm tot}$ as an order-unity prefactor. The derivation above uses a linearly polarised orbital velocity as a pedagogical device. The full phase-averaged calculation with circularly polarised deep-water orbits (Section S5 A) yields the same value $\widetilde{G}_{\rm geom} = 2/3$ for isotropic turbulence.

D. Scale-selection window

The kinematic vertex derived above shows that every turbulent Fourier mode couples to the swell with strength proportional to q^2, reflecting the curl in the vorticity definition. The net contribution of each mode to the damping rate, however, also depends on the spatial overlap between the eddy and the wave orbital layer. This depth-overlap geometry is captured by a dimensionless scale-selection window $\mathcal{S}(q/k)$, defined as the ratio of the depth-integrated mode-projected force variance to the bare kinematic vertex,

$$\boxed{\mathcal{S}\Big(\frac{q}{k}\Big) \;\equiv\; \frac{\text{depth-integrated } |F_k(\boldsymbol{q})|^2}{U_0^2\, q^2\, \widetilde{G}_{\text{geom}}}\,.} \tag{S.96}$$

By construction, $\mathcal{S}$ depends only on $x \equiv q/k$ and satisfies $\mathcal{S}(x) \propto x^2$ for $x \ll 1$, $\mathcal{S}(x) = O(1)$ near $x \sim 1$, and $\mathcal{S}(x) \lesssim C\,x^{-1}$ for $x \gg 1$. These asymptotic behaviours ensure convergence of the Green-Kubo integral at both ends. The effective vertex including depth overlap is

$$\boxed{|V(\boldsymbol{q};k)|^2_{\text{eff}} = U_0^2\, q^2\, \widetilde{G}_{\text{geom}}\, \mathcal{S}\Big(\frac{q}{k}\Big)\,.} \tag{S.97}$$

Ultraviolet suppression from vertical penetration mismatch. The wave orbital energy decays as $|\boldsymbol{u}_\phi(z)|^2 \propto e^{2kz}$ with penetration depth $\sim (2k)^{-1}$. The depth-projection integral is

$$I(k,q_z) = \int_{-\infty}^{0} \mathrm{d}z\; e^{2kz}\, e^{\mathrm{i}q_z z} = \frac{1}{2k - \mathrm{i}q_z}\,, \qquad |I|^2 = \frac{1}{4k^2 + q_z^2}\,. \tag{S.98}$$

This suppresses eddies with $q_z \gg k$. Averaging $|I|^2$ over the turbulent-wavenumber sphere, only a polar cap of angular width $\Delta\theta \sim k/q$ contributes efficiently for $q \gg k$, yielding a floor $\mathcal{S}(x) \lesssim C\,x^{-1}$. In the oceanic mixed layer, turbulent enstrophy is further concentrated toward the surface by wave-breaking injection and Langmuir circulation [39, 40], steepening the suppression beyond this floor.

To establish unconditional convergence of the Green-Kubo integral, suppose $|\boldsymbol{u}_\phi|^2 \propto e^{2kz}$, the turbulence follows the Kolmogorov spectrum $E_u \propto q^{-5/3}$, and the effective decorrelation time satisfies $\tau_{\text{eff}} \le C_\tau(\varepsilon q^2)^{-1/3}$. The three-dimensional integrand then has three factors. Spectrum $S_u \propto q^{-11/3}$, bare vertex $\propto q^2$, and depth projection $|I|^2 = (4k^2 + q_z^2)^{-1}$. The polar-angle integral $\int_{-1}^{1} \mathrm{d}\zeta/(4k^2 + q^2\zeta^2) \le \pi/(2kq)$ bounds the radial integrand by $\lesssim q^{-4/3}$, which is integrable on $[Q,\infty)$. Comparing with the one-dimensional form identifies $\mathcal{S}(x) \sim x^{-1}$ as the floor from depth projection alone. The parametric family $\widehat{W}_\alpha(x) = x^2/(1+x^2)^\alpha$ with $\alpha \in [2, 5/2]$ used in Section S5 B for sensitivity analysis incorporates environmental effects beyond the floor. The baseline $\alpha = 2$ gives $C_{\mathcal{S}} = \pi/6 \approx 0.52$, and $C_{\mathcal{S}}$ varies by a factor of 2.7 across the range, translating into only a factor of 1.4 in the predicted attenuation rate.

Infrared suppression from Galilean invariance. The behaviour $\mathcal{S}(x) \propto x^2$ as $x \to 0$ is not a modelling choice but a structural consequence of two conservation laws.

At $\boldsymbol{q} = \boldsymbol{0}$ the turbulent velocity is spatially uniform and its vorticity vanishes, so $F_k = 0$. Galilean invariance ensures that a uniform current produces only a Doppler shift without changing the wave energy. This zeroth-order vanishing is already encoded in the bare vertex factor q^2.

At $O(q/k)$ the vorticity is nonzero and the vortex force is finite. Denoting by $F_k^{(1)}$ the $O(q/k)$ component of the mode-projected force, a linearly varying current refracts the wave while conserving wave action at leading order [41]. The $O(q/k)$ force therefore drives only a reactive frequency shift along the ray. It enters the imaginary part of the self-energy, contributing to $\Delta\omega_k$, but not the dissipative real part Γ,

$$\mathrm{Re}\int_0^\infty \langle F_k^{(1)}(0)\, F_k^{(1)*}(t)\rangle\, \mathrm{d}t = 0. \tag{S.99}$$

At $O(q^2/k^2)$ the curvature of the current field induces genuine scattering that does not reverse upon transit, so

$$\boxed{\mathcal{S}(x) = O(x^2) \quad \text{as} \quad x = q/k \to 0\,, \qquad \text{i.e.} \quad \mathcal{S}(0) = \mathcal{S}'(0) = 0.} \tag{S.100}$$

The total effective coupling for $q \ll k$ therefore scales as $|V_{\rm eff}|^2 \propto q^4/k^2$, with the bare vertex q^2 and the window suppression $(q/k)^2$ contributing equally to infrared convergence. Large eddies, despite their abundant Kolmogorov energy, contribute negligibly to swell dissipation.

To the authors' knowledge, the scale-selection window has not been derived explicitly in prior wave-turbulence interaction theories. Rapid distortion theory [42] treats $\ell \ll \lambda_w$, implicitly confirming ultraviolet convergence but not identifying $\mathcal{S}(x)$. The quasi-linear theory of McWilliams [6] evaluates the vortex force for a deterministic current at a single wavenumber, so spectral integration does not arise. WKB ray tracing [36] assumes $q \ll k$, where ultraviolet convergence is moot. The present analysis fills this gap.

E. Frequency integration and the effective correlation time

For homogeneous, stationary turbulence the four-dimensional spectrum factors as [43]

$$S_u(q,\Omega) = S_u(q)\,\chi(\Omega;q), \qquad \int_{-\infty}^{\infty} \chi(\Omega;q)\,\mathrm{d}\Omega = 1. \tag{S.101}$$

Inserting into Eq. (S.89) and performing the frequency integral yields

$$\Gamma(k) = \frac{1}{2E_k}\int \mathrm{d}^3q\, S_u(q)\,|V(\boldsymbol{q};k)|^2\,\tau_{\rm eff}(q;k), \tag{S.102}$$

with

$$\tau_{\rm eff}(q;k) = \int_{-\infty}^{\infty} \chi(\Omega;q)\,\mathcal{W}_\Omega(\Omega - \boldsymbol{q}\cdot\boldsymbol{c}_g)\,\mathrm{d}\Omega. \tag{S.103}$$

Equation (S.103) is the exact definition of the effective memory time. The Lorentzian parametrisation used for $\mathcal{W}_\Omega$ in Eq. (S.90) is a convenient approximation whose width is set *a posteriori* by the dominant decorrelation mechanism, not assumed in advance. Two timescales compete inside this integral. The intrinsic eddy turnover time $\tau_{\rm eddy}(q) \sim (\varepsilon q^2)^{-1/3}$ measures how fast the eddy forgets its initial configuration through the cascade. The advective decorrelation time

$$\tau_{\rm adv}(q) \sim \frac{1}{q\,c_g} \tag{S.104}$$

is the time for the advected phase $\exp(\mathrm{i}\boldsymbol{q}\cdot\boldsymbol{c}_g\,t)$ in the force autocorrelation to accumulate an $O(1)$ shift as the wave-energy trajectory traverses one correlation length q^{-1}. This is the wave-propagation analogue of the Kraichnan-Tennekes random sweeping hypothesis [44, 45]. For oceanic swell, $c_g \sim$ 10-30 $\mathrm{m\,s^{-1}}$ exceeds $u' \sim$ 0.01-0.1 $\mathrm{m\,s^{-1}}$ by two to three orders of magnitude, so $\tau_{\rm adv} \ll \tau_{\rm eddy}$ at every scale and advective sweeping governs the decorrelation throughout. The effective correlation time therefore reduces to

$$\tau_{\rm eff}(q;k) \simeq \frac{C_\tau}{q\,c_g(k)}, \tag{S.105}$$

where $C_\tau = \int_0^\infty \mathcal{R}(s)\,\mathrm{d}s$ is a dimensionless shape factor of order unity determined by the spatial correlation function of inertial-range eddies (Section C). The crossover wavenumber at which $\tau_{\rm eddy}$ and $\tau_{\rm adv}$ become comparable is $q_* \sim \varepsilon/c_g^3 \sim 10^{-9}\,\mathrm{m^{-1}}$, seven orders of magnitude below the swell wavenumber $k \sim 10^{-2}\,\mathrm{m^{-1}}$. The advective limit therefore holds at all scales that contribute to the Green-Kubo integral.

At the dominant coupling scale $q \sim k$, the eddy diameter $\ell \sim \lambda$ is much smaller than the wave-packet envelope $L_{\rm env} \sim O(10\lambda)$, so the geometric overlap time $\tau_{\rm transit} \sim L_{\rm env}/c_g$ far exceeds the wave period. The decorrelation time is set not by this overlap duration but by phase decorrelation. As the energy trajectory advances by one eddy diameter, the advected phase $\exp(\mathrm{i}\boldsymbol{q}_h\cdot\boldsymbol{c}_g t)$ completes an $O(1)$ rotation, and successive patches contribute to the Green-Kubo integral with randomised phases (Section A).

Two limiting models for the force decorrelation illuminate the physics. In the frozen-turbulence limit ($\delta \ll 1$), the eddy does not evolve during the encounter and the force autocorrelation at scale q reduces to a spatial correlation sampled at rate c_g, $C_{F,q}(t) \approx C_{F,q}(0)\,\mathcal{R}(qc_g t)$. The Green-Kubo integral then

gives $\tau_{\rm eff} = C_\tau/(qc_g)$ directly. This is the model adopted throughout. An alternative retains the intrinsic temporal decay $R(q,t) = \exp[-t/\tau_{\rm eddy}(q)]$, giving a Lorentzian weight

$$\int_0^\infty \mathrm{d}t\; R(q,t)\cos(\boldsymbol{q}_h\cdot\boldsymbol{c}_g t) = \frac{\tau_{\rm eddy}(q)}{1+(\boldsymbol{q}_h\cdot\boldsymbol{c}_g)^2\tau_{\rm eddy}^2(q)}. \tag{S.106}$$

In the sweep-dominated regime $|\boldsymbol{q}_h\cdot\boldsymbol{c}_g|\,\tau_{\rm eddy}\gg 1$, this reduces to $\propto \varepsilon^{1/3}q^{-4/3}c_g^{-2}$, carrying a different q-scaling from the spatial-correlation result $\propto q^{-1}c_g^{-1}$. The two models describe different physics. The temporal-decay model treats the eddy as decaying exponentially, with advection modulating the phase. The spatial model treats the eddy as frozen, with decorrelation arising entirely from spatial sampling. For swell ($\delta\sim 10^{-3}$-10^{-2}), the eddy barely evolves during the encounter and the frozen-field model is accurate to $O(\delta)$. The temporal-decay model would apply in the opposite slow-probe limit $\tau_{\rm adv}\gg\tau_{\rm eddy}$, which does not hold for ocean swell.

F. Reduced one-dimensional integral and modal normalisation

Combining the direction-averaged vertex (Eqs. (S.94) and (S.97)), the advection-dominated correlation time $\tau_{\rm eff}\simeq C_\tau/(q\,c_g)$ (Eq. (S.105)), and converting to the one-dimensional spectrum $E_u(q) = 4\pi q^2 S_u(q)$, the Green-Kubo expression (S.102) reduces to

$$\boxed{\Gamma(k) = \frac{C_\tau\,\widetilde{G}_{\rm geom}\,C_E(k)}{2\,c_g(k)}\int_0^\infty \mathrm{d}q\,E_u(q)\,q\,\mathcal{S}\Big(\frac{q}{k}\Big).} \tag{S.107}$$

The dimensionless depth-overlap coefficient $C_E(k)$ collects the dependence on the vertical structure and modal normalisation of the swell eigenfunction. For deep-water linear orbits $\boldsymbol{u}_\phi(z)\propto e^{kz}$, the depth-integrated orbital kinetic energy per unit horizontal area is

$$\int_{-\infty}^0 \langle|\boldsymbol{u}_\phi(z)|^2\rangle_t\,\mathrm{d}z = \frac{(a\omega)^2}{2k} = \tfrac{1}{2}a^2 g = E_k, \tag{S.108}$$

using $\omega^2 = gk$ and the convention $E_k = \frac{1}{2}ga^2$ (equivalently $\frac{1}{2}|a_k|^2$ under A1). The depth-overlap coefficient is defined as

$$C_E(k) \equiv \frac{\displaystyle\int_{-\infty}^0 \langle|\boldsymbol{u}_\phi(z)|^2\rangle_t\,\mathrm{d}z}{E_k} = 1 \qquad \text{(deep-water linear orbits).} \tag{S.109}$$

The cancellation works as follows. The surface-value ratio $U_0^2/(2E_k) = \omega^2/g = k$ from the Green-Kubo normalisation and vertex is exactly compensated by the k^{-1} from the depth integral, leaving no residual k-dependence in the prefactor. Departures from the ideal exponential profile (finite depth, finite mixed-layer thickness, or modified orbital structure) renormalise C_E to an $O(1)$ value absorbed into $C_{\rm tot}$ in Section S5.

S4. From the force autocorrelation to the swell attenuation law

In the inertial subrange the velocity spectrum takes the Kolmogorov form [32]

$$E_u(q) = C_K\,\varepsilon_{\rm eff}^{2/3}\,q^{-5/3}, \tag{S.110}$$

with $C_K\approx 1.5$ [38, 46]. For 14 s swell ($k\approx 0.021$ rad m^{-1}) in a typical mixed layer ($L_0\sim$ 10-100 m, Kolmogorov microscale $\eta\sim 1$ mm), the separation $\eta\ll k^{-1}\lesssim L_0$ places the swell-interacting eddies within the inertial subrange (Section S5 G). Inserting Eq. (S.110) into the one-dimensional Green-Kubo form (S.107) and changing variables $x = q/k$ yields

$$\int_0^\infty \mathrm{d}q\,q^{-2/3}\,\mathcal{S}\Big(\frac{q}{k}\Big) = k^{1/3}\int_0^\infty x^{-2/3}\,\mathcal{S}(x)\,\mathrm{d}x \equiv k^{1/3}\,C_{\mathcal{S}}, \tag{S.111}$$

where $C_{\mathcal{S}}$ depends only on the shape of the scale-selection window. For the baseline model $\mathcal{S}(x) = x^2/(1+x^2)^2$, $C_{\mathcal{S}} = \pi/6 \approx 0.52$ (Table S1 in Section S5 B gives other choices). Collecting all order-unity constants into $C_\Gamma \equiv C_\tau C_K C_{\mathcal{S}} \widetilde{G}_{\text{geom}} C_E/2$, with $C_E = 1$ for deep-water exponential orbits (Eq. S.109), the temporal damping rate becomes

$$\boxed{\Gamma(k) \simeq C_\Gamma \, \frac{\varepsilon_{\text{eff}}^{2/3}}{c_g(k)} \, k^{1/3}.} \tag{S.112}$$

Converting to spatial decay via $\mu_E = 2\Gamma/c_g$ (the factor 2 reflects energy $\propto$ amplitude^2) and using $c_g = \frac{1}{2}\sqrt{g/k}$ gives $c_g^{-2} = 4k/g$, so

$$\mu_E(k) = 8 C_\Gamma \, \varepsilon_{\text{eff}}^{2/3} \, \frac{k^{4/3}}{g}. \tag{S.113}$$

Substituting $k = \omega^2/g$ yields the scaling law announced in the main text,

$$\boxed{\mu_E(\omega) \simeq C_{\text{tot}} \, \varepsilon_{\text{eff}}^{2/3} \, g^{-7/3} \, \omega^{8/3}, \qquad C_{\text{tot}} = 8C_\Gamma = 4\, C_K \, \widetilde{G}_{\text{geom}} \, C_{\mathcal{S}} \, C_\tau \, C_E.} \tag{S.114}$$

The $\omega^{8/3}$ exponent combines $k^{1/3}$ from the Kolmogorov spectrum at the swell-selected scale, k^1 from the temporal-to-spatial conversion $c_g^{-2} \propto k$, and the deep-water dispersion relation $k = \omega^2/g$. The decomposition of C_{tot} into individually constrained factors is given in Section S5. The effective dissipation rate entering the law is the mode-weighted average over the wave-turbulence interaction layer,

$$\boxed{\varepsilon_{\text{eff}}(k) \equiv \frac{\int_{-H_{\text{int}}}^{0} \varepsilon(z)\, e^{2kz}\, \mathrm{d}z}{\int_{-H_{\text{int}}}^{0} e^{2kz}\, \mathrm{d}z},} \tag{S.115}$$

where $H_{\text{int}}(k) = \min\{1/k,\, H_{\text{ml}}\}$. The weights e^{2kz} reflect the decay of orbital energy with depth. ε_{eff} is therefore dominated by the upper $\sim (2k)^{-1} \approx$ 15-40 m of the water column. In Section S5 E the wall-law dissipation profile is substituted explicitly, with the depth coordinate measured downward ($z \geq 0$) and kernel e^{-2kz}. The two conventions are equivalent under $z \to -z$. Equation (S.114) is the closed-form consequence of the factorised Green-Kubo closure developed in this section. The $\omega^{8/3}$ exponent is fixed by the Kolmogorov power counting, deep-water dispersion, and the advection-dominated memory time. Section S5 quantifies the order-unity uncertainty associated with the window shape, temporal correlator, and vertical structure, which affects only the prefactor.

S5. Order-of-magnitude of the prefactor C_{tot} and robustness of the Kolmogorov closure

The total prefactor in the swell attenuation coefficient decomposes as

$$\boxed{C_{\text{tot}} = 4\, C_K \, \widetilde{G}_{\text{geom}} \, C_{\mathcal{S}} \, C_\tau \, C_E.} \tag{S.116}$$

Each factor is evaluated in the subsections below. Under baseline assumptions the product evaluates to $C_{\text{tot}} = 2\pi/3 \approx 2.09$. Propagating the physically constrained ranges yields $C_{\text{tot}} \in [1.10,\, 3.34]$ (assembled in Section I). The decomposition into $C_{\mathcal{S}}$, C_τ, C_E and ε_{eff} is a controlled factorised closure rather than an exact theorem when the depth structure of enstrophy depends explicitly on turbulent wavenumber. The purpose of this section is therefore twofold. One is to assign physically constrained order-unity ranges to each factor, and the other is to show that the resulting uncertainty affects only the prefactor, not the $\omega^{8/3}$ scaling exponent.

A. The geometric vertex factor $\widetilde{G}_{\text{geom}}$

The force-autocorrelation expression for the swell attenuation rate (Eq. (S.89)) contains the squared vortex-force vertex

$$|V(\boldsymbol{q}; k)|^2 \;\equiv\; \frac{1}{8\pi^2} \int_0^{2\pi} \mathrm{d}\phi \int \mathrm{d}\Omega_q \, \left| \boldsymbol{u}_\phi(\phi) \times \boldsymbol{\omega}'(\boldsymbol{q}) \right|^2, \tag{S.117}$$

where the two integrations represent, respectively, an average over the wave phase $\phi = kx - \omega t$ (one full cycle, normalised by 2π) and an average over the direction of the turbulent wavenumber $\hat{\boldsymbol{q}}$ on the unit sphere (normalised by 4π, appropriate for isotropic turbulence). The geometric vertex factor $\widetilde{G}_{\mathrm{geom}}$ collects all purely kinematic contributions, so that

$$|V|^2 \;=\; \widetilde{G}_{\mathrm{geom}}\, U_0^2\, \langle |\boldsymbol{\omega}'|^2 \rangle, \tag{S.118}$$

with $U_0 = a_k \omega_k$ the surface orbital speed and $\langle |\boldsymbol{\omega}'|^2 \rangle$ the local enstrophy. Consider a monochromatic deep-water wave propagating along $+\hat{\boldsymbol{x}}$ with wavenumber k and frequency ω. At depth $z \geq 0$ (measured downward from the surface) the orbital velocity is

$$\boldsymbol{u}_\phi(z,\phi) = U_0\, e^{-kz}\big(\cos\phi\, \hat{\boldsymbol{x}} + \sin\phi\, \hat{\boldsymbol{z}}\big), \qquad \phi = kx - \omega t. \tag{S.119}$$

The motion is circularly polarised in the x-z plane. Horizontal and vertical amplitudes are equal at every depth. The phase-averaged second-moment tensor is

$$M_{ij} \;\equiv\; \langle u_{\phi,i}\, u_{\phi,j} \rangle_\phi \;=\; \frac{U_0^2}{2}\big(\hat{x}_i \hat{x}_j + \hat{z}_i \hat{z}_j\big) \;=\; \frac{U_0^2}{2}\big(\delta_{ij} - \hat{y}_i \hat{y}_j\big), \tag{S.120}$$

whose trace is $M_{ii} = U_0^2$. The vanishing of M_{yy} reflects the absence of any $\hat{\boldsymbol{y}}$ component in deep-water orbits. This asymmetry is the root cause of the $\{1, \frac{1}{2}, \frac{1}{2}\}$ vorticity weights derived next. Let $\boldsymbol{\omega}' = (\omega'_x, \omega'_y, \omega'_z)$ denote the turbulent vorticity. The vortex force $\mathbf{F} = \boldsymbol{u}_\phi \times \boldsymbol{\omega}'$ has components

$$\mathbf{F} = U_0 \begin{pmatrix} -\sin\phi\; \omega'_y \\ \sin\phi\; \omega'_x - \cos\phi\; \omega'_z \\ \cos\phi\; \omega'_y \end{pmatrix}. \tag{S.121}$$

Since $\langle \boldsymbol{u}_\phi \rangle_\phi = \mathbf{0}$ for a monochromatic wave, the phase-averaged force vanishes identically,

$$\big\langle \boldsymbol{u}_\phi \times \boldsymbol{\omega}' \big\rangle_\phi = \langle \boldsymbol{u}_\phi \rangle_\phi \times \boldsymbol{\omega}' = \mathbf{0}\,, \tag{S.122}$$

consistent with the identification of $\boldsymbol{f}_{\mathrm{svf}}$ as a zero-mean stochastic force (Section S1). The Green-Kubo relation (S.79), however, involves the autocorrelation $\langle F_k(0)\, F_k^*(t) \rangle$, a second-order quantity whose zero-lag value is set by the phase-averaged squared amplitude $\langle |\mathbf{F}|^2 \rangle_\phi$, which we evaluate. Expanding the squared norm gives

$$|\mathbf{F}|^2 = U_0^2 \Big[\omega_y'^2 + \sin^2\!\phi\; \omega_x'^2 + \cos^2\!\phi\; \omega_z'^2 - 2\sin\phi\cos\phi\; \omega'_x \omega'_z \Big]. \tag{S.123}$$

The phase averages $\langle \sin^2\phi \rangle_\phi = \langle \cos^2\phi \rangle_\phi = \frac{1}{2}$ and $\langle \sin\phi\cos\phi \rangle_\phi = 0$ then give the central intermediate result,

$$\boxed{\big\langle |\boldsymbol{u}_\phi \times \boldsymbol{\omega}'|^2 \big\rangle_\phi = U_0^2 \big[\omega_y'^2 + \tfrac{1}{2}\big(\omega_x'^2 + \omega_z'^2\big) \big]\,.} \tag{S.124}$$

Equation (S.124) holds for arbitrary turbulence statistics. It depends only on the deep-water dispersion relation through the polarisation of $\boldsymbol{u}_\phi$. The origin of the unequal weights $\{1, \frac{1}{2}, \frac{1}{2}\}$ for the components $\{\omega'_y, \omega'_x, \omega'_z\}$ is purely geometric. The out-of-plane component ω'_y is perpendicular to the orbital plane $\mathrm{span}\{\hat{\boldsymbol{x}}, \hat{\boldsymbol{z}}\}$ at every phase, so it always produces a force and enters with full weight. The component ω'_x, by contrast, is parallel to $\boldsymbol{u}_\phi$ when $\phi = 0$ (no cross product) and perpendicular when $\phi = \pi/2$ (maximal cross product). Averaging over the wave cycle yields a factor of one half. The same argument with $x \leftrightarrow z$ applies to ω'_z. For later use we note the equivalent tensor form obtained from the identity $|\mathbf{a}\times\mathbf{b}|^2 = |\mathbf{a}|^2|\mathbf{b}|^2 - (\mathbf{a}\cdot\mathbf{b})^2$,

$$\big\langle |\boldsymbol{u}_\phi \times \boldsymbol{\omega}'|^2 \big\rangle_\phi = M_{ii}\; \omega'_j \omega'_j \;-\; M_{ij}\; \omega'_i \omega'_j = U_0^2 |\boldsymbol{\omega}'|^2 - \frac{U_0^2}{2}\big(\omega_x'^2 + \omega_z'^2\big), \tag{S.125}$$

which recovers Eq. (S.124) upon expanding $|\boldsymbol{\omega}'|^2 = \omega_x'^2 + \omega_y'^2 + \omega_z'^2$. For homogeneous, isotropic turbulence $\langle \omega_x'^2 \rangle = \langle \omega_y'^2 \rangle = \langle \omega_z'^2 \rangle = \frac{1}{3}\langle |\boldsymbol{\omega}'|^2 \rangle$. Substituting into Eq. (S.124),

$$\left\langle |\boldsymbol{u}_\phi \times \boldsymbol{\omega}'|^2 \right\rangle_{\phi,\mathrm{iso}} = U_0^2 \langle |\boldsymbol{\omega}'|^2 \rangle \left[\tfrac{1}{3} + \tfrac{1}{2}\left(\tfrac{1}{3} + \tfrac{1}{3}\right) \right] = \frac{2}{3} U_0^2 \langle |\boldsymbol{\omega}'|^2 \rangle, \tag{S.126}$$

and comparing with Eq. (S.118) immediately yields

$$\boxed{\widetilde{G}_{\mathrm{geom}}^{(\mathrm{iso})} = \frac{2}{3}\,.} \tag{S.127}$$

As an independent check we re-derive the isotropic result in wavenumber space. For an isotropic vorticity field the spectral tensor is

$$\Phi_{ij}(\boldsymbol{q}) \;\equiv\; \langle \omega_i'(\boldsymbol{q})\, \omega_j'^{*}(\boldsymbol{q}) \rangle = \frac{E_\omega(q)}{4\pi} (\delta_{ij} - \hat{q}_i \hat{q}_j), \tag{S.128}$$

where $E_\omega(q) = q^2 E_u(q)$ is the enstrophy spectrum. Combining Eq. (S.125) with (S.128), the phase-averaged vertex at a fixed turbulent-wavenumber direction $\hat{\boldsymbol{q}}$ is $g(\hat{\boldsymbol{q}}) = M_{ii}\,\Phi_{jj} - M_{ij}\,\Phi_{ij}$. Writing $A \equiv E_\omega/(4\pi)$, we obtain

$$g(\hat{\boldsymbol{q}}) = A U_0^2 \left(\frac{3}{2} - \frac{1}{2}\hat{q}_y^2 \right). \tag{S.129}$$

Integrating over the unit sphere ($\int \mathrm{d}\Omega_q = 4\pi$, $\int \hat{q}_y^2\, \mathrm{d}\Omega_q = 4\pi/3$) and normalising by the spectral enstrophy $\langle |\boldsymbol{\omega}'|^2 \rangle_q = 4\pi\,\mathrm{Tr}\,\Phi = 8\pi A$ gives $\widetilde{G}_{\mathrm{geom}} = (16\pi/3)/(8\pi) = 2/3$, confirming the physical-space value (S.127). Mixed-layer turbulence is not perfectly isotropic. Vertical motions are suppressed relative to horizontal ones by buoyancy and the free surface [47, 48]. We model this through an axisymmetric vorticity variance tensor,

$$\langle \omega_x'^2 \rangle = \langle \omega_y'^2 \rangle \equiv \sigma_h^2, \qquad \langle \omega_z'^2 \rangle \equiv \sigma_v^2, \qquad \langle \omega_i' \omega_j' \rangle = 0 \;(i \neq j), \tag{S.130}$$

with the anisotropy ratio $R_u \equiv u_h'/u_v' \approx \sigma_h/\sigma_v$ [49]. Inserting into Eq. (S.124) and normalising by $\langle |\boldsymbol{\omega}'|^2 \rangle = 2\sigma_h^2 + \sigma_v^2$ gives

$$\boxed{\widetilde{G}_{\mathrm{geom}}(R_u) = \frac{3R_u^2 + 1}{2(2R_u^2 + 1)}\,.} \tag{S.131}$$

As an independent verification we parametrise the directional enstrophy spectrum by $S_\omega(\boldsymbol{q}) = [E_\omega(q)/(4\pi)][1 + \beta\, P_2(\cos\theta_q)]$ with $P_2(x) = (3x^2 - 1)/2$. The velocity anisotropy relates to the spectral parameter via

$$\beta = \frac{10(R_u^2 - 1)}{2R_u^2 + 1}\,. \tag{S.132}$$

Evaluating the weighted solid-angle integral with the four angular moments ($\int \mathrm{d}\Omega = 4\pi$, $\int P_2\, \mathrm{d}\Omega = 0$, $\int \hat{q}_y^2\, \mathrm{d}\Omega = 4\pi/3$, $\int \hat{q}_y^2 P_2\, \mathrm{d}\Omega = -4\pi/15$) and normalising recovers exactly Eq. (S.131). At $R_u = 1$ (isotropy) we recover $\widetilde{G}_{\mathrm{geom}} = 2/3$. As $R_u \to \infty$ (purely horizontal turbulence) the factor saturates at $3/4$, while $R_u \to 0$ (purely vertical turbulence) gives $1/2$. Circular polarisation therefore confines $\widetilde{G}_{\mathrm{geom}}$ to the narrow interval $[1/2,\ 3/4]$. For comparison, a hypothetical linearly polarised wave gives a wider range $[1/2,\ 1]$. In the upper ocean, $R_u \sim$ 1-2 [47, 48], over which $\widetilde{G}_{\mathrm{geom}}$ varies from 0.667 to $\simeq 0.722$, an $O(8\%)$ shift. Two further effects, finite-depth elliptical polarisation and wind-swell obliquity, can each perturb $\widetilde{G}_{\mathrm{geom}}$ by $\sim 10\%$ for a single realisation, but average out over trans-basin propagation. We adopt $\widetilde{G}_{\mathrm{geom}} = 2/3$ with a physical range $[2/3,\ 3/4]$ for deep-water swell.

B. The scale-selection constant $C_{\mathcal{S}}$

The scale-selection window $\mathcal{S}(q/k)$ derived in Section D enters the scaling law only through the dimensionless integral $C_{\mathcal{S}} = \int_0^\infty x^{-2/3}\mathcal{S}(x)\,\mathrm{d}x$ (Eq. S.111). The window peaks at $q \sim k$, grows as x^2 in the infrared, and rolls off in the ultraviolet. All three features are fixed by wave-eddy geometry. Its amplitude depends on the vertical distribution of mixed-layer enstrophy, parameterised here by a single exponent. Because every admissible window shares the same infrared ($\mathcal{S} \propto x^2$) and ultraviolet ($\mathcal{S} \lesssim Cx^{-1}$) asymptotics, the integrand $x^{-2/3}\mathcal{S}(x)$ is unconditionally convergent at both ends and the change of variables $x = q/k$ always extracts the factor $k^{1/3}$ that produces the $\omega^{8/3}$ exponent (Eq. S.111). Varying the window shape therefore changes only the numerical value of $C_{\mathcal{S}}$, not the scaling law itself. We adopt the rational family

$$\widehat{W}_\alpha(x) = \frac{x^2}{(1+x^2)^\alpha}\,, \qquad \alpha \geq \tfrac{3}{2}\,, \tag{S.133}$$

whose ultraviolet behaviour is $\widehat{W}_\alpha \sim x^{2-2\alpha}$ as $x \to \infty$. The constraint $\alpha \geq 3/2$ ensures convergence, matching the theorem-level floor $\mathcal{S} \lesssim Cx^{-1}$ proved in Section D. Each value of α corresponds to a distinct assumption about turbulent enstrophy depth structure. At $\alpha = 3/2$ the enstrophy profile $\chi_q(z)$ is independent of q, corresponding to a local-equilibrium cascade with depth-independent spectral shape ($\chi_q \propto \varepsilon(z)^{2/3} \propto z^{-2/3}$, so q and z separate completely and UV suppression arises solely from the angular-cap geometry). At $\alpha = 2$ the profile acquires q-dependent depth confinement, $\chi_q(z) \propto e^{-qz}$, as expected when turbulence is injected at the surface by wave breaking and wind stress rather than locally by shear [39]. At $\alpha = 5/2$ the surface concentration is stronger still, as may arise, for example, from Langmuir circulations [10, 40].

Table S1: Scale-selection window comparison. Each row lists the ultraviolet behaviour, the physical assumption, the coupling constant $C_{\mathcal{S}}$, the fraction captured by the band $x \in [0.5, 2]$, and the peak of the spectral contribution density $x^{1/3}\widehat{W}(x)$.

Window	UV decay	Physical assumption	$C_{\mathcal{S}}$	$[k/2, 2k]$	x_{peak}
$\alpha = 3/2$ (floor)	x^{-1}	Local-equilibrium cascade; χ_q independent of q	1.40	35%	1.9
$\alpha = 2$ (baseline)	x^{-2}	Surface-injected turbulence; $\chi_q \propto e^{-qz}$	$\pi/6 \approx 0.52$	58%	1.2
$\alpha = 5/2$	x^{-3}	Strong surface concentration	0.31	66%	0.9
Top-hat $[\frac{1}{2}, 2]$	cutoff	Artificial (no UV tail)	1.40	-	~ 1

Analytical evaluation for $\alpha = 2$. The substitution $t = x^2$ converts the baseline integral to a Beta function,

$$C_{\mathcal{S}}^{(\alpha=2)} = \int_0^\infty \frac{x^{4/3}}{(1+x^2)^2}\,\mathrm{d}x = \frac{1}{2}\,B\left(\tfrac{7}{6},\,\tfrac{5}{6}\right). \tag{S.134}$$

With $a + b = 2$ and the reflection formula $\Gamma(z)\Gamma(1-z) = \pi/\sin(\pi z)$,

$$B\left(\tfrac{7}{6},\,\tfrac{5}{6}\right) = \tfrac{1}{6}\,\Gamma\left(\tfrac{1}{6}\right)\Gamma\left(\tfrac{5}{6}\right) = \frac{\pi}{3\sin(\pi/6)} = \frac{\pi}{3}\,, \tag{S.135}$$

giving the exact result

$$\boxed{C_{\mathcal{S}}^{(\alpha=2)} = \frac{\pi}{6} \approx 0.5236\,.} \tag{S.136}$$

Between $\alpha = 3/2$ (floor) and $\alpha = 2$ (baseline), $C_{\mathcal{S}}$ varies by a factor of 2.7. Between the two physically motivated shapes $\alpha = 2$ and $5/2$, it varies by only a factor of 1.7. The near-coincidence $C_{\mathcal{S}}^{(\alpha=3/2)} \approx C_{\mathcal{S}}^{(\text{top-hat})} = 1.40$ is accidental. The top-hat concentrates all weight inside $[k/2, 2k]$, while $\alpha = 3/2$ has a modest peak ($\widehat{W}(1) \approx 0.35$), but a fat UV tail-fully 65% of its integral comes from $x > 2$.

The theorem floor therefore overestimates the UV contribution by attributing full inertial-range vorticity to depths, where surface-injected turbulence has not penetrated.

The spectral contribution density $x^{1/3}\widehat{W}_\alpha(x)$ peaks at $x_{\rm peak} = \sqrt{7/(6\alpha-7)}$, confirming that the dominant coupling shifts toward $q \sim k$ as α increases. For the physically motivated choices ($\alpha \geq 2$), the band $x \in [0.5, 2]$ captures 58-66% of the integral (Fig. 2b of the main text), confirming that wave-scale eddies dominate the energy transfer.

C. The advective correlation factor C_τ

After angular averaging and factorisation of the geometric vertex, the damping rate contains the effective correlation time

$$\tau_{\rm eff}(q;k) \;\equiv\; \frac{C_\tau}{q\, c_g(k)}\,, \tag{S.137}$$

where $c_g(k)$ is the swell group velocity and C_τ is dimensionless and of order unity. Remote swell propagates at $c_g \sim$ 10-20 $\mathrm{m\,s^{-1}}$, far exceeding the turbulent velocity $u'(q) \sim$ 0.01-0.1 $\mathrm{m\,s^{-1}}$. The wave-energy trajectory traverses one spatial period of each turbulent Fourier mode long before the eddy turns over ($\tau_{\rm adv}/\tau_{\rm eddy} \sim 10^{-3}$-$10^{-2}$), so decorrelation is controlled by relative advection, that the wave-propagation analogue of Kraichnan-Tennekes random sweeping [44, 45]. The correlation function for wavenumber shell q is $C_{F,q}(t) \approx C_{F,q}(0)\,\mathcal{R}(q\,c_g\,t)$, where $\mathcal{R}(s)$ is a self-similar normalised spatial correlation with $\mathcal{R}(0) = 1$. Changing variables gives

$$\boxed{C_\tau \;=\; \int_0^\infty \mathcal{R}(s)\,\mathrm{d}s\,,} \tag{S.138}$$

which is necessarily of order unity. An exponential $\mathcal{R}(s) = \mathrm{e}^{-s}$ gives $C_\tau = 1$. A Gaussian e^{-s^2} gives $C_\tau = \sqrt{\pi}/2 \approx 0.89$. The broader Gaussian $\mathrm{e}^{-s^2/2}$ gives $C_\tau \approx 1.25$. The physical range is $C_\tau \in [0.89,\, 1.25]$, contributing $\sim$20% variation compared with the order-of-magnitude uncertainty in $\varepsilon_{\rm eff}$. We adopt $C_\tau = 1$ as the baseline. The full timescale comparison and spatial correlation functions are shown in Extended Data Fig. 2a,b.

D. The vertical-weighting factor C_E

The factor C_E relates the depth-integrated orbital kinetic energy to the modal energy per unit density,

$$C_E \;\equiv\; \frac{\displaystyle\int_{-\infty}^{0} |\boldsymbol{u}_\phi(z)|^2\,\mathrm{d}z}{E_k} \;=\; 1 \qquad \text{(deep water)}. \tag{S.139}$$

This is exact for $\boldsymbol{u}_\phi(z) \propto e^{kz}$ with $E_k = \frac{1}{2}ga^2$. For the far-field deep-water swell regime considered throughout this work, deviations from the ideal exponential eigenfunction are negligible.

E. Effective dissipation rate and numerical baseline

Collecting all prefactors (Eq. S.114), the baseline values $C_{\mathcal{S}} = \pi/6$, $C_\tau = 1$, $C_E = 1$, $\widetilde{G}_{\rm geom} = 2/3$ and $C_K = 1.5$ give

$$C_\Gamma = \frac{C_\tau\, C_K\, C_{\mathcal{S}}\, \widetilde{G}_{\rm geom}\, C_E}{2} \simeq 0.26, \qquad C_{\rm tot} = 8C_\Gamma = \frac{2\pi}{3} \simeq 2.09. \tag{S.140}$$

The effective dissipation rate entering the scaling law is the depth-weighted average of $\varepsilon(z)$ over the orbital layer. Equation (S.115) in Section S4 gives the formal definition over the full interaction layer. The operational form below restricts the lower limit to z_0 (the breaking-layer exclusion depth) and works in

the depth-downward convention used for dissipation profiles. With $z \geq 0$ measured downward from the surface (equivalent to the $z \leq 0$ convention of Sections S3-S4 under $z \to -z$),

$$\varepsilon_{\rm eff}(k) \;=\; \frac{\displaystyle\int_{z_0}^{H_{\rm ml}} \varepsilon(z)\, \mathrm{e}^{-2kz}\, \mathrm{d}z}{\displaystyle\int_{z_0}^{H_{\rm ml}} \mathrm{e}^{-2kz}\, \mathrm{d}z}, \tag{S.141}$$

where the kernel e^{-2kz} reflects the orbital-energy decay with e-folding depth $\delta_E = 1/(2k)$. For 14 s swell ($k \approx 0.021$ m^{-1}), $\delta_E \approx 24$ m. When $H_{\rm ml} \gg \delta_E$ and $2kz_0 \ll 1$,

$$\varepsilon_{\rm eff}(k) \;\approx\; 2k \int_{z_0}^{\infty} \varepsilon(z)\, \mathrm{e}^{-2kz}\, \mathrm{d}z \tag{S.142}$$

to within a few percent. Since $\varepsilon_{\rm eff} \propto u_*^{(w)3} \propto C_D^{3/2}$ and $\Gamma \propto \varepsilon_{\rm eff}^{2/3}$, the exponents cancel to give $\Gamma \propto C_D$. A fractional error in the drag coefficient translates one-to-one into Γ. Stress continuity across the air-sea interface gives

$$u_*^{(w)} = U_{10}\sqrt{C_D}\,\sqrt{\rho_a/\rho_w} \approx U_{10}\sqrt{C_D} \times 0.035, \tag{S.143}$$

with $\rho_a/\rho_w \approx 1.2 \times 10^{-3}$. We adopt the COARE 3.5 parameterisation [50] as the baseline. At $U_{10} = 10$ m s^{-1}, COARE 3.5 gives $C_D \approx 1.15 \times 10^{-3}$ and $u_*^{(w)} \approx 1.17 \times 10^{-2}$ m s^{-1}. Alternative bulk-flux formulations [51–53] give C_D from 1.08 to 1.47×10^{-3}, corresponding to $\Delta\Gamma/\Gamma$ between -6% and $+28\%$. For moderate winds ($5 \leq U_{10} \leq 20$ m s^{-1}), COARE 3.5 is well approximated by $C_D \approx (0.065\,U_{10} + 0.49) \times 10^{-3}$. Below the wave-breaking layer ($z > z_0$), the dissipation rate follows the law of the wall,

$$\varepsilon(z) = \frac{u_*^{(w)3}}{\kappa\, z}, \qquad z > z_0 = c_b\, H_{s,w}, \tag{S.144}$$

with $\kappa = 0.4$ and $c_b \approx 0.6$ ($z_0 \approx 0.9$ m for $H_s = 1.5$ m). Substituting into (S.142) gives

$$\varepsilon_{\rm eff}(k) = 2k\, \frac{u_*^{(w)3}}{\kappa}\, E_1(2k\, z_0), \tag{S.145}$$

where $E_1(x) = \int_x^\infty t^{-1}\mathrm{e}^{-t}\, \mathrm{d}t$. For 14 s swell with $z_0 = 0.9$ m, $2kz_0 \approx 0.037$ and $E_1(0.037) \approx 2.76$, giving

$$\boxed{\varepsilon_{\rm eff} \approx 2 \times 0.021 \times \frac{(1.17 \times 10^{-2})^3}{0.4} \times 2.76 \approx 4.6 \times 10^{-7}\ \mathrm{m^2\,s^{-3}}.} \tag{S.146}$$

The logarithmic approximation $E_1(x) \approx -\gamma_E - \ln x$ for $x \ll 1$ gives the closed form

$$\varepsilon_{\rm eff} \approx 2k\, \frac{u_*^{(w)3}}{\kappa}\, \big[-\gamma_E - \ln(2kz_0)\big], \tag{S.147}$$

with error less than 2% for $2kz_0 < 0.1$. The result is insensitive to z_0. A fourfold variation from 0.5 to 2.0 m changes $\varepsilon_{\rm eff}$ by a factor of ~ 1.7, following from the logarithmic dependence. The drag coefficient is typically the dominant source of uncertainty in large-scale applications.

Near-surface dissipation rates under active wind-wave breaking exceed the wall-law prediction by up to an order of magnitude. The Craig-Banner and Terray models [20, 21] parametrise the breaking-layer TKE flux as $F_0 = \alpha\, u_*^{(w)3}$ with $\alpha \sim$ 50-150, producing a three-layer vertical structure (Extended Data Fig. 3a). A constant-dissipation layer at $z < z_b \approx 0.6\, H_{s,w}$, a power-law decay layer $\varepsilon \propto z^{-\lambda}$ ($\lambda \approx$ 1.5-2) extending to $z_t \approx c_1\, H_{s,w}$, and an asymptotic return to wall-law scaling at greater depth [21, 54]. Here $H_{s,w}$ is the significant height of the *local wind-wave* field that generates the breaking. For $U_{10} = 10$ m s^{-1} the Pierson-Moskowitz limit gives $H_{s,w} \approx 2.2$ m, $z_b \approx 1.3$ m and $z_t \approx 9$ m (taking $c_1 \approx 4$ from the wave-following observations of Thomson et al. 54, Sutherland and Melville 55). The resulting surface enhancement is a factor ~ 7 relative to the wall-law.

The question is whether this enhancement should be included in $\varepsilon_{\rm eff}$. Within the present factorised closure, doing so would effectively double-count the spectral filtering already performed by the scale-selection integral $C_{\mathcal{S}}$. The full Green-Kubo damping coefficient is a coupled integral over eddy wavenumber q and depth z (Eq. S.148). The factored form $\Gamma \propto C_{\mathcal{S}}\,\varepsilon_{\rm eff}^{2/3}$ is valid when the depth-weighted dissipation entering $\varepsilon_{\rm eff}$ is produced by eddies at wavenumbers $q \sim k$ that receive full weight from the window $\widehat{W}(q/k)$. The wall-law profile, having no characteristic depth scale, satisfies this condition. The Kolmogorov inertial range at every depth feeds all wavenumbers q equally per unit log-interval, and the spectral integral $C_{\mathcal{S}}$ correctly selects the swell-scale contribution.

The breaking-generated eddies violate this condition. Their injection scales are set by the local wind-wave geometry, $\ell_b \sim O(H_{s,w}) \sim 2\,\mathrm{m}$, corresponding to $q_b \sim$ 1-6 rad m^{-1}. Relative to the swell wavenumber $k \sim 0.02$ rad m^{-1}, the ratio $q_b/k \sim$ 50-300 falls deep in the ultraviolet tail where $\widehat{W}(q_b/k) \sim 4\times10^{-4}$ (Extended Data Fig. 3b). The scale-selection integral has already assigned these eddies negligible weight. Including them a second time via a breaking-enhanced $\varepsilon_{\rm eff}$ would double-count their contribution. To bound the residual sensitivity we nevertheless apply the physical-space coupling filter $\mathcal{E}(\ell k) = (\ell k)^2/[1+(\ell k)^2]$ to both the wall-law and Terray profiles, integrate with the orbital weight e^{-2kz}, and take the ratio. The result ranges from 1.10× at $T = 12$ s to 1.02× at $T = 20$ s (Extended Data Fig. 3c)-a residual bias of at most 10%, far smaller than the $C_{\rm tot}$ uncertainty (×3). The wall-law baseline therefore provides the consistent baseline adopted here across the entire far-field swell band. The full three-panel analysis is presented in Extended Data Fig. 3.

F. Self-consistency of window shape and dissipation profile

The factored form $\Gamma = C_\Gamma\,\varepsilon_{\rm eff}^{2/3}\,k^{1/3}/|c_g|$ is exact only when the depth and spectral integrals factorise, which requires the normalised enstrophy profile $\chi_q(z)$ to be q-independent. When $\chi_q(z) \propto e^{-qz}$ (as in the real ocean), the full Green-Kubo structure involves a coupled integral

$$\Gamma \;\propto\; \int \mathrm{d}q\; q^{-2/3} \underbrace{\int \mathrm{d}z\; e^{-2kz}\;\varepsilon(z)^{2/3}\;\chi_q(z)}_{\mathcal{I}(k,q)}\,, \tag{S.148}$$

and $\mathcal{I}(k,q)$ cannot be cleanly separated into a q-independent depth factor and a spectral window. The current treatment assigns the depth-mismatch effect to the window ($\alpha = 2$) while computing $\varepsilon_{\rm eff}$ from the q-independent wall-law profile. Two approximation errors arise but partially compensate. First, by Jensen's inequality the linear depth-average $\langle\varepsilon\rangle^{2/3}$ overestimates the correct $\langle\varepsilon^{2/3}\rangle$ by a factor $\lesssim 1.2$ for the wall-law profile. Second, the physical premise of $\alpha = 2$ (surface-injected turbulence) implies near-surface ε exceeding the wall-law by a factor of ∼2-3 [40], which would increase $\varepsilon_{\rm eff}^{2/3}$ by ∼1.6, partially offsetting the window reduction from $C_{\mathcal{S}} = 1.40$ ($\alpha = 3/2$) to $\pi/6$ ($\alpha = 2$). The net effect places the baseline within a factor of ∼2 of the self-consistent Langmuir-enhanced alternative, and the $\omega^{8/3}$ exponent is unaffected. The wall-law baseline is conservative. It underestimates ε itself, and this dominates the Jensen overestimate, so our predictions represent a lower bound on the attenuation rate.

G. Validity of Kolmogorov scaling at swell-selected eddy scales

The $\omega^{8/3}$ scaling exponent requires Kolmogorov scaling $E_u(q) \propto \varepsilon^{2/3}\,q^{-5/3}$ only at eddy wavenumbers $q \sim k$, where the dissipation kernel peaks. The spectral contribution density $\mathrm{d}\Gamma/\mathrm{d}\ln q$ peaks near $q/k \approx 1$, where the eddy horizontal scale matches the orbital penetration depth and geometric overlap is maximised. The half-decade band $0.5 \le q/k \le 2$ captures the majority of the total attenuation rate (58-66% depending on window shape). For swell wavelengths $\lambda \approx$ 200-500 m, the selected eddy scales are $\ell_h \approx$ 30-80 m. What must be justified is not a universal $k^{-5/3}$ law for all mixed-layer motions at these scales, but the use of $E_u(q) \propto \varepsilon^{2/3}\,q^{-5/3}$ over the narrow swell-selected band $q \sim k$ that carries most of the Green-Kubo weight. For typical upper-ocean conditions ($\varepsilon \sim 10^{-8}$-10^{-7} m^2 s^{-3}, $N \sim 10^{-3}$ s^{-1}), the Ozmidov wavenumber $k_O = (N^3/\varepsilon)^{1/2} \approx$ 0.1-0.3 rad m^{-1}. The swell-selected wavenumbers $q \sim k \approx$ (1-3) $\times 10^{-2}$ rad m^{-1} fall

below k_O by roughly one decade. However, the *horizontal* energy spectrum maintains an approximately continuous $\varepsilon^{2/3}\,k_h^{-5/3}$ form across k_O, without evidence for an order-one break over the swell-selected band. The unified framework of Kunze [56] provides the theoretical basis. This spectral continuity is confirmed by towed ocean microstructure measurements [57], atmospheric data [58], and DNS of stratified turbulence [59, 60]. The orbital penetration depth $1/k \approx$ 30-80 m is comparable to or smaller than the mixed-layer depth, so the interaction occurs predominantly within the surface mixed layer, where the buoyancy frequency is $N_{\rm ml} \sim 10^{-4}$ s^{-1}. The local Ozmidov length scale is then $L_O = (\varepsilon/N_{\rm ml}^3)^{1/2} \approx 300$ m, exceeding the orbital penetration depth by a factor of 3-10. The swell-selected eddies therefore reside within the locally isotropic regime where the standard Kolmogorov spectrum applies without appeal to the Kunze framework. The turbulent Reynolds number

$$\mathrm{Re}_\ell \;\equiv\; \frac{\varepsilon^{1/3}}{\nu\, k^{4/3}} \tag{S.149}$$

is of order 10^6 for 14-s swell, confirming a well-developed inertial subrange at the relevant scales [38]. Within the mixed layer, local isotropy is assured. Below it, the horizontal spectrum maintains the same $\varepsilon^{2/3}\,k_h^{-5/3}$ form continuously across k_O.

H. Empirical closure accuracy on DNS turbulence

The closed-form law replaces the true vorticity spectrum by $E_\omega = C_K\varepsilon^{2/3}q^{1/3}$ inside the coupling kernel $\mathcal{W}(q/k)$. Because the analytical prediction depends on the turbulence field only through this kernel-weighted spectrum, the accuracy of the Kolmogorov closure within the selected window can be assessed on homogeneous isotropic turbulence (HIT) without introducing any wave. These tests do *not* validate the SVF mechanism itself, because the simulations contain no waves. They quantify only how accurately the Kolmogorov surrogate reproduces the actual vorticity spectrum within the kernel window that enters the analytical law. A separate companion study [**?**] validates the SVF mechanism directly by inserting a prescribed wave probe into turbulence and measuring the mode-projected Green-Kubo coefficient on the JHTDB `isotropic1024coarse` dataset ($\mathrm{Re}_\lambda \approx 433$, 5028 time steps).

Using 256^3, 512^3, and 1024^3 subvolumes from the JHTDB `isotropic8192` dataset (8192^3, $\mathrm{Re}_\lambda \approx$ 1300), we define

$$\beta(k) = \frac{\int E_\omega^{\rm DNS}(q)\,\mathcal{W}(q/k)\,q^{-1}\,\mathrm{d}q}{\int C_K\varepsilon^{2/3}q^{1/3}\,\mathcal{W}(q/k)\,q^{-1}\,\mathrm{d}q}\,. \tag{S.150}$$

This ratio measures the accuracy of the kernel-weighted Kolmogorov surrogate, including both residual departures of spectral shape and inertial-range normalisation from the ideal $q^{1/3}$ form. If the DNS spectrum were an exact Kolmogorov law with the standard C_K over the entire kernel support, β would equal unity identically.

The dissipation rate ε entering the denominator is estimated from the same subvolume velocity field via $\varepsilon = \int 2\nu q^2 E_u(q)\,\mathrm{d}q$. After the Helmholtz-Hodge projection defined below, the same estimator is recomputed on the projected solenoidal field, yielding $\varepsilon^{\rm sol}$. The numerator and denominator in Eq. (S.150) therefore use internally consistent statistics from the same subvolume.

Raw values ($\beta^{\rm raw} = 0.60$-0.69) are biased low by longitudinal spectral leakage introduced by the non-periodic subvolume FFT. On the full 8192^3 periodic domain, every Fourier mode satisfies $\boldsymbol{q}\cdot\hat{\boldsymbol{u}} = 0$. Cropping a finite subvolume breaks periodicity and generates a spurious longitudinal component. The Fourier-space identity

$$|\hat{\boldsymbol{\omega}}|^2 = q^2\,|\hat{\boldsymbol{u}}|^2 - |\boldsymbol{q}\cdot\hat{\boldsymbol{u}}|^2 \tag{S.151}$$

shows that the vorticity spectrum obtained from the exact spectral curl depends only on the solenoidal velocity. The numerator of β is therefore much less sensitive to this artifact, whereas the denominator uses ε inferred from the total velocity spectrum E_u, which is inflated by the spurious longitudinal contribution. This asymmetry accounts for most of the observed raw bias.

The parameter-free Helmholtz-Hodge projection

$$\hat{\boldsymbol{u}}^{\mathrm{sol}} = \hat{\boldsymbol{u}} - \frac{\boldsymbol{q}\,(\boldsymbol{q}\cdot\hat{\boldsymbol{u}})}{|\boldsymbol{q}|^2} \tag{S.152}$$

removes the spurious longitudinal component mode by mode and thereby strongly suppresses the dominant non-periodicity artifact at each resolution (Extended Data Fig. 4a, b, d). At 1024^3 the corrected ratio is

$$\beta^{\mathrm{sol}} = 0.96, \qquad C_{\mathrm{tot}}^{\mathrm{DNS}} = 2.01, \tag{S.153}$$

which is within 4% of the baseline $2\pi/3 = 2.09$ and well within the physically constrained range $[1.10,\ 3.34]$ (Eq. S.154).

The residual 4% gap reflects the finite-Reynolds-number non-uniformity of the compensated spectrum across the kernel window (Extended Data Fig. 4c). Under ideal HIT conditions, it therefore measures one specific component of the closure error: the finite-Re departure of the kernel-weighted spectrum from its asymptotic Kolmogorov form. Because oceanic Reynolds numbers are far larger than those accessible in present DNS, the same kernel window should lie more deeply within the inertial range in the ocean, so this particular source of error is expected to decrease. Other departures from ideal HIT–including anisotropy, stratification, and intermittency–are not probed by β and are discussed separately in Sections A and G.

I. Assembly of the total prefactor

Factor	Baseline	Physical range	Source
Numerical coefficient	4	-	deep-water dispersion
C_K	1.5	1.5-1.7	experiments/DNS
$\widetilde{G}_{\mathrm{geom}}$	2/3	2/3-3/4	Section A
$C_{\mathcal{S}}$	$\pi/6 \approx 0.52$	0.31-$\pi/6$	Section B
C_τ	1	0.89-1.25	Section C
C_E	1	1 (deep-water baseline)	Section D
C_{tot}	$\mathbf{2\pi/3 \approx 2.09}$	$\mathbf{[1.10,\ 3.34]}$	Eq. (S.116)

The standard value $C_K = 1.5$ [46] is adopted as the baseline. High-resolution DNS compilations report values up to 1.7 [61]. For circularly polarised deep-water waves with $R_u \sim$ 1-2, the geometric factor is $\widetilde{G}_{\mathrm{geom}} \in [2/3,\ 3/4]$. The coupling constant ranges from $C_{\mathcal{S}} = \pi/6$ (surface-injected turbulence, $\alpha = 2$) to 0.31 (strong surface concentration, $\alpha = 5/2$). The $\alpha = 3/2$ case ($C_{\mathcal{S}} = 1.40$) is retained in Section B as a theorem-level UV-convergence floor, not as the physical upper bound. For the far-field mixed layer the prefactor range is restricted to $\alpha \in [2,\ 5/2]$. Together with $C_\tau \in [0.89,\ 1.25]$ and $C_E = 1$,

$$C_{\mathrm{tot}}^{(\mathrm{phys})} \in \left[4\times 1.5\times\tfrac{2}{3}\times 0.31\times 0.89,\ \ 4\times 1.7\times\tfrac{3}{4}\times\tfrac{\pi}{6}\times 1.25\right] \approx [1.10,\ 3.34]\,. \tag{S.154}$$

The baseline value $C_{\mathrm{tot}} = 4\times 1.5\times(2/3)\times(\pi/6)\times 1\times 1 = 2\pi/3 \approx 2.09$ sits near the geometric mean of this range. The wider uncertainty compared with the geometric and correlation factors ($\widetilde{G}_{\mathrm{geom}}$ and C_τ together contribute < 30% variation) is dominated by the coupling constant $C_{\mathcal{S}}$, which reflects the physical ambiguity in the UV exponent α.

The distinction between the scaling exponent and the prefactor is central to the theory's predictive status. The $\omega^{8/3}$ exponent follows from the power-counting $-5/3 + 2 - 1 = -2/3$ and the deep-water dispersion relation alone. It is independent of the window shape α, the turbulent correlator, the depth profile of ε, and any $O(1)$ prefactor. The prefactor $C_{\mathrm{tot}} \in [1.10,\ 3.34]$ is a controlled parametrisation of the remaining geometric and environmental uncertainties, not a free parameter. Each factor is independently constrained by turbulence measurements, wave kinematics, or analytical integration. The residual prefactor uncertainty is dwarfed by the order-of-magnitude environmental variability in $\varepsilon_{\mathrm{eff}}$ along real propagation paths (Section E).

S6. Random-walk theory and intrinsic variance closure

Satellite retrievals return a finite-length attenuation estimator $\hat{\mu}_i$, not the ensemble-mean physical rate $\mu_E(\omega)$ defined by the Green-Kubo theory. For remote swell, the wave packet undergoes $N \sim 10^5$ weakly correlated multiplicative encounters with the turbulent bath along a trans-oceanic path. The resulting log-energy dynamics are therefore naturally described as a biased random walk. This section derives three structural results of that walk:

$$\boxed{\langle \hat{\mu} \rangle = 2\mu_E, \qquad \mathrm{Var}(\hat{\mu}) = \frac{2\mu_E}{L}\, c_0, \qquad c_0 = 1 \ \text{ for near-independent encounters.}} \tag{S.155}$$

The first factor of 2 is the Itô correction associated with multiplicative noise in energy space. The second factor of 2 is fixed by the same force autocorrelation that determines the mean drift through FDR-II. The ratio c_0 is therefore not an empirical fit at leading order, but a structural consequence of the encounter statistics. Weak along-ray dependence renormalises only the second moment, $c_0 \to \mathcal{R}$, without altering the first-moment prediction.

A. Random walk in logarithmic energy

Let $E_k(x)$ be the modal swell energy along a ray parameterised by distance x. The observable attenuation estimator is the finite-length log-energy slope

$$\hat{\mu} \equiv -\frac{1}{L} \ln \frac{E_k(L)}{E_k(0)}. \tag{S.156}$$

This is the natural variable because multiplicative energy changes become additive in $\ln E_k$. Under the narrow-band assumption A1, the observed swell energy satisfies $H_s^2 \propto E_\mathrm{w} \propto E_k$ up to a constant spectral-width factor, so the same log-slope estimator applies directly to the satellite-derived H_s. Partition the path into $N = L/\ell_\mathrm{corr}$ segments, where $\ell_\mathrm{corr} \sim c_g \tau_c$ is the advective decorrelation length of the mode-projected stochastic force along the ray. Define the logarithmic increment over one segment by

$$\Delta\varepsilon_n \equiv \ln \frac{E_n}{E_{n-1}}, \qquad \hat{\mu} = -\frac{1}{L} \sum_{n=1}^{N} \Delta\varepsilon_n. \tag{S.157}$$

Equivalently, introducing the fractional energy change per encounter,

$$\xi_n \equiv \frac{\Delta E_n}{E_{n-1}}, \tag{S.158}$$

the log increment is

$$\Delta\varepsilon_n = \ln(1 + \xi_n) = \xi_n - \frac{1}{2}\xi_n^2 + O(\xi_n^3). \tag{S.159}$$

In the weak-coupling regime $\delta = u'/c_g \ll 1$, each encounter is nearly symmetric with $\xi_n = O(\delta)$.

B. Mean and variance of one encounter

Over one advective encounter of duration $\tau_\mathrm{adv} = \ell_\mathrm{corr}/c_g$, the modal energy change induced by the stochastic vortex force is

$$\dot{W}_k(t) \equiv \left.\frac{\mathrm{d}E_k}{\mathrm{d}t}\right|_\mathrm{SVF} = \mathrm{Re}\big[a_k^* F_k(t)\big], \tag{S.160}$$

so that

$$\xi = \frac{1}{E_k} \int_0^{\tau_\mathrm{adv}} \dot{W}_k(t)\, \mathrm{d}t. \tag{S.161}$$

Here $F_k(t)$ is the mode-projected stochastic vortex force and $E_k = \frac{1}{2}|a_k|^2$. Define the force autocorrelation

$$C_F(\tau) \equiv \langle F_k(0) F_k^*(\tau) \rangle, \qquad I_F \equiv \int_0^\infty \mathrm{Re}\, C_F(\tau)\, \mathrm{d}\tau. \tag{S.162}$$

The power-transfer autocorrelation $\langle \dot{W}_k(0)\dot{W}_k(\tau)\rangle$ involves two terms via the identity $\mathrm{Re}(z_1)\mathrm{Re}(z_2) = \frac{1}{2}\mathrm{Re}(z_1 z_2^*) + \frac{1}{2}\mathrm{Re}(z_1 z_2)$ with $z_j = a_k^* F_k(t_j)$. The first term gives $\langle z_1 z_2^*\rangle = 2E_k\, C_F(\tau)$. The second requires evaluating the pseudo-correlation $\langle \eta_k(0)\eta_k(\tau)\rangle$, where $F_k = a_k\,\eta_k$ and η_k depends only on the bath. Because η_k is the Fourier coefficient at wavevector $\boldsymbol{k} \neq \boldsymbol{0}$ of a real, statistically homogeneous field, its pseudo-spectrum satisfies $\langle \hat{X}_{\boldsymbol{k}} \hat{X}_{\boldsymbol{k}'}\rangle \propto \delta(\boldsymbol{k} + \boldsymbol{k}')$. Setting $\boldsymbol{k}' = \boldsymbol{k} \neq \boldsymbol{0}$ gives $\delta(2\boldsymbol{k}) = 0$, so the pseudo-correlation vanishes identically. For a finite-bandwidth wave packet, the residual scales as $O(\Delta k/k) \ll 1$ (narrow-band assumption A1). The process η_k is therefore proper (circularly symmetric) to leading order, and

$$\langle \dot{W}_k(0)\dot{W}_k(\tau)\rangle = E_k\,\mathrm{Re}\,C_F(\tau). \tag{S.163}$$

This is the key bridge equation. The properness identity contributes $|a_k|^2 = 2E_k$ from $\langle z_1 z_2^*\rangle$, while the factor $\frac{1}{2}$ from the real-part identity gives the net coefficient E_k.

The force autocorrelation $\langle \dot{W}_k(0)\dot{W}_k(\tau)\rangle$ decays on the timescale $\tau_c \sim \tau_{\mathrm{adv}}$, so the single-encounter formulae below should be read as scale estimates. The results become asymptotically exact when the path is partitioned into mesoscale blocks of length $L_0 \gg \ell_{\mathrm{corr}}$, each containing many decorrelation lengths. Because both the mean and variance of the cumulative log-energy increment scale linearly with L_0/c_g, the ratio c_0 that governs the observable statistics is independent of this coarse-graining choice (see below Eq. S.173). The variance of the fractional change is therefore, at leading order,

$$\begin{aligned}
\mathrm{Var}(\xi) &= \frac{1}{E_k^2}\int_0^{\tau_{\mathrm{adv}}}\!\!\int_0^{\tau_{\mathrm{adv}}} \langle \dot{W}_k(t)\dot{W}_k(t')\rangle\,\mathrm{d}t\,\mathrm{d}t' \\
&\simeq \frac{2\tau_{\mathrm{adv}}}{E_k^2}\int_0^{\infty} \langle \dot{W}_k(0)\dot{W}_k(\tau)\rangle\,\mathrm{d}\tau \\
&= \frac{2\tau_{\mathrm{adv}}}{E_k}\,I_F.
\end{aligned} \tag{S.164}$$

The mean follows from the Markovian Green-Kubo decay law,

$$\frac{\mathrm{d}}{\mathrm{d}t}\langle E_k\rangle = -2\Gamma E_k, \qquad \Gamma = \frac{I_F}{2E_k}, \tag{S.165}$$

so over one encounter

$$\langle \xi\rangle = -2\Gamma\tau_{\mathrm{adv}}. \tag{S.166}$$

Substituting $I_F = 2E_k\Gamma$ into Eq. (S.164) gives

$$\boxed{\mathrm{Var}(\xi) = 4\Gamma\tau_{\mathrm{adv}}, \qquad \langle \xi\rangle = -2\Gamma\tau_{\mathrm{adv}}.} \tag{S.167}$$

The same force autocorrelation fixes both the mean drift and the fluctuation level. The variance is twice the magnitude of the mean fractional loss at leading order in δ. Passing from ξ to the log increment $\Delta\varepsilon = \ln(1+\xi)$ gives

$$\begin{aligned}
\langle \Delta\varepsilon\rangle &= \langle \xi\rangle - \frac{1}{2}\langle \xi^2\rangle + O(\delta^3) \\
&= -2\Gamma\tau_{\mathrm{adv}} - \frac{1}{2}\big(4\Gamma\tau_{\mathrm{adv}}\big) + O(\delta^3) \\
&= -4\Gamma\tau_{\mathrm{adv}} + O(\delta^3),
\end{aligned} \tag{S.168}$$

and

$$\mathrm{Var}(\Delta\varepsilon) = 4\Gamma\tau_{\mathrm{adv}} + O(\delta^3). \tag{S.169}$$

Half of the mean log-energy loss comes from the physical drift $-2\Gamma\tau_{\mathrm{adv}}$ and half from the noise-induced Itô correction.

C. Track-level mean, variance, and the baseline $c_0 = 1$

For near-independent encounters, summing Eq. (S.168) over $N = L/\ell_{\rm corr}$ segments gives

$$\langle\hat{\mu}\rangle = -\frac{N\,\langle\Delta\varepsilon\rangle}{L} = \frac{4\Gamma\tau_{\rm adv}}{\ell_{\rm corr}} = \frac{4\Gamma}{c_g} = 2\mu_E, \qquad \mu_E \equiv \frac{2\Gamma}{c_g}. \tag{S.170}$$

Similarly,

$$\mathrm{Var}(\hat{\mu}) = \frac{N\,\mathrm{Var}(\Delta\varepsilon)}{L^2} = \frac{4\Gamma\tau_{\rm adv}}{L\,\ell_{\rm corr}} = \frac{4\Gamma}{Lc_g} = \frac{2\mu_E}{L}. \tag{S.171}$$

Define the intrinsic noise-to-signal coefficient

$$c_0 \equiv \frac{\mathrm{Var}(\hat{\mu})}{\langle\hat{\mu}\rangle/L}. \tag{S.172}$$

Using Eqs. (S.170) and (S.171),

$$\boxed{c_0 = 1 \qquad \text{(near-independent encounters, leading order).}} \tag{S.173}$$

The identification of one step with $\ell_{\rm corr}$ is a coarse-graining convenience. For any mesoscale step of length $L_0 \gg c_g\tau_c$, both the mean and variance of the cumulative increment scale linearly with L_0/c_g, so the ratio $c_0 = \mathrm{Var}(\hat{\mu})\cdot L/\langle\hat{\mu}\rangle$ is independent of the step size. The result $c_0 = 1$ is a property of the force-autocorrelation shape, not of the chosen discretisation.

The baseline above applies to the two-endpoint estimator Eq. (S.156). If the attenuation rate is instead estimated from an OLS regression through M effectively independent points along the track, the intrinsic variance acquires the efficiency factor

$$\mathrm{Var}(\hat{\mu}_{\rm OLS} \mid \text{intrinsic}) = f(M)\,\frac{2\mu_E}{L}, \qquad f(M) = \frac{6}{5}\,\frac{M^2+1}{M(M+1)}. \tag{S.174}$$

Here $f(2) = f(3) = 1$ and $f(M) \to 6/5$ as $M \to \infty$. For the effective range $M \sim$ 3-15 relevant to satellite tracking, $f(M) \approx$ 1.00-1.13. This is a modest correction and does not alter the leading-order prediction $c_0 = O(1)$.

D. Variance renormalisation from along-ray dependence

The first-moment result $\langle\hat{\mu}\rangle = 2\mu_E$ depends only on the Green-Kubo integral and is unchanged by weak dependence between successive encounters. The second moment, by contrast, depends on the *shape* of the along-ray correlation function. Let $\Delta\varepsilon_n$ be the segment increments defined in Eq. (S.157), and define

$$\rho_m \equiv \frac{\mathrm{Cov}(\Delta\varepsilon_n, \Delta\varepsilon_{n+m})}{\mathrm{Var}(\Delta\varepsilon_n)}, \qquad m \geq 1. \tag{S.175}$$

Under short-memory mixing,

$$\mathrm{Var}(\hat{\mu}) = \frac{\mathrm{Var}(\Delta\varepsilon_n)}{L\,\ell_{\rm corr}}\left(1 + 2\sum_{m=1}^{\infty}\rho_m\right). \tag{S.176}$$

Define the renormalisation factor

$$\mathcal{R} \equiv 1 + 2\sum_{m=1}^{\infty}\rho_m. \tag{S.177}$$

Then the intrinsic variance becomes

$$\boxed{\mathrm{Var}(\hat{\mu}) = \frac{2\mu_E}{L}\,\mathcal{R}, \qquad c_0 = \mathcal{R}.} \tag{S.178}$$

Thus correlations renormalise the second moment only. A convenient continuum closure writes

$$\mathcal{R} \simeq \frac{1}{\ell_{\rm corr}} \int_{-\infty}^{\infty} R(r)\, \mathrm{d}r \equiv \frac{\ell_{\rm int}}{\ell_{\rm corr}}, \tag{S.179}$$

where $R(r)$ is the normalised along-ray correlation function of the projected increment process and $\ell_{\rm int}$ its integral correlation length. Hence c_0 measures the ratio of integral to local decorrelation length. The baseline $c_0 = 1$ corresponds to $\ell_{\rm int} \approx \ell_{\rm corr}$.

Our inferred negative-rate fractions are consistent with $c_0 = O(1)$ and suggest $c_0 \lesssim 1$, a modest variance reduction relative to the near-independent-encounter baseline. If c_0 lies below 1, along-ray encounter correlations provide a mechanism. The renormalisation $c_0 = \mathcal{R}$ with $\mathcal{R} < 1$ requires only that the along-ray correlation function develop sign changes, so that partial cancellation reduces $\ell_{\rm int}$ below $\ell_{\rm corr}$. This is plausible where Langmuir turbulence organises into counter-rotating vortical structures with alternating-sign contributions [10, 62]. At $c_0 \approx 0.78$ only a modest oscillatory component is required.

E. Signal-to-noise ratio and deterministic emergence scale

The intrinsic signal-to-noise ratio of a single-track estimate is

$$\mathcal{S}_{\rm int} \equiv \frac{\langle \hat{\mu} \rangle}{\sqrt{\mathrm{Var}_{\rm int}(\hat{\mu})}} = \sqrt{\frac{\langle \hat{\mu} \rangle L}{c_0}} = \sqrt{\frac{2\mu_E L}{c_0}}. \tag{S.180}$$

For $c_0 = 1$, this reduces to $\mathcal{S}_{\rm int} = \sqrt{2\mu_E L}$. Because $\mu_E \propto \omega^{8/3}$,

$$\mathcal{S}_{\rm int} \propto \omega^{4/3} \sqrt{L}, \tag{S.181}$$

so the frequency and path-length dependence of the negative tail provide two independent one-sided falsification tests of the theory. Setting $\mathcal{S}_{\rm int} = 1$ defines the deterministic emergence scale,

$$\boxed{L_{\rm det} = \frac{c_0}{\langle \hat{\mu} \rangle} = \frac{c_0}{2\mu_E}.} \tag{S.182}$$

This is the propagation distance at which the cumulative drift in $\ln E$ becomes comparable to the intrinsic scatter. It is an estimator-level detectability threshold, not the physical energy e-folding length μ_E^{-1}.

For deep-water swell of period $T = 15$ s ($k \approx 0.018$ rad m^{-1}, $c_g \approx 11.7$ m s^{-1}), a trans-oceanic path $L \sim 10^4$ km traverses $N \approx 1.7 \times 10^5$ near-independent encounters. Taking $\bar{\mu}_{\rm obs} = 0.8 \times 10^{-7}$ m^{-1} (corresponding to $\mu_E \approx 0.40 \times 10^{-7}$ m^{-1}) with $c_0 = 1$ gives $L_{\rm det} \approx 12{,}500$ km and $\mathcal{S}_{\rm int} \approx 0.89$. This places typical trans-oceanic swell in the marginal-detection regime ($\mathcal{S} \lesssim 1$), with a predicted negative fraction $P(\hat{\mu} < 0) = \Phi(-0.89) \approx 19\%$, consistent with 24% [34] and 13% [19]. Over the far-field wind range $U_{10} \approx$ 3-15 m s^{-1} ($\varepsilon_{\rm eff} \sim 10^{-8}$-$10^{-6}$ m^2 s^{-3}), the 15 s swell SNR rises from $\mathcal{S} \approx 0.4$ to ≈ 1.2 and the intrinsic negative fraction decreases from $\sim 34\%$ to $\sim 11\%$. At fixed turbulence and path length, the $\omega^{8/3}$ dependence gives $\mathcal{S} \propto \omega^{4/3}$, so 12 s swell has roughly double the SNR of 18 s swell. The $\mathcal{S} \sim O(1)$ regime is therefore a robust feature of the parameter space occupied by remote oceanic swell, not an artefact of any particular dataset. The full four-panel analysis is presented in Extended Data Fig. 5.

F. Predictive variance and the observable bridge

For a real satellite track, the total single-track variance contains three contributions:

$$\sigma_{\hat{\mu}}^2 = \underbrace{\frac{2\mu_E}{L} c_0}_{\text{intrinsic}} + \underbrace{\sigma_{\rm env}^2}_{\text{environmental}} + \underbrace{\sigma_{\rm obs}^2}_{\text{observational}}. \tag{S.183}$$

The intrinsic term is fixed by the SVF encounter statistics. The environmental term captures variability of $\varepsilon_{\rm eff}$ along propagation paths. The observational term collects altimetric noise, spectral partitioning uncertainty, and regression error [34].

For a representative trans-oceanic track with $\bar{\mu}_{\rm obs} = 0.8 \times 10^{-7}$ m^{-1} ($\mu_E \approx 0.40 \times 10^{-7}$ m^{-1}), $L = 10^7$ m, and $c_0 = 1$, the three contributions (in units of 10^{-7} m^{-1}) are $\sigma_{\rm int} \approx 0.89$, $\sigma_{\rm env} \approx 0.50$, and $\sigma_{\rm obs} \approx 0.63$, giving variance fractions of approximately 55%, 17%, and 28% respectively (Extended Data Fig. 9a). The predicted total $\sigma_{\rm tot} = \sqrt{0.89^2 + 0.50^2 + 0.63^2} \approx 1.2 \times 10^{-7}$ m^{-1} matches the observed spread [34] without tuning. The three components are estimated from independent information. The intrinsic component follows from the Green-Kubo kernel, the environmental component from reanalysis uncertainties, and the observational component from the altimeter error analysis.

Ensemble-averaging over M independent events reduces the intrinsic and observational contributions as $1/\sqrt{M}$, while the environmental floor remains fixed,

$$\sigma^2_{\bar{\mu}} \approx \frac{\sigma^2_{\rm int} + \sigma^2_{\rm obs}}{M} + \left[\sigma^{(\mu)}_{\rm env}\right]^2. \tag{S.184}$$

The crossover

$$M_\times \equiv \frac{\sigma^2_{\rm int} + \sigma^2_{\rm obs}}{\left[\sigma^{(\mu)}_{\rm env}\right]^2} \approx 5 \tag{S.185}$$

separates the random-scatter-limited regime ($M < M_\times$) from the environment-limited floor ($M > M_\times$). The altimeter dataset [34] ($M = 202$) is firmly environment-limited.

In the predictive likelihood used for the data analysis, the environmental and observational channels are combined into a single additive floor $\sigma^2_{\rm meas}$. Writing $\mu_{{\rm svf},i} = 2\mu_{E,i}$ for the observable SVF contribution and $\mu_{{\rm model},i} = \mu_{{\rm svf},i} + \mu^{\rm Dore}_{v,i}$ for the full trackwise mean, the working distribution is

$$\boxed{\hat{\mu}_i \sim \mathcal{N}\left(\mu_{{\rm model},i},\ c_0\,\frac{\mu_{{\rm svf},i}}{L_i} + \sigma^2_{\rm meas}\right).} \tag{S.186}$$

Only the SVF part enters the intrinsic variance because the Dore channel is deterministic. Likelihood-based estimation of β, c_0, and $\sigma_{\rm meas}$ is deferred to Section S7.

G. Negative attenuation rates as a discriminating prediction

For a Gaussian predictive distribution, the probability of a negative trackwise estimate is

$$P(\hat{\mu}_i < 0) = \Phi\left(-\mathcal{S}_{{\rm tot},i}\right), \qquad \mathcal{S}_{{\rm tot},i} = \frac{\mu_{{\rm model},i}}{\sqrt{c_0\,\mu_{{\rm svf},i}/L_i + \sigma^2_{\rm meas}}}, \tag{S.187}$$

where Φ is the standard normal CDF. The intrinsic part of this negative tail is unavoidable whenever $\mathcal{S}_{\rm int} = O(1)$, as is typical for trans-oceanic swell. This converts apparently anomalous negative estimates into a direct distribution-level prediction of the stochastic theory.

Two consequences are especially important. First, because $\mathcal{S}_{\rm int} \propto \omega^{4/3}$, longer-period swell should show a larger negative fraction than shorter-period swell at fixed path length and turbulence level. Taking $\bar{\mu}_{\rm obs} = 0.8 \times 10^{-7}$ m^{-1} at $T = 15$ s with $\mathcal{S}_{\rm int} \approx 0.89$ as a reference, $\mathcal{S}_{\rm int}(T) \propto T^{-4/3}$ gives $\mathcal{S}_{\rm int} \approx 1.04$ at $T = 12$ s and ≈ 0.57 at $T = 19$ s, corresponding to intrinsic negative fractions $\sim 15\%$ and $\sim 29\%$ respectively. Including observational noise, the total negative fraction rises from $\sim 17\%$ at $T = 12$ s to $\sim 33\%$ at $T = 19$ s, roughly a factor-of-two increase across the swell band. By contrast, observational methodology noise has no strong frequency dependence and would produce a nearly flat $P_{\rm neg}(T)$. Satellite data yield a frequency exponent $b = 3.07$ with 95% CI [2.11, 4.04] [34], and the theoretical $8/3 \approx 2.67$ lies within this interval.

Second, because $\mathcal{S}_{\rm int} \propto \sqrt{L}$, the negative fraction should decrease systematically with propagation distance. These two trends are more discriminating than the absolute mean attenuation rate because they test the distribution implied by the same Green-Kubo kernel that fixes the mean.

S7. Comparison with satellite observations

The scaling law and the track-level Gaussian predictive distribution derived in Section S6 (Eq. S.186) imply order-unity single-track scatter for basin-scale swell, so a non-negligible fraction of estimates should satisfy $\hat{\mu} < 0$. This section tests that prediction against two published satellite datasets, the 202-event altimeter-WW3 analysis [34] and the 10-year Envisat SAR analysis [19], and uses profile-likelihood inference and fixed-design Monte Carlo to calibrate the statistical framework.

Signal-to-noise ratios used in this section. Different observational products report different subsets of $\{\bar{\mu}_{\rm obs},\, \sigma_{\hat{\mu}},\, P_{\rm neg}\}$. To prevent ambiguity we distinguish three SNRs.

Intrinsic SNR (encounter noise only),

$$\mathcal{S}_{\rm int} \equiv \frac{\langle\hat{\mu}\rangle}{\sigma_{\rm int}} = \sqrt{\frac{\langle\hat{\mu}\rangle\, L_{\rm eff}}{c_0}} \approx \sqrt{\frac{\bar{\mu}_{\rm obs}\, L_{\rm eff}}{c_0}}\,. \tag{S.188}$$

Total SNR (when both sample mean and sample SD are reported),

$$\mathcal{S}_{\rm tot} \equiv \frac{\bar{\mu}_{\rm obs}}{\sigma_{\hat{\mu}}}\,. \tag{S.189}$$

Effective SNR (back-calculated from the negative fraction alone),

$$\mathcal{S}_{\rm eff} \equiv -\Phi^{-1}\big(P_{\rm neg,obs}\big). \tag{S.190}$$

The last supports only a consistency check on plausible SNR levels, not an independent test of the functional form $P(\hat{\mu} < 0) = \Phi(-\mathcal{S})$.

A. Profile-likelihood analysis

To test whether any global rescaling of the predicted mean is required, a multiplicative factor $\beta = C_{\rm tot}/(2\pi/3)$ is applied to the SVF component of both the mean and intrinsic variance (Eq. S.186). The same SVF contribution that sets the mean also sets the intrinsic variance through the S6 closure, so β enters both. The Green-Kubo prediction corresponds to $\beta = 1$. The negative log-likelihood over the 241-track sample is

$$\mathrm{NLL}(\beta, c_0, \sigma_{\rm meas}) = \tfrac{1}{2}\sum_{i=1}^{N}\left[\ln\sigma_i^2 + \frac{(\hat{\mu}_i - \beta\,\mu_{{\rm svf},i} - \mu_{v,i}^{\rm Dore})^2}{\sigma_i^2}\right], \tag{S.191}$$

with $\sigma_i^2 = c_0\,\beta\,\mu_{{\rm svf},i}/L_i + \sigma_{\rm meas}^2$.

At the adopted observational lower bound $\sigma_{\rm meas} = 0.63 \times 10^{-7}$ m^{-1}, the profile for c_0 (marginalised over β) gives $c_{0,\rm MLE} = 0.78$ with 95% CI [0.56, 1.16] (Extended Data Fig. 8a). The baseline $c_0 = 1$ lies within this interval, so the near-independent-encounter second-moment prediction is not rejected.

The corresponding profile for β gives $\beta_{\rm MLE} = 1.30$ with 95% CI [0.95, 1.64] (Extended Data Fig. 8b). The parameter-free prediction $\beta = 1$ falls within the statistical CI. The implied $C_{\rm tot} = 2\pi\beta/3 \approx 2.09$ remains within the theoretical range [1.10, 3.34]. The joint (β, c_0) contour places the baseline $(1, 1)$ inside the 95% region (Extended Data Fig. 8c), and $\beta_{\rm MLE}$ shifts toward unity as $\sigma_{\rm meas}$ increases (Extended Data Fig. 8d).

This estimate of c_0 is conditional on $\sigma_{\rm meas}$. Because c_0 and $\sigma_{\rm meas}$ are partially degenerate in the likelihood, they trade off along a ridge that preserves the total predictive variance (Extended Data Fig. 6a). A joint profile over both parameters at $\beta = 1$ yields $\sigma_{\rm meas} \approx 1.2 \times 10^{-7}$ m^{-1} with c_0 near zero. The adopted $\sigma_{\rm meas} = 0.63 \times 10^{-7}$ m^{-1} is a lower bound reflecting observational errors alone. The excess in the data-driven estimate is attributable to residual $\varepsilon_{\rm eff}$ prediction error. The reported $c_{0,\rm MLE} = 0.78$ therefore represents a conditional upper bound on the true intrinsic variance coefficient, since it absorbs non-intrinsic scatter not captured by $\sigma_{\rm meas}$. The first-moment prediction $\beta = 1$ is unaffected. It lies within the 95% CI regardless of how the variance budget is partitioned (Extended Data Fig. 6b,c).

B. Altimeter tracking dataset

A historical benchmark is the far-field altimeter-WW3 analysis [34], which contains 202 swell events with periods 12-18 s and wavelengths 250-500 m. The reported ensemble statistics are $\bar{\mu}_{\text{obs}} = 0.8 \times 10^{-7}\,\text{m}^{-1}$, $\sigma_{\hat{\mu}} = 1.2 \times 10^{-7}\,\text{m}^{-1}$, and 49/202 negative estimates (24.3%).

To set the physical scale, take a representative basin-scale path $L_{\text{eff}} = 10^7$ m with $c_0 = 1$. This is an illustrative estimate for a typical trans-oceanic event, not a trackwise reconstruction of the Jiang sample. The resulting intrinsic SNR is

$$\mathcal{S}_{\text{int}} = \sqrt{\frac{0.8 \times 10^{-7} \times 10^{7}}{1}} \approx 0.89, \tag{S.192}$$

placing typical basin-scale swell tracks in the marginal-detection regime. The intrinsic model predicts $P_{\text{neg}}^{(\text{int})} = \Phi(-0.89) \approx 19\%$, close to the observed 24.3% and slightly below, as expected when non-intrinsic variance contributions are included. From the reported sample mean and standard deviation, $\mathcal{S}_{\text{tot}} = 0.8/1.2 \approx 0.67$, giving $P(\hat{\mu} < 0) = \Phi(-0.67) \approx 25\%$, in close agreement with the observed 24.3%. The Jiang dataset therefore already exhibits the key qualitative signature of the theory. Broad, near-Gaussian single-track scatter with a substantial negative tail. The sharper frequency and path-length tests are carried out using the 241-track sample analysed in the main text.

C. SAR tracking dataset

A distinct satellite product is the 10-year Envisat SAR wave-mode analysis [19], which reports 1050 swell tracks from 460 storm events. Of these, 910 fitted dissipation rates are positive and 140 are negative. After imposing a 95% confidence criterion, the retained subset contains 606 positive and 21 negative cases. For the full sample, $P_{\text{neg,obs}} = 140/1050 \approx 0.133$, giving $\mathcal{S}_{\text{eff}} \approx 1.11$. For the 95% significant subset, $P_{\text{neg,obs}} = 21/627 \approx 0.034$, giving $\mathcal{S}_{\text{eff}} \approx 1.82$. The drop from 13.3% to 3.4% under stricter quality control is consistent with preferential removal of low-SNR tracks. These effective SNRs are back-calculated summary statistics (Eq. S.190) and support only a consistency check, not a full model test. The SAR dataset confirms the same broad picture. Order-unity pathwise scatter, a non-negligible negative tail before strict filtering, and strong sensitivity of that tail to data-quality thresholds.

D. Variance budget and the non-intrinsic noise floor

The observational methodology noise $\sigma_{\text{obs}} \approx 0.63 \times 10^{-7}\,\text{m}^{-1}$ is computed from four independent altimetric error sources identified in Jiang et al. [34] (their Section 3). H_s measurement precision (≈ 0.1), swell-partition approximation (≈ 0.3), fitting-method sensitivity (≈ 0.2), and point-source model deviation (≈ 0.5), all in units of $10^{-7}\,\text{m}^{-1}$, added in quadrature. This accounts for only $(\sigma_{\text{obs}}/\sigma_{\hat{\mu}})^2 = (0.63/1.20)^2 \approx 0.28$ of the observed variance. A purely deterministic single-track picture therefore leaves roughly 72% of the variance unexplained. In the present framework that missing variance is supplied by intrinsic wave-eddy encounter statistics. Using the leading-order baseline $c_0 = 1$ with $\bar{\mu}_{\text{obs}} = 0.8 \times 10^{-7}\,\text{m}^{-1}$ and $L_{\text{eff}} = 10^7$ m gives $\sigma_{\text{int}} \approx 0.89 \times 10^{-7}\,\text{m}^{-1}$. Including the propagated environmental contribution $\sigma_{\text{env}}^{(\mu)} \approx 0.50 \times 10^{-7}\,\text{m}^{-1}$ (Section S6 F) then gives $\sigma_{\text{tot}} \approx 1.20 \times 10^{-7}\,\text{m}^{-1}$, matching the observed value. The variance budget is approximately closed without any additional fit to the single-track scatter.

This comparison does not require $c_0 = 1$ exactly. In the theory $c_0 = 1$ is the leading-order reference, and weak along-ray dependence renormalises only the second moment (Section S6 D). The first-moment prediction $\beta = 1$ is unaffected. Two findings of the pipeline Monte Carlo study [63] acquire sharper interpretations here. The positive correlation between fitted $\hat{\mu}$ and initial wave height can arise algebraically from the shared regression and is not diagnostic of a distinct dissipation mechanism. When $\mathcal{S} = O(1)$, single-track fitting cannot discriminate functional forms. Functional-form inference must come from ensemble and distribution-level tests.

E. Fixed-design Monte Carlo validation of the inference layer

The profile-likelihood inference must itself be well calibrated. If the true coefficients were exactly $(\beta, c_0) = (1, 1)$, the pipeline should recover them without systematic bias. This question is distinct from the forward observational Monte Carlo of Jiang et al. [63], which quantifies how retrieval errors propagate into attenuation estimates. The present test addresses whether the heteroscedastic likelihood, the optimiser, and the profile confidence intervals are internally calibrated under the assumed model family. The deterministic laminar viscous correction (Dore term) is excluded from both generator and likelihood. The purpose is to validate the stochastic SVF inference layer, not every deterministic sub-component.

The generative model is

$$\hat{\mu}_i^{(r)} \;\sim\; \mathcal{N}\!\left(\beta^* \mu_{\mathrm{svf},i},\; c_0^* \beta^* \mu_{\mathrm{svf},i}\,/L_i + \sigma_{\mathrm{meas}}^{*2}\right), \tag{S.193}$$

with imposed truth $(\beta^*, c_0^*) = (1, 1)$. The real 241-track design matrix $(L_i,\ \mu_{\mathrm{svf},i})$ is held fixed. Only the observations are regenerated. For each synthetic dataset, the NLL (Eq. S.191) is minimised over $(\beta, c_0, \sigma_{\mathrm{meas}})$ by L-BFGS-B with a 27-point multi-start grid. Profile-likelihood 95% CIs are obtained by adaptive bisection. Three noise scenarios are tested. Baseline $\sigma_{\mathrm{meas}}^* = 0.63 \times 10^{-7}$ m^{-1}, low noise (0.30×10^{-7}), and high noise (1.00×10^{-7}). For each, $R = 2000$ independent replications are performed.

Table S2 summarises the results. In every scenario the bias is negligible. $|\mathrm{bias}(\hat{\beta})| < 0.003$ and $|\mathrm{bias}(\hat{c}_0)| < 0.02$. The 95% profile-likelihood coverage rates are 94.6-96.0% for β and 94.6-94.9% for c_0, consistent with the nominal level. The joint false-rejection rate is 3.8-5.4%, again consistent with the nominal 5%. The recovered $\hat{\beta}$ and $\hat{c}_0$ are negatively correlated ($\rho \approx -0.58$ to -0.75), reflecting the partial degeneracy between mean-scaling and variance-scaling roles of β. This correlation is visible in Extended Data Fig. 7d but does not compromise identifiability. Both marginal standard deviations remain moderate ($\mathrm{SD}(\hat{\beta}) \approx 0.14$-$0.17$, $\mathrm{SD}(\hat{c}_0) \approx 0.21$-$0.37$).

The recovery experiment shows that the inference machinery is unbiased and properly calibrated conditional on data drawn from the assumed model family. It does not, by itself, establish that real-ocean tracks obey that model. That external consistency comes from the independent evidence assembled in the main text. The frequency and environmental dependence of the ensemble-mean decay rate, the negative-rate fraction, and the residual structure (Figs. 3 and 4).

Table S2: Fixed-design Monte Carlo recovery ($R = 2000$, $(\beta^*, c_0^*) = (1, 1)$). Bias and standard deviation are computed over the R replications. Coverage is the fraction of replicates whose 95% profile-likelihood CI contains the true value. Joint rejection uses $\Delta\mathrm{NLL} > \frac{1}{2}\chi^2_{0.95}(3)$.

Scenario	σ_{meas}^* ($\times 10^{-7}$ m^{-1})	bias($\hat{\beta}$)	SD($\hat{\beta}$)	bias($\hat{c}_0$)	SD($\hat{c}_0$)	Cov. β (%)	Cov. c_0 (%)	Joint rej. (%)
Baseline	0.63	+0.003	0.15	+0.01	0.25	95.4	94.6	5.4
Low noise	0.30	−0.000	0.14	+0.01	0.21	94.6	94.9	3.8
High noise	1.00	+0.003	0.17	+0.02	0.37	96.0	94.9	4.4

F. Cross-dataset consistency

Table S3 collects the negative-rate fractions from three independent observational sources. For the altimeter samples the associated SNR estimates follow the forward model of the preceding subsections. For the SAR rows an effective SNR is inferred from the observed negative fraction for consistency mapping only (Eq. S.190). All three sources sit in the $\mathcal{S} = O(1)$ regime, confirming that the broad single-track scatter and its substantial negative tail are not artefacts of a single retrieval algorithm or observation platform. The differences in aggregate P_{neg} across datasets (26%, 24%, 13%) reflect differences in period and path-length distributions, environmental sampling, and measurement-noise characteristics rather than any inconsistency in the underlying physics.

Table S3: Observed and model-consistent negative-rate fractions. For the altimeter rows the SNR is derived from the forward model. Rows marked † report $\mathcal{S}_{\rm eff}$ inferred from $P_{\rm neg,obs}$ (Eq. S.190), so the listed $P_{\rm neg}^{\rm pred}$ matches the observation by construction.

Dataset	N	SNR used	$P_{\rm neg}^{\rm pred}$	$P_{\rm neg}^{\rm obs}$
Altimeter (this work)	241	$\mathcal{S}_{\rm tot} \approx 0.73$	23%	26%
Altimeter (historical, intrinsic)	202	$\mathcal{S}_{\rm int} \approx 0.89$	19%	24.3%
Altimeter (historical, total)	202	$\mathcal{S}_{\rm tot} \approx 0.67$	25%	24.3%
SAR (full sample)†	1050	$\mathcal{S}_{\rm eff} \approx 1.11$	13.3%	13.3%
SAR (95% significant)†	627	$\mathcal{S}_{\rm eff} \approx 1.82$	3.4%	3.4%

S8. Amplitude independence of the attenuation rate

The Green-Kubo theory predicts that μ_E is independent of wave amplitude within the far-field, non-breaking regime governed by Assumptions A1-A5. The coupling is linear in amplitude (A4, $F_k \propto a_k$), so the force autocorrelation factorises as $\langle F_k(0) F_k^*(t)\rangle = \langle |a_k|^2\rangle\, G_k(t)$, where G_k depends only on the bath statistics. The wave energy $E_k = \frac{1}{2}\langle |a_k|^2\rangle$ cancels identically in the Green-Kubo expression (Eq. S.46), making μ_E a material property of the turbulent bath at fixed k. This cancellation requires three ingredients. Linear coupling (A4) ensures that $|a_k|^2$ factors out. Statistical independence of the bath from swell energy (A5) prevents implicit E_k-dependence in G_k. Slow amplitude variation (A2) justifies treating a_k as quasi-constant over the correlation window $\tau \lesssim \tau_c$. All three hold with large margins for trans-oceanic swell (Section A, Remark 2).

This prediction stands in sharp contrast to the amplitude-dependent swell-dissipation parameterisation used in WAVEWATCH III [64–66]. In the current standard implementation [65], the swell source term is

$$S_{\rm swl}(k,\theta) = -\tfrac{2}{3}\, b_1\, \sigma \sqrt{B_n(k)}\; F(k,\theta), \qquad b_1 = \tfrac{1}{2}\, B_1\, H_s\, k_p\,, \tag{S.194}$$

where $F(k,\theta) = N(k,\theta)\,\sigma$ is the energy spectrum, N the action density, $B_n(k)$ the spectral saturation ($\propto N\sigma k^3$), and B_1 a tunable coefficient. Under a uniform amplitude scaling at fixed spectral shape, the three amplitude-dependent factors combine as $b_1 \propto H_s \propto \sqrt{N}$, $\sqrt{B_n} \propto \sqrt{N}$, $F \propto N$, giving $S_{\rm swl} \propto N^2$. The implied attenuation rate is therefore quadratic in amplitude,

$$\mu_{\rm emp}(k,\theta) \equiv -\frac{S_{\rm swl}(k,\theta)}{F(k,\theta)} \propto N \propto a^2 \propto H_s^2\,. \tag{S.195}$$

Over the range of initial wave heights in the altimeter dataset ($H_{s,0} = 1.3$-4.9 m) [34], this predicts a factor of $(4.9/1.3)^2 \approx 14$ variation in μ_E, readily detectable in 241 distinct swell tracks. Table S4 summarises the contrasting predictions.

Table S4: Predicted amplitude dependence: SVF theory versus the empirical parameterisation.

Property	SVF (this work)	Empirical
μ_E dependence on H_s	$\mu_E \propto H_s^0$	$\mu_E \propto H_s^2$
Predicted variation over $H_s = 1.3$-4.9 m	$\times 1$	$\times 14$
Observed H_s-$\hat{\mu}$ correlation (241 tracks)	$r = 0.00$	-
Frequency exponent	$\omega^{8/3}$	depends on B_n

We test the prediction using satellite tracks retained under the selection criteria ($250 \le \lambda \le 500$ m) [34]. A scatter plot of $\hat{\mu}$ versus $H_{s,0}$ for all 241 tracks yields $r = 0.00$ ($p = 0.98$), consistent with no association (Extended Data Fig. 1a). To control for the dominant frequency dependence $\mu_E \propto \omega^{8/3}$, we partition the data into three period bins (12.5-14 s, $n = 71$; 14-15.5 s, $n = 90$; 15.5-18 s, $n = 80$). Within each bin the correlation is statistically insignificant at the 1% level ($|r| \le 0.24$), with no consistent sign across bins.

The largest $R^2 \lesssim 0.06$ implies at most $\sim 6\%$ of the within-bin variability could be attributed to amplitude. This is far below what would be required for a quadratic-amplitude trend to emerge over the observed factor-of-3.8 amplitude range (Extended Data Fig. 1b).

A partial-correlation analysis in which the $\omega^{8/3}$-dependence is first regressed out confirms the null result. $r_{\text{partial}} = 0.07$ ($p = 0.27$) (Extended Data Fig. 1c). Quartile-binned means within each period group show no systematic trend (Extended Data Fig. 1d). The non-detection is particularly significant because the factor-of-3.8 dynamic range in $H_{s,0}$ would produce a factor-of-14 signal under the empirical parameterisation, well above the observational noise floor characterised in Section S7 (Eq. S.183).

Because μ_E does not depend on amplitude, the pathwise fluctuation in $\hat{\mu}$ is driven entirely by turbulent encounters and environmental variability, not by wave-height variations. The variance budget of Section S6 F is therefore cleanly separated from any amplitude effect.

S9. Domain of validity: why remote swell isolates the universal dissipation law

The theorem-level non-negativity result and the closed-form remote-swell law have distinct domains of validity. The Green-Kubo sign theorem $\Gamma(k) \geq 0$ (Theorem 1) requires Assumptions A1 (wave subspace), A3(i, iii) (stationarity, zero ensemble mean), A5(i) (local stationarity of the bath measure), and A6 (finite memory). The factorised closed-form law $\mu \propto \varepsilon_{\text{eff}}^{2/3}\, \omega^{8/3}$ and the amplitude-independence of the attenuation rate require the additional remote-swell conditions used in Sections S2-S4. These are quasi-frozen wave amplitude over the correlation window (A2), phase decoupling between swell and bath (A3(ii)), linear truncation in wave amplitude (A4), and approximate factorisation of the reference measure (A5(ii)).

Remote swell is the regime in which these extra conditions are most nearly satisfied. Wave breaking is rare, local wind input and nonlinear wave-wave transfer are comparatively weak, and the wave phase is predominantly set by distant forcing rather than by local mixed-layer dynamics. The SVF coupling is therefore not unique to remote swell. It operates whenever waves propagate through turbulence. What is special about remote swell is the signal-to-noise ratio. Competing processes are weak enough that the SVF contribution can be isolated observationally. In actively forced wind seas, local forcing correlates the wave field with the turbulent bath, the decoupling conditions deteriorate, and wave breaking dominates the energy budget by one to two orders of magnitude [67, 68].

The dominant energy sink for steep wind waves is breaking [66, 67]. For waves approaching a deep-water breaking threshold $ak \sim 0.3$ [66, 69], breaking attenuation can reach $\mu_{\text{brk}} \sim 10^{-5}$-$10^{-4}\,\text{m}^{-1}$, corresponding to e-folding distances of only 10-100 km. For gentle far-field swell with $ak \sim 0.01$-0.05, steepness is far below onset and breaking is strongly suppressed.

The phase-averaged Craik-Leibovich (CL) vortex force [6, 7] occupies a different status. In the leading-order mode-level theory of Sections S1-S2, the phase-averaged CL term carries spectral weight mainly at frequencies 0 and 2ω, rather than at the resolved swell frequency ω. It therefore does not contribute to the Green-Kubo friction coefficient in the present projected stochastic-force formulation.

It is nevertheless useful to estimate a distinct quasi-steady, signed wave-mean-flow exchange associated with Stokes-shear production [36]. Under the assumption that turbulent stresses are uncorrelated with the fast wave phase, the depth-integrated production scales as

$$\int_{-\infty}^{0} P_{ws}\, \mathrm{d}z \;\sim\; \rho_w\, u_*^{(w)2}\, U_s(0)\, \cos\Delta\theta\,, \tag{S.196}$$

where $\Delta\theta$ is the angle between swell propagation and local wind. Converting to a spatial attenuation-like rate gives

$$\mu_{\text{CL}}^{(\text{qs})} \;\sim\; \frac{4\, u_*^{(w)2}\, k^2}{g}\, \cos\Delta\theta\,. \tag{S.197}$$

This quantity should not be conflated with the positive-definite coefficient μ_{SVF}. It is a slow, deterministic modulation whose sign is set by local wind alignment. For $U_{10} = 10\ \text{m s}^{-1}$ and $k \approx 0.02\,\text{m}^{-1}$, the water-side friction velocity is $u_*^{(w)} \approx 1.2 \times 10^{-2}\ \text{m s}^{-1}$ and $|\mu_{\text{CL}}^{(\text{qs})}| \sim 2 \times 10^{-8}\,\text{m}^{-1}$, comparable to or

Table S5: Representative wave-energy exchange channels. Internal oceanic non-breaking channels are listed together with breaking and laminar benchmarks. External atmospheric input (Miles-type wind forcing) and conservative four-wave spectral redistribution are excluded by the remote-swell regime conditions.

Channel	Ampl. dep.	Freq. dep.	Active regime	Sign	Typical μ (m^{-1})
Breaking	threshold	empirical	Steep wind sea	> 0	10^{-5}-10^{-4}
Laminar viscosity (Dore)[a]	none	$\omega^{7/2}$	All, usually subdominant	> 0	3×10^{-9}-3×10^{-8}
CL/Langmuir	$\propto$ Stokes drift	model-dep.	Wind sea and swell	$\pm$	$\sim 10^{-8}$
SVF (Green-Kubo)	none	$\omega^{8/3}$	Non-breaking waves (cleanest in remote swell)	> 0	0.5-1×10^{-7}

[a] Laminar (Stokes) solution [70, 71]. Even if the air-side boundary layer becomes turbulent, available estimates place the enhancement well below observed mean attenuation [18].

smaller than μ_{SVF}. For remote swell the angle $\Delta\theta$ varies broadly along a trans-oceanic path, so the path-mean CL contribution is typically small owing to sign cancellations.

For representative far-field conditions ($T \approx 14$ s, $\varepsilon_{\mathrm{eff}} \sim 5\times10^{-7}$ m^2 s^{-3}), the SVF law gives $\mu_{\mathrm{SVF}} \sim 0.5$-$1\times10^{-7}$ m^{-1}. The SVF channel is amplitude-independent (Section S8), not signed by wind-swell alignment, and positive-definite by Theorem 1. We therefore regard remote swell as the regime in which breaking is suppressed and the CL modulation is sufficiently small that the SVF friction can be isolated and tested.

The classical upper limit for laminar air-side viscous shearing [70, 71] gives $\mu_\nu \sim (3\text{-}5)\times10^{-9}$ m^{-1} for 14-18 s swell, an order of magnitude below the SVF prediction. Because $\mu_\nu \propto \omega^{7/2}$ decays faster with period than $\mu_E \propto \omega^{8/3}$, the laminar channel is subdominant throughout the remote-swell band. Even if the air-side boundary layer becomes turbulent, available estimates place the enhancement well below observed mean attenuation [18, 71].

We distinguish here between the physical attenuation rate μ_E and the satellite estimator $\hat{\mu}$ derived from finite-length log-energy regressions (Section S6). Observed literature values are typically reported for $\hat{\mu}$, whose mean satisfies the Itô relation $\langle\hat{\mu}\rangle = 2\mu_E$ to leading order. Reported values $\hat{\mu} \sim 1\text{-}1.5\times10^{-7}$ m^{-1} correspond to physical rates $\mu_E \sim 0.5\text{-}0.75\times10^{-7}$ m^{-1}, consistent with the SVF range. That the observed mean exceeds the Dore laminar ceiling by a factor of several was the original motivation for invoking turbulent mechanisms [18]. The SVF theory supplies a parameter-free, first-principles account of that turbulent excess. Table S5 summarises the channel comparison.

Beyond remote swell. The closed-form scaling $\mu \propto \varepsilon_{\mathrm{eff}}^{2/3}\,\omega^{8/3}$ rests on four ingredients. An inertial-range vorticity spectrum $E_\omega \propto q^{1/3}$, the geometric overlap kernel $\mathcal{W}(q/k)$, a sweep decorrelation time $\tau \propto (qc_g)^{-1}$, and the deep-water dispersion relation $k = \omega^2/g$. None is specific to remote swell. The $\omega^{8/3}$ dependence is the natural dimensional signature of the SVF channel whenever these conditions are approximately met.

What distinguishes remote swell is the clarity with which the SVF channel can be isolated. In actively forced wind seas, three additional processes can mask the SVF contribution.

1. *Wave breaking.* Breaking losses ($\mu_{\mathrm{brk}} \sim 10^{-4}$-$10^{-3}$ m^{-1}) can exceed the SVF prediction by one to two orders of magnitude.

2. *Wind input.* Active atmospheric forcing injects energy at rates comparable to breaking losses, so the observed net tendency need not reveal the weaker SVF sink.

3. *CL-type inter-modal coupling.* At leading order for nearly monochromatic swell, the CL force carries spectral support only at 0 and 2ω and does not project onto the swell mode. In a broadband wind sea, however, difference-frequency interactions between distinct components can generate forcing

near $|\omega_i - \omega_j|$ that overlaps other spectral components. The CL pathway may then participate in inter-modal energy transfer into Langmuir circulations and eventually into the turbulent cascade.

Remote swell is the cleanest observational regime because competing pathways are suppressed. Breaking is weak, wind input is negligible, and the near-monochromatic structure minimises CL-type inter-modal coupling. Quantifying the relative importance of these channels in broadband wind seas is a natural target for future wave-resolving DNS and LES studies.

SVF as an irreducible non-breaking sink. Because $\Gamma(k) \geq 0$, the SVF contribution defines an irreducible positive sink component wherever the reduced-kernel assumptions hold. Other pathways may redistribute energy between spectral components, but the SVF channel itself remains strictly dissipative and cannot be cancelled into a gain term. One broader implication is worth noting. The empirical non-breaking dissipation coefficients in operational wave models ($f_e \sim 0.002$-0.004 in WAVEWATCH III [64, 72]) correspond under typical remote-swell conditions to $\mu \sim 10^{-7}\,\mathrm{m}^{-1}$, consistent with the SVF prediction. Part of their tuned role may have been compensating for the missing SVF pathway.

References

[1] G. K. Batchelor. *An Introduction to Fluid Dynamics*. Cambridge University Press, 1967.

[2] Anqing Xuan, Bing-Qing Deng, and Lian Shen. Effect of an incoming Gaussian wave packet on underlying turbulence. *J. Fluid Mech.*, 999:A45, 2024.

[3] O. M. Phillips. *The Dynamics of the Upper Ocean*. Cambridge University Press, 2nd edition, 1977.

[4] J. Lighthill. *Waves in Fluids*. Cambridge University Press, 1978.

[5] C. C. Mei, M. Stiassnie, and D. K.-P. Yue. *Theory and Applications of Ocean Surface Waves*. World Scientific, 2005.

[6] J. C. McWilliams. *Quasi-linear Theory for Surface Wave–Current Interactions*. Springer, 2022.

[7] A. D. D. Craik and S. Leibovich. A rational model for Langmuir circulations. *J. Fluid Mech.*, 73: 401–426, 1976.

[8] S. Leibovich. *On wave-current interaction theories of Langmuir circulations*, volume 99. 1980.

[9] D. D. Holm. The ideal Craik–Leibovich equations. *Physica D*, 98:415–441, 1996.

[10] J. C. McWilliams, P. P. Sullivan, and C.-H. Moeng. Langmuir turbulence in the ocean. *J. Fluid Mech.*, 334:1–30, 1997.

[11] P. P. Sullivan, J. C. McWilliams, and W. K. Melville. Surface gravity wave effects in the oceanic boundary layer: Large-eddy simulation with vortex force and stochastic breakers. *J. Fluid Mech.*, 593:405–452, 2007.

[12] P. P. Sullivan and J. C. McWilliams. Dynamics of winds and currents coupled to surface waves. *Annu. Rev. Fluid Mech.*, 42:19–42, 2010.

[13] Yasushi Fujiwara, Yutaka Yoshikawa, and Yoshimasa Matsumura. A wave-resolving simulation of Langmuir circulations with a nonhydrostatic free-surface model: Comparison with Craik–Leibovich theory and an alternative Eulerian view of the driving mechanism. *J. Phys. Oceanogr.*, 48:1691–1708, 2018.

[14] M. S. Green. Markoff random processes and the statistical mechanics of time-dependent phenomena. II. Irreversible processes in fluids. *J. Chem. Phys.*, 22(3):398–413, 1954.

[15] R. Kubo. Statistical-mechanical theory of irreversible processes. I. General theory and simple applications to magnetic and conduction problems. *J. Phys. Soc. Jpn.*, 12(6):570–586, 1957.

[16] S. Bochner. *Vorlesungen über Fouriersche Integrale*. Akademische Verlagsgesellschaft, Leipzig, 1933.

[17] F. E. Snodgrass, G. W. Groves, K. F. Hasselmann, G. R. Miller, W. H. Munk, and W. H. Powers. Propagation of ocean swell across the Pacific. *Phil. Trans. R. Soc. Lond. A*, 259:431–497, 1966.

[18] F. Ardhuin, B. Chapron, and F. Collard. Observation of swell dissipation across oceans. *Geophys. Res. Lett.*, 36:L06607, 2009. doi: 10.1029/2008GL037030.

[19] Justin E. Stopa, Fabrice Ardhuin, Romain Husson, Haoyu Jiang, Bertrand Chapron, and Fabrice Collard. Swell dissipation from 10 years of Envisat advanced synthetic aperture radar in wave mode. *Geophys. Res. Lett.*, 43:3423–3430, 2016. doi: 10.1002/2015GL067566.

[20] Peter D. Craig and Michael L. Banner. Modeling wave-enhanced turbulence in the ocean surface layer. *J. Phys. Oceanogr.*, 24(12):2546–2559, 1994. doi: 10.1175/1520-0485(1994)024<2546:MWETIT>2.0.CO;2.

[21] E. A. Terray, M. A. Donelan, Y. C. Agrawal, W. M. Drennan, K. K. Kahma, III A. J. Williams, P. A. Hwang, and S. A. Kitaigorodskii. Estimates of kinetic energy dissipation under breaking waves. *J. Phys. Oceanogr.*, 26(5):792–807, 1996. doi: 10.1175/1520-0485(1996)026<0792:EOKEDU>2.0.CO;2.

[22] Stephen E. Belcher, Alan L. M. Grant, Kirsty E. Hanley, Baylor Fox-Kemper, Luke Van Roekel, Peter P. Sullivan, William G. Large, Andy Brown, Adrian Hines, Daley Calvert, Anna Rutgersson, Heidi Pettersson, Jean-Raymond Bidlot, Peter A. E. M. Janssen, and Jeff A. Polton. A global perspective on Langmuir turbulence in the ocean surface boundary layer. *Geophys. Res. Lett.*, 39 (18):L18605, 2012. doi: 10.1029/2012GL052932.

[23] B. J. Alder and T. E. Wainwright. Decay of the velocity autocorrelation function. *Physical Review A*, 1(1):18–21, 1970. doi: 10.1103/PhysRevA.1.18.

[24] Adrean Webb and Baylor Fox-Kemper. Wave spectral moments and Stokes drift estimation. *Ocean*

Modelling, 40:273–288, 2011. doi: 10.1016/j.ocemod.2011.08.007.
[25] H. Mori. Transport, collective motion, and Brownian motion. *Prog. Theor. Phys.*, 33:423–455, 1965.
[26] R. Zwanzig. *Nonequilibrium Statistical Mechanics*. Oxford University Press, 2001.
[27] Denis J. Evans and Gary P. Morriss. *Statistical Mechanics of Nonequilibrium Liquids*. Cambridge University Press, Cambridge, 2nd edition, 2008. doi: 10.1017/CBO9780511535307.
[28] Umberto Marini Bettolo Marconi, Andrea Puglisi, Lamberto Rondoni, and Angelo Vulpiani. Fluctuation–dissipation: Response theory in statistical physics. *Physics Reports*, 461(4–6):111–195, 2008. doi: 10.1016/j.physrep.2008.02.002.
[29] Ming Han, Michel Fruchart, Colin Scheibner, Suriyanarayanan Vaikuntanathan, Juan J. de Pablo, and Vincenzo Vitelli. Fluctuating hydrodynamics of chiral active fluids. *Nature Physics*, 17:1260–1269, 2021. doi: 10.1038/s41567-021-01360-7.
[30] É. Fodor, C. Nardini, M. E. Cates, J. Tailleur, P. Visco, and F. van Wijland. How far from equilibrium is active matter? *Phys. Rev. Lett.*, 117:038103, 2016.
[31] Jean-Pierre Hansen and Ian R. McDonald. *Theory of Simple Liquids: With Applications to Soft Matter*. Academic Press, Oxford, 4th edition, 2013. ISBN 978-0-12-387032-2. doi: 10.1016/C2010-0-66723-X.
[32] A. N. Kolmogorov. The local structure of turbulence in incompressible viscous fluid for very large Reynolds numbers. *Dokl. Akad. Nauk SSSR*, 30:301–304, 1941.
[33] James R. Holton and Gregory J. Hakim. *An Introduction to Dynamic Meteorology*, volume 88 of *International Geophysics Series*. Academic Press, Amsterdam, 5th edition, 2013. ISBN 978-0-12-384866-6.
[34] H. Jiang, J. E. Stopa, H. Wang, R. Husson, A. Mouche, B. Chapron, and G. Chen. Tracking the attenuation and nonbreaking dissipation of swells using altimeters. *J. Geophys. Res. Oceans*, 121:1446–1458, 2016.
[35] Mickaël D. Chekroun, Honghu Liu, and James C. McWilliams. Stochastic rectification of fast oscillations on slow manifold closures. *Proc. Natl. Acad. Sci. U.S.A.*, 118(48):e2113650118, 2021. doi: 10.1073/pnas.2113650118.
[36] F. Ardhuin and A. D. Jenkins. On the interaction of surface gravity waves and upper ocean turbulence. *J. Phys. Oceanogr.*, 36:551–557, 2006.
[37] G. K. Batchelor. *The Theory of Homogeneous Turbulence*. Cambridge University Press, Cambridge, 1953.
[38] S. B. Pope. *Turbulent Flows*. Cambridge University Press, 2000.
[39] Ayal Anis and James N. Moum. Surface wave–turbulence interactions: Scaling $\varepsilon(z)$ near the sea surface. *J. Phys. Oceanogr.*, 25:2025–2045, 1995. doi: 10.1175/1520-0485(1995)025<2025:SWISNT>2.0.CO;2.
[40] Zhihua Zheng, Ramsey L. Harcourt, and Eric A. D'Asaro. Evaluating Langmuir turbulence parameterizations in the ocean surface boundary layer. *J. Geophys. Res. Oceans*, 126:e2020JC016325, 2021. doi: 10.1029/2020JC016325.
[41] F. P. Bretherton and C. J. R. Garrett. Wavetrains in inhomogeneous moving media. *Proc. R. Soc. Lond. A*, 302:529–554, 1968. doi: 10.1098/rspa.1968.0034.
[42] M. A. C. Teixeira and S. E. Belcher. On the distortion of turbulence by a progressive surface wave. *J. Fluid Mech.*, 458:229–267, 2002.
[43] H. Tennekes and J. L. Lumley. *A First Course in Turbulence*. MIT Press, Cambridge, MA, 1972.
[44] H. Tennekes. Eulerian and Lagrangian time microscales in isotropic turbulence. *J. Fluid Mech.*, 67:561–567, 1975.
[45] R. H. Kraichnan. Kolmogorov's hypotheses and Eulerian turbulence theory. *Phys. Fluids*, 7:1723–1734, 1964.
[46] K. R. Sreenivasan. On the universality of the Kolmogorov constant. *Phys. Fluids*, 7:2778–2784, 1995.
[47] E. A. D'Asaro. Turbulent vertical kinetic energy in the ocean mixed layer. *J. Phys. Oceanogr.*, 31:3530–3537, 2001.

[48] S. A. Thorpe. Langmuir circulation. *Annu. Rev. Fluid Mech.*, 36:55–79, 2004.
[49] K. R. Sreenivasan and R. A. Antonia. The phenomenology of small-scale turbulence. *Annu. Rev. Fluid Mech.*, 29:435–472, 1997.
[50] J. B. Edson et al. On the exchange of momentum over the open ocean. *J. Phys. Oceanogr.*, 43: 1589–1610, 2013.
[51] W. G. Large and S. Pond. Open ocean momentum flux measurements in moderate to strong winds. *J. Phys. Oceanogr.*, 11:324–336, 1981. doi: 10.1175/1520-0485(1981)011<0324:OOMFMI>2.0.CO;2.
[52] S. D. Smith. Wind stress and heat flux over the ocean in gale force winds. *J. Phys. Oceanogr.*, 10: 709–726, 1980. doi: 10.1175/1520-0485(1980)010<0709:WSAHFO>2.0.CO;2.
[53] J. Wu. Wind-stress coefficients over sea surface from breeze to hurricane. *J. Geophys. Res.*, 87(C12): 9704–9706, 1982. doi: 10.1029/JC087iC12p09704.
[54] J. Thomson, M. S. Schwendeman, S. F. Zippel, S. Moghimi, J. Gemmrich, and W. E. Rogers. Wave-breaking turbulence in the ocean surface layer. *J. Phys. Oceanogr.*, 46:1857–1870, 2016. doi: 10.1175/JPO-D-15-0130.1.
[55] P. Sutherland and W. K. Melville. Field measurements of surface and near-surface turbulence in the presence of breaking waves. *J. Phys. Oceanogr.*, 45:943–965, 2015. doi: 10.1175/JPO-D-14-0133.1.
[56] E. Kunze. A unified model spectrum for anisotropic stratified and isotropic turbulence in the ocean and atmosphere. *J. Phys. Oceanogr.*, 49:385–407, 2019.
[57] J. M. Klymak and J. N. Moum. Oceanic isopycnal slope spectra. Part II: Turbulence. *J. Phys. Oceanogr.*, 37:1232–1245, 2007.
[58] G. D. Nastrom and K. S. Gage. A climatology of atmospheric wavenumber spectra of wind and temperature observed by commercial aircraft. *J. Atmos. Sci.*, 42:950–960, 1985.
[59] E. Lindborg. The energy cascade in a strongly stratified fluid. *J. Fluid Mech.*, 550:207–242, 2006.
[60] G. Brethouwer, P. Billant, E. Lindborg, and J.-M. Chomaz. Scaling analysis and simulation of strongly stratified turbulent flows. *J. Fluid Mech.*, 585:343–368, 2007.
[61] T. Ishihara, T. Gotoh, and Y. Kaneda. Study of high-Reynolds number isotropic turbulence by direct numerical simulation. *Annu. Rev. Fluid Mech.*, 41:165–180, 2009.
[62] S. A. Thorpe. Langmuir circulation. *Annual Review of Fluid Mechanics*, 36:55–79, 2004. doi: 10.1146/annurev.fluid.36.052203.071431.
[63] H. Jiang, A. Mouche, H. Wang, A. Babanin, B. Chapron, and G. Chen. Limitation of the altimeter-derived swell attenuation: An example of swell propagation from the Southern Ocean. *Remote Sens. Environ.*, 200:244–253, 2017. doi: 10.1016/j.rse.2017.08.004.
[64] S. Zieger, A. V. Babanin, W. E. Rogers, and I. R. Young. Observation-based source terms in the third-generation wave model WAVEWATCH. *Ocean Model.*, 96:2–25, 2015.
[65] Qingxiang Liu, W. Erick Rogers, Alexander V. Babanin, Ian R. Young, Leonel Romero, Stefan Zieger, Fangli Qiao, and Changlong Guan. Observation-based source terms in the third-generation wave model WAVEWATCH III: Updates and verification. *J. Phys. Oceanogr.*, 49:489–517, 2019. doi: 10.1175/JPO-D-18-0137.1.
[66] Alexander V. Babanin. *Breaking and Dissipation of Ocean Surface Waves*. Cambridge University Press, 2011. doi: 10.1017/CBO9780511736162.
[67] W. K. Melville. The role of surface-wave breaking in air–sea interaction. *Annu. Rev. Fluid Mech.*, 28:279–321, 1996.
[68] O. M. Phillips. Spectral and statistical properties of the equilibrium range in wind-generated gravity waves. *J. Fluid Mech.*, 156:505–531, 1985.
[69] O. M. Phillips. The equilibrium range in the spectrum of wind-generated waves. *J. Fluid Mech.*, 4 (4):426–434, 1958. doi: 10.1017/S0022112058000550.
[70] B. D. Dore. Some effects of the air-water interface on gravity waves. *Geophysical & Astrophysical Fluid Dynamics*, 10(1):215–230, 1978. doi: 10.1080/03091927808242638.
[71] F. Collard, F. Ardhuin, and B. Chapron. Monitoring and analysis of ocean swell fields from space: New methods for routine observations. *J. Geophys. Res.*, 114:C07023, 2009. doi: 10.1029/2008JC005215.
[72] F. Ardhuin, N. Rascle, K. Belibassakis, D. Katsanis, D. Wang, R. Magne, and M. Accensi.

Semiempirical dissipation source functions for ocean waves. Part I: Definition, calibration and validation. *J. Phys. Oceanogr.*, 40:1917–1941, 2010.

Caption for Movie S1. Swell decay as a Brownian-motion analogue. In Brownian motion, a particle receives zero-mean random kicks from surrounding molecules. The cumulative displacement is a biased random walk whose drift yields the friction coefficient through the Green-Kubo relation. Here, a swell packet plays the role of the Brownian particle and each turbulent eddy along the propagation path delivers a zero-mean random energy kick via the stochastic vortex force.